

# **Dynamic Model and Control of Vehicles**

By: Hsueh-Yuan Lu

Supervised by: Dr. Meilan Liu

A Thesis submitted to the Faculty of Graduate Studies  
in partial fulfillment of the requirements for the  
Master of Science in Engineering  
Control Engineering

Lakehead University

September, 2006



Library and  
Archives Canada

Bibliothèque et  
Archives Canada

Published Heritage  
Branch

Direction du  
Patrimoine de l'édition

395 Wellington Street  
Ottawa ON K1A 0N4  
Canada

395, rue Wellington  
Ottawa ON K1A 0N4  
Canada

*Your file* *Votre référence*  
*ISBN: 978-0-494-21534-0*  
*Our file* *Notre référence*  
*ISBN: 978-0-494-21534-0*

**NOTICE:**

The author has granted a non-exclusive license allowing Library and Archives Canada to reproduce, publish, archive, preserve, conserve, communicate to the public by telecommunication or on the Internet, loan, distribute and sell theses worldwide, for commercial or non-commercial purposes, in microform, paper, electronic and/or any other formats.

The author retains copyright ownership and moral rights in this thesis. Neither the thesis nor substantial extracts from it may be printed or otherwise reproduced without the author's permission.

**AVIS:**

L'auteur a accordé une licence non exclusive permettant à la Bibliothèque et Archives Canada de reproduire, publier, archiver, sauvegarder, conserver, transmettre au public par télécommunication ou par l'Internet, prêter, distribuer et vendre des thèses partout dans le monde, à des fins commerciales ou autres, sur support microforme, papier, électronique et/ou autres formats.

L'auteur conserve la propriété du droit d'auteur et des droits moraux qui protègent cette thèse. Ni la thèse ni des extraits substantiels de celle-ci ne doivent être imprimés ou autrement reproduits sans son autorisation.

---

In compliance with the Canadian Privacy Act some supporting forms may have been removed from this thesis.

Conformément à la loi canadienne sur la protection de la vie privée, quelques formulaires secondaires ont été enlevés de cette thèse.

While these forms may be included in the document page count, their removal does not represent any loss of content from the thesis.

Bien que ces formulaires aient inclus dans la pagination, il n'y aura aucun contenu manquant.

  
**Canada**

## ABSTRACT

In this thesis the author develops a 14 degrees-of-freedom (DOF) full-car model. The model draws from and improves upon features and setups of certain existing vehicle dynamics models. The proposed model provides a means to simulate vehicle ride and handling behaviors. An accurate prediction of such behaviors will lead to the proper control and design of vehicles.

The vehicle's kinematics and dynamics are developed to reflect the interactions between the rigid mass elements of the model such as the vehicle body and the wheels. The mathematical model includes the nonlinear characteristics of the tires, the three dimensional motions of the sprung and unsprung masses, the inertial coupling between the sprung and unsprung masses, and the restraints and forces imposed by the suspension components. The frictional forces developed at the road-tire contacts are modeled by the single point contact version of the Lund-Grenoble (LuGre) dynamic friction model. An extension of the LuGre friction model is presented to take into account the coupling between the rotational and translational motions of the wheels.

Three different numerical study cases are selected to verify the model's capability in representing various vehicle dynamic situations with respect to the model's accuracy and to the model's range of applicability.

The issue of active suspension is subsequently discussed. A non-switching sliding mode controller is incorporated into the proposed vehicle model and a substantial reduction in the spectral intensity of a vibration mode of the vehicle body is achieved.

Simulation results suggest that the rigorous modeling and mathematical development yields a model that captures satisfactory ride comfort and vehicle performance.

## ACKNOWLEDGEMENTS

I would like to thank the following people for their help and support during the past two years of study at Lakehead University.

First and foremost, my deepest gratitude goes to my advisor, Dr. Meilan Liu, for guiding my work with valuable insights and detailed comments, for working closely with me and for providing support and encouragement during the course of this research program.

I am very grateful to my co-advisor, Dr. Xiaoping Liu, for his valuable suggestions and help on my research topic.

I am also very grateful to Dr. Abdelhamid Tayebi for the valuable lectures that introduced me to the modern control concepts.

Special thanks go to the examiners, Dr. Alexander Sedov (internal) and Dr. Yuping He (external), for devoting their effort and time to review and make suggestions to my work and helping me to finalize the details.

My sincere thanks go to all my fellow graduate students, for creating a pleasant working environment. Their friendship and support has made my Lakehead experience very enjoyable. Thanks also go to the staff members of the Master's Program in Control Engineering who have helped me in many ways.

Financial support, received by my advisor from the Natural Sciences and Engineering Research Council of Canada (NSERC) that supported this work is gratefully acknowledged.

Finally, I would like to thank my family members and my fiancée, Weilin Wang, for loving me and supporting my work all these years.

# TABLE OF CONTENTS

CERTIFICATE OF EXAMINATION		
ABSTRACT	iii	
ACKNOWLEDGEMENTS	v	
TABLE OF CONTENTS	vii	
LIST OF TABLES	ix	
LIST OF FIGURES	x	
LIST OF APPENDIX	xv	
CHAPTER 1	INTRODUCTION	
1.1	Vehicle Dynamics – A Historical Perspective	1
1.2	Objectives	3
1.3	Organization of the thesis	3
1.4	Relevant Terminologies	5
CHAPTER 2	OVERVIEW OF VEHICLE DYNAMICS MODELS	
2.1	Existing Vehicle Dynamics Models	7
2.2	The Proposed Vehicle Dynamics Model	14
CHAPTER 3	THE 14-DOF FULL-CAR DYNAMIC MODEL	
3.1	Coordinate Systems	15
3.2	The 14-DOF Full-Car Model	19
3.3	Kinematics of Vehicle Body and Wheels	22
3.4	Dynamics of Vehicle Body and Wheels	26
3.5	Simplification of the 14-DOF Full-Car Model	41
3.6	Concluding Remarks	47
CHAPTER 4	ROAD-TIRE FRICTION	
4.1	Literature Review	49
4.2	The LuGre Dynamic Friction Model	52
4.3	Steady-State Characteristics	56

4.4	Validation of Steady-State Behavior with the Magic Formula	61
4.5	Incorporating the LuGre Friction Model	63
4.6	Concluding Remarks	68
CHAPTER 5	NUMERICAL STUDIES OF VEHICLE DYNAMICS	
5.1	A Planar Model of a Three-Wheeled Vehicle	71
5.2	A 7-DOF Full-Car Model	79
5.3	A Full-Car Model for Maneuver Simulation	86
5.4	Conclusions	114
CHAPTER 6	SLIDING MODE CONTROL	
6.1	Background	118
6.2	Vehicle Model (A Pitch-Bounce Half-Car)	121
6.3	Sliding Mode Controller Design	123
6.4	Simulations and Discussions	126
6.5	Conclusions	139
CHAPTER 7	CONCLUSIONS AND RECOMMENDATIONS	
7.1	Conclusions	140
7.2	Recommendations	144
APPENDIX A	DERIVATION OF VELOCITIES AND ACCELERATIONS	147
REFERENCES		149

## LIST OF TABLES

Table 4.1	Magic Formula Parameters	63
Table 4.2	LuGre Model Parameters	63
Table 5.1	Parameters for LuGre Friction Model	73
Table 5.2	Parameters for the TWV	74
Table 5.3	Parameters $\varepsilon$ and $R$	80
Table 5.4	Model Parameters	83
Table 5.5	Model Parameters	91
Table 6.1	System Parameters	122

## LIST OF FIGURES

Figure 1.1	Vehicle Motions	5
Figure 2.1	Quarter-Car Models [2.3]	8
Figure 2.2	A 2-DOF Quarter-Car Model [2.4]	9
Figure 2.3	Half-car model involving pitch and roll motion	10
Figure 2.4	Planar Model of a Three-Wheeled Vehicle [2.6]	11
Figure 2.5	Full-Car Model of A Three-Wheeled Vehicle [2.7]	12
Figure 3.1	Vehicle body frame of reference	16
Figure 3.2	Wheel center and wheel base coordinate frames of reference	18
Figure 3.3	The four frames of reference used	19
Figure 3.4	The full-car model	19
Figure 3.5	Axle roll center bounce and axle rotation as DOFs	21
Figure 3.6	Schematic of the 14-DOF full-car dynamics model (spins not shown)	21
Figure 3.7a	Side view of the vehicle body showing $-x_n \sin \gamma$	24
Figure 3.7b	Front view of the vehicle body showing $y_n \sin \phi$	24
Figure 3.7c	Locations of wheel centers in the vehicle body frame of reference	25
Figure 3.8	FBD of vehicle body (showing forces and torques from wheels 2 and 3 only)	28
Figure 3.9a	FBD of the vehicle body as viewed along the $x$ -axis	31
Figure 3.9b	FBD of the vehicle body as viewed along the $y$ -axis	31
Figure 3.9c	FBD of the vehicle body as viewed along the top	32
Figure 3.10	Vehicle body as viewed along the $y$ -axis showing $H$ , $z$ and $z_n$	32
Figure 3.11	Forces exerted by road surface onto the wheel bases	33

Figure 3.12	FBD of a wheel	34
Figure 3.13	Free body diagram of a wheel (showing only forces in the z-direction)	36
Figure 3.14a	[A] Matrix as inputted into MAPLE	40
Figure 3.14b	[A] <sup>-1</sup> Matrix as determined by MAPLE	40
Figure 3.15	A quarter-car model [3.13]	43
Figure 3.16	A half-car model showing pitch and bounce motions [3.14]	44
Figure 3.17	A half-car model showing roll and bounce motions [3.15]	45
Figure 3.18	A 7-DOF full-car Model [3.12]	47
Figure 4.1	The average internal deflected state $\eta$ in the direction of motion	53
Figure 4.2	The effect on $g(V_r)$ due to changes in friction parameters	54
Figure 4.3a	Slip for braking	59
Figure 4.3b	Slip for acceleration	59
Figure 4.4	Steady-state friction forces $F_x(s)$ and $F_y(\beta)$	63
Figure 4.5a	Bristle deformation before rotation	64
Figure 4.5b	Bristle deformation after rotation	64
Figure 4.6	Total bristle deflection with respect to the global frame	66
Figure 4.7	Vehicle steering geometry definition [4.10]	69
Figure 5.1	The planar TWV model	71
Figure 5.2	Half-sine wave road profile	74
Figure 5.3	Normal reaction at front/rear wheel	75
Figure 5.4a	Vertical acceleration of the vehicle body – Time history	76
Figure 5.4b	Vertical acceleration of the vehicle body – Frequency spectrum	76

Figure 5.5	Comparisons of the present model and Ref. [5.1]	78
Figure 5.6	Frictional forces	78
Figure 5.7	Dry friction behavior	80
Figure 5.8	Ramp-like bump profile	82
Figure 5.9	Time-delay at 10 m/s	82
Figure 5.10a	Vertical displacement of vehicle body	84
Figure 5.10b	Pitch angle of vehicle body	84
Figure 5.10c	Vertical acceleration of vehicle body	85
Figure 5.11	Damper friction forces	85
Figure 5.12	Steering geometry definition (showing right steering) [5.3]	87
Figure 5.13	Driver steering input	89
Figure 5.14	Longitudinal/Lateral friction forces	92
Figure 5.15	Vehicle body speeds for pavement road with no torque input	93
Figure 5.16	Wheels' rotational speeds with no torque input	95
Figure 5.17	Longitudinal/Lateral relative velocity of each wheel with no torque input	96
Figure 5.18	Longitudinal/Lateral bristle deflection at each wheel	97
Figure 5.19	Longitudinal/Lateral dynamic friction coefficients	98
Figure 5.20	Normal forces during turn maneuver	99
Figure 5.21	Vehicle position with no torque input	100
Figure 5.22a	Comparison of vehicle body speeds	102
Figure 5.22b	Comparison of vehicle position	103
Figure 5.23	Comparison of longitudinal/lateral frictional forces	103-104
Figure 5.24	Comparison of longitudinal/lateral relative velocities	104-105

Figure 5.25a	Vehicle body speeds, no torque input	106
Figure 5.25b	Vehicle position, no torque input	107
Figure 5.26a	Vehicle body speeds, 50 N.m input torque	107
Figure 5.26b	Vehicle position, 50 N.m input torque	108
Figure 5.27a	Normal forces for turn maneuver with no torque input	108
Figure 5.27b	Normal forces for turn maneuver with 50 N.m torque input	109
Figure 5.28	Longitudinal/Lateral friction forces, no torque input	109-110
Figure 5.29	Longitudinal/Lateral friction forces, 50 N.m torque input	110-111
Figure 5.30	Comparison of vehicle positions, no torque input	112
Figure 5.31	Comparison of vehicle positions, slippery road	113
Figure 5.32	Vehicle spins out of control, 100 N.m torque to rear wheels	113
Figure 5.33	Lateral frictional forces, 100 N.m torque to rear wheels	114
Figure 6.1a	Schematic of a passive suspension system	120
Figure 6.1b	Schematic of an active suspension system	120
Figure 6.2	A single ramp-step bump	126
Figure 6.3a	Vehicle body bounce	128
Figure 6.3b	Vehicle body pitch	129
Figure 6.3c	Acceleration of vehicle body bounce	129
Figure 6.3d	Acceleration of vehicle body pitch	130
Figure 6.4	Control input forces at front/rear suspension	130-131
Figure 6.5	Frequency spectrum of body bounce/pitch accelerations	131-132
Figure 6.6a	Vehicle bounce acceleration – Change in sprung mass	133
Figure 6.6b	Vehicle bounce acceleration – Change in spring coefficients	134
Figure 6.6c	Vehicle bounce acceleration – Change in damping coefficients	134

Figure 6.7	Control input forces at front/rear suspension	136
Figure 6.8a	Vehicle body bounce	137
Figure 6.8b	Vehicle body pitch	137
Figure 6.9	Frequency spectrum of body bounce/pitch accelerations	138

## LIST OF APPENDIX

APPENDIX A	DERIVATION OF VELOCITIES AND ACCELERATIONS	147
------------	-----------------------------------------------	-----

## CHAPTER 1

### INTRODUCTION

#### 1.1 Vehicle Dynamics – A Historical Perspective.

The study of vehicle dynamics started probably in the early 1930s [1.1]. The tools used in those days were mainly experimental observations. Ride comfort was first considered an important issue of vehicle performance during this period. This period also saw theoretical development that led to the practical design of suspension systems.

From the 1930s to 1950s, the importance of achieving a satisfactory compromise between ride comfort and vehicle handling performance was recognized. The importance of the main force-generating element, the tire, had also been recognized by experimental measurement of the force and moment properties. Accordingly, the design of the suspension system was advanced. It is interesting to note that the development of independent suspension was introduced during this period [1.1].

For the next three to four decades, the maturing theories and technologies expanded significantly. More accurate rig results and mathematical models were developed for which the tire and vehicle dynamics behaviors could be studied and verified

experimentally. Dynamic analysis was also broadened to consider studies of vehicle stability, handling and vibration to predict ride comfort [1.1].

The last decade or two witnessed research in vehicle dynamics moving toward and relying on more and more the development of computer modeling and simulation methods [1.2]. Currently, these computer codes provide a range of ride and handling models of varying degrees of complexity, which could hardly be prepared manually. All of the commonly required calculations for vehicle dynamics studies have been embodied in multi-body system (MBS) dynamics codes. These codes are expressed and solved either numerically or analytically. The latter approach has the advantage of fast simulation run time and ease of parameter change and control system implementation. Depending on user preference, there are many computer packages commercially available. Examples of stand-alone packages include ADAMS/CAR [1.3] and CarSim [1.4]. There are also “add-ons” available that serve the same purpose such as the many Matlab “tool boxes” contained in [1.5].

Although one could logically suggest the use of these codes for a vehicle dynamic study, the complexity of these codes makes it difficult to add user routines or add-ons, not to mention that one may not be able to test the different underlying assumptions inherent in the development of such codes. In addition, due to the complexity and the size of the

output data that the codes tend to generate, it is difficult to introduce and investigate various control schemes. Therefore, in this thesis the author will propose and develop a vehicle model that is of medium complexity, but nevertheless one that is able to capture the physical essence of ride comfort and vehicle handling performance.

## **1.2 Objectives.**

The author will propose a vehicle dynamics model consisting of a rigid vehicle body and rigid wheels, having independent suspensions connecting the vehicle body and wheels, and taking into consideration tire-road interaction. The model will be able to address ride and handling simulations, and ride comfort control applications. The scope of the model presented will include derivation of the vehicle dynamics model, modification of the Lund Grenoble (LuGre) dynamic friction model [1.6], numerical case studies for the modeling verifications by using Matlab [1.7], and control application using the non-switching sliding mode control technique for the improvement of ride comfort.

## **1.3 Organization of the Thesis.**

The thesis contains seven chapters.

Chapter 1 deals with the introduction.

Chapter 2 presents an overview of some existing vehicle dynamics models and their applications.

In Chapter 3, the development of a 14-degrees-of-freedom (DOF) full-car dynamic model is described. The model considers the vehicle body, suspensions as well as the wheel motions in a pre-selected coordinate system. Derivations of equations of motion are governed by the principles of Newtonian mechanics. The coupling of some equations is addressed. Simplification of the proposed model and comparisons to existing models are then presented.

Chapter 4 is concerned with a crucial component of the vehicle model, the dynamic friction, or the road-tire contact force. It focuses on the LuGre model. Extension of the existing one-dimensional friction model to a two-dimensional model is made and validated. The 2-D LuGre model is subsequently introduced into the full-car model of Chapter 3.

Chapter 5 is where the developments of Chapters 3 and 4 come together and are applied. Three numerical case studies are included to demonstrate the applicability and accuracy of the proposed model.

Chapter 6 introduces the non-switching sliding mode control technique to the

proposed vehicle model. A pitch-bounce car model is used to demonstrate the effectiveness of the sliding mode control technique.

#### 1.4 Relevant Terminologies.

A few terminologies are introduced here to facilitate the understanding of Chapter 2 in particular. With reference to Figure 1.1, translation along the  $x$ -axis is the longitudinal or forward motion; lateral or sideward motion is the translation along the  $y$ -axis and bounce refers to the vertical ( $z$ -axis) translation of the main body of the vehicle. The rotations about the  $x$ -,  $y$ - and  $z$ -axes are known as the roll, pitch, and yaw, respectively. A wheel's rotation about its spin ( $y$ ) axis is its spin ( $\omega$ ) and its vertical motion ( $z$ ) is its bounce.

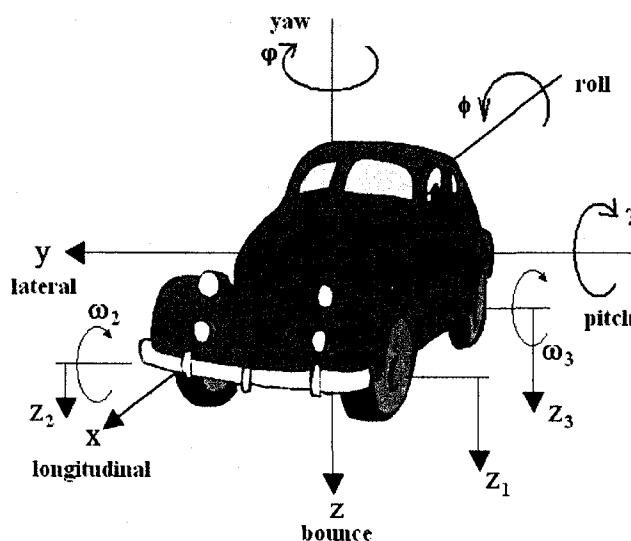


Figure 1.1 Vehicle Motions

## CHAPTER 2

### OVERVIEW OF VEHICLE DYNAMICS MODELS

In studying vehicle dynamics, three essential components are considered for typical ground vehicles, the main body of the vehicle (sprung mass), the suspension system, and the wheels (unsprung masses). The vehicle's kinematics and dynamics can be described from the interactions among those rigid bodies. The incorporation of road-tire interaction is also an essential part of vehicle dynamics. Therefore, "it is important to construct a mathematical model that includes the nonlinear characteristics of the tires, the general three dimensional motions of the sprung and unsprung masses, the required inertial coupling between sprung and unsprung masses, and an accurate representation of the restraints and forces imposed by the suspension components" [2.1].

Vehicle dynamics covers a wide range of subject material because it is a study of anything relating to vehicle systems. However, two major areas have been studied extensively; ride comfort and vehicle handling performance [2.2]. Even today many researchers are seeking ways to further improve ride comfort and vehicle handling by developing analytical tools, and by advancing control techniques to attain the desired goal.

Simply to avoid the complexity of coupled vehicle modes, many researchers have studied ride comfort and vehicle handling separately. Logically one could ask, “How can this be justified when it is clear in the real world the vehicles are subjected to ride and handling inputs simultaneously?” [2.2]. The two aspects are inextricably linked to one another. However, it may be difficult, if not impossible, to analyze or simulate all the vehicle dynamics simultaneously.

## **2.1 Existing Vehicle Dynamics Models.**

Many vehicle models have been developed. They were derived by considering energy equilibrium or dynamic equilibrium. In general, these models can be classified into three types: (i) the quarter-car model, (ii) the half-car model, and (iii) the full-car model.

### 2.1.1 Quarter-Car Models

A quarter-car model consists of one wheel and associated suspension, and a body mass.

Due to its simplicity in modeling and the relative ease in obtaining analytical results, the model is primarily used to study vehicle ride comfort and to implement advanced control.

In this 2-DOF model, the vertical motions of body mass (sprung mass) and the associated wheel and suspension masses (unsprung masses) are considered.

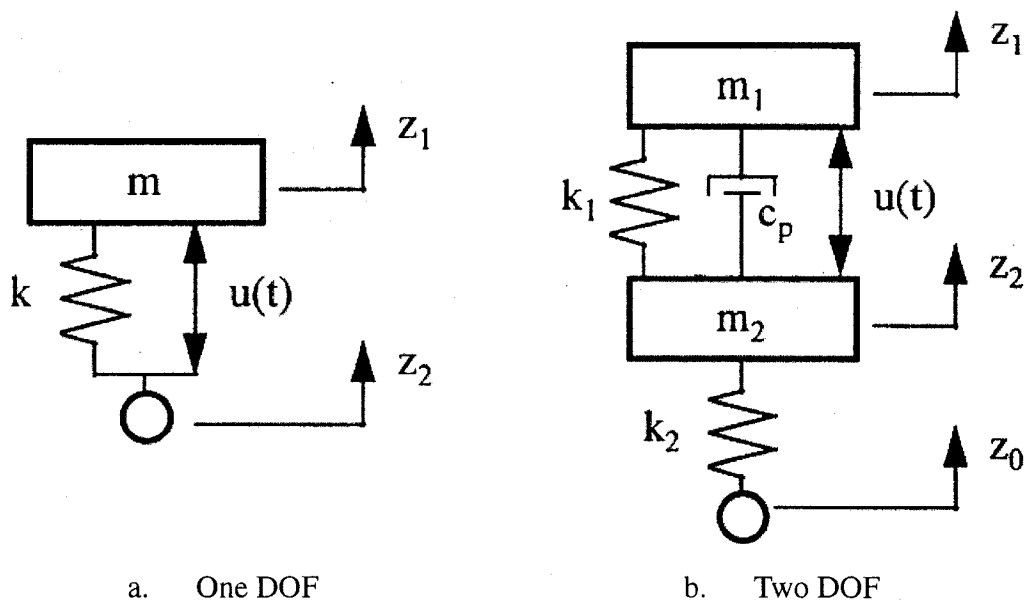


**Figure 2.1 Quarter-Car Models [2.3]**

Hac and Fratini presented their work on vehicle ride comfort using the “skyhook” damping control law [2.3]. The mathematical vehicle models used were quarter-car models with one DOF (Figure 2.1a) and two DOFs (Figure 2.1b), respectively. It should be mentioned that in this chapter, figures retain their original notations; that is, notations used in the references. In Chapter 3 however, figures will be annotated by symbols consistent with those used in this thesis. The model in Figure 2.1a used a single DOF to describe the vertical response,  $z_1(t)$ , of the sprung mass after road signal  $z_2(t)$  is inputted. The 2-DOF model shown in Figure 2.1b considered motions of both the sprung and unsprung masses. In addition to the spring ( $k_1$ ), a linear passive damper ( $C_p$ ) was also introduced. It should be pointed out that  $u(t)$  in both models represents the “continuously

variable real time damping” forces that were governed by the “skyhook” damping control law.

A similar model was used by Simon [2.4]. The focus of his work was also on the primary suspension systems. Various suspension systems, conventional and non-conventional, were evaluated and compared for obtaining the optimal trade-off relationships between ride and handling. A prototype of a continuously variable semi-active system implementing the “skyhook” control algorithm was constructed, and tested for its dynamic effect on vehicles. The work was also based on a quarter-car model of 2 DOFs (Figure 2.2).

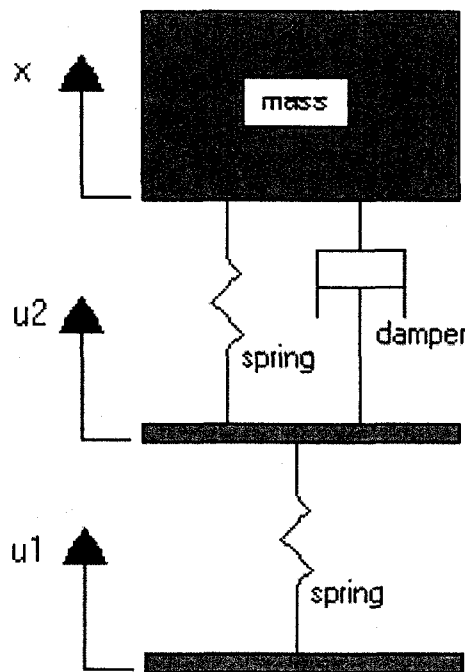


**Figure 2.2** A 2-DOF Quarter-Car Model [2.4]

### 2.1.2 Half-Car Models

A half-car model typically consists of either the left or right half of a vehicle, or the front or rear half of the vehicle. The former is usually called the pitch-bounce model (Figure 2.3a), while the latter is the roll-bounce model (Figure 2.3b). There is also the so-called roll-yaw model that includes, as its DOFs, the lateral, roll and yaw motions of the vehicle.

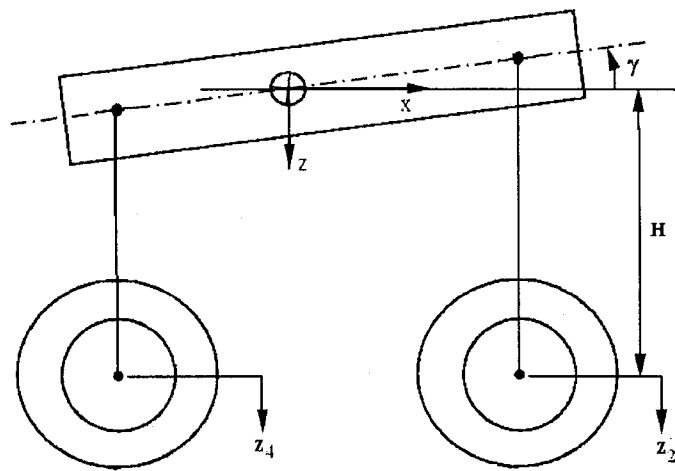


Figure 2.3a Half-car model involving pitch motion

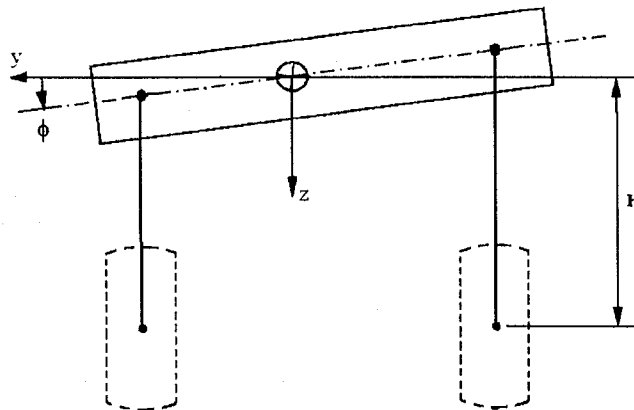


Figure 2.3b Half-car model involving roll motion

Chen *et al.* [2.5] presented a pitch-bounce model along with their work on constrained  $H_\infty$  control to active suspension systems on a vehicle. The half-car model had 4 DOFs, the bounce and pitch of the vehicle body and the bounces of the two wheels. The suspension and tire were modeled by linear springs and viscous dampers. Gawade *et al.* showed the in-plane 7-DOF mathematical model of a three-wheel vehicle to study the influence of bump profiles on occupant injury [2.6]. The planar three-wheeled vehicle model considered the motions of longitudinal, bounce and pitch of vehicle body, and the motions of bounce and rotation of the wheels (Figure 2.4).

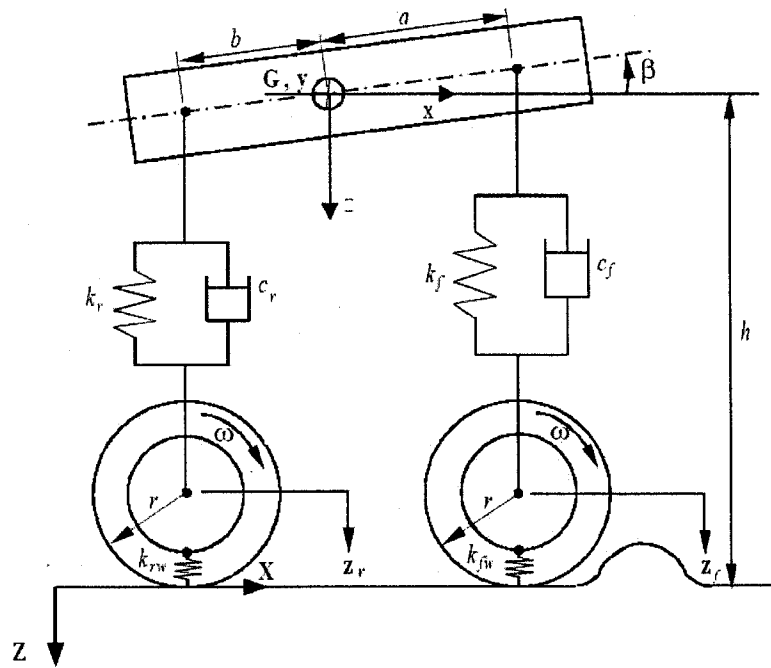
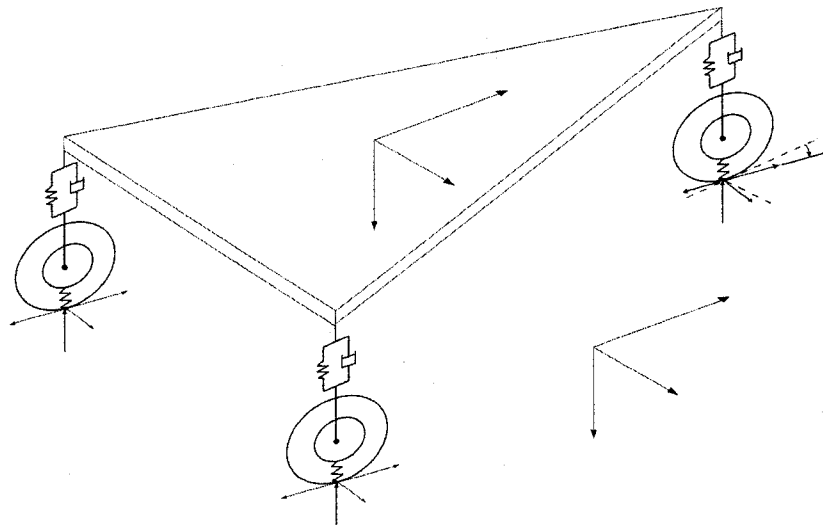


Figure 2.4 Planar Model of a Three-Wheeled Vehicle [2.6]

### 2.1.3 Full-Car Models

Further to their in-plane model [2.6], Gawade *et al.* developed a three dimensional model of the three-wheeled vehicle with suspensions and compliant tires [2.7]. It had 6 DOFs for the vehicle body, and another 6 DOFs describing the vertical displacements and rotation motions of the wheels (Figure 2.5).



**Figure 2.5 Full-Car Model of A Three-Wheeled Vehicle [2.7]**

For this seemingly simple full-car model, a good amount of detail had to be incorporated. For example, transformation matrices were used to describe the relation between the inertial coordinate frame and body centered coordinates. These matrices were written in terms of three independent Euler angles (the yaw, roll, and pitch angles). The equations of motion also took into account the steering effect. The so-called “Magic

Formula” [2.8] was used to describe the tire’s behavior in the lateral direction for different slip angles, and the Coulomb friction model was used to describe rolling resistance, or the tire’s behavior in the longitudinal direction.

A simplified full-car model, together with the 2-D LuGre friction model, was presented by Vilella in [2.9] to study the handling responses with implementation of the input-output linearization control technique. The main focus of the work was on incorporating the LuGre dynamic friction model into the full-car model and on simulating the handling responses under a less aggressive lane change maneuver by the driver over a smooth road.

Vilella’s model was developed with reduced complexity in mind. The suspensions were absent. They were replaced by four rigid joints, which resulted in a 7-DOF model. The DOFs were, the longitudinal, lateral, and yaw motions of the vehicle body, and the rotation motion of each wheel. As for the absence of suspensions, the equations of normal reaction forces among the four wheels were determined analytically by using static force balance in the  $z$  direction, static moment balances about the pitch and roll axes, and a hypothetical suspension model with infinitely large values of the spring stiffness. Accordingly, the normal reaction forces depend only on the geometric parameters of the vehicle, the steering angles, and the tire-road friction functions.

## **2.2 The Proposed Vehicle Dynamics Model.**

This thesis proposes a 14-DOF full-car model. This model can be viewed as an improved version on those presented in [2.7, 2.9]. Specifically, the vehicle body will have 6 DOFs representing the six rigid body motions. Each wheel will have a bounce and a spin motion associated with it. Suspensions will be present, so will road-tire interaction. The detailed description and derivation of the model will be presented in the next two chapters, where the reader may note that, for the kinematics, this thesis draws upon and expands the work presented in [2.9]. For the dynamics, however, the free-body diagrams of Reference [2.6] will be utilized where appropriate. This more general full-car model will then be simplified to quarter- and half-car models, and to full-car models with fewer DOFs.

## CHAPTER 3

### THE 14-DOF FULL-CAR DYNAMIC MODEL

The first step in vehicle modeling is a thorough understanding of the physics – kinematics and dynamics – of motion of the vehicle. This chapter is devoted to such a task, to develop a 14-DOF full-car mathematical model. This model, like any other car models, will provide a means to simulate vehicle dynamic behaviors which can further lead to the proper design and control of vehicles.

The study of motion will inevitably involve the setup and use of frames of references. Once the kinematics, the absolute accelerations in particular, is understood, the Newton's laws are applied in order to establish the required equations of motion. These equations of motion are then simplified so as to compare with other car models. This not only validates the proposed full car model, it also demonstrates the versatility of the model.

#### 3.1 Coordinate Systems.

Four frames of reference are used throughout the study. They are introduced below.

- 1) Global coordinates  $X$ - $Y$ - $Z$

The global coordinates are used to measure the absolute position of the vehicle. It is an earth-fixed frame of reference, and considered as an inertial frame [3.1]. Its origin is arbitrary, but chosen as the position that the center of gravity of the vehicle body takes when  $t = t_0$ . Note that the origin is fixed once chosen.

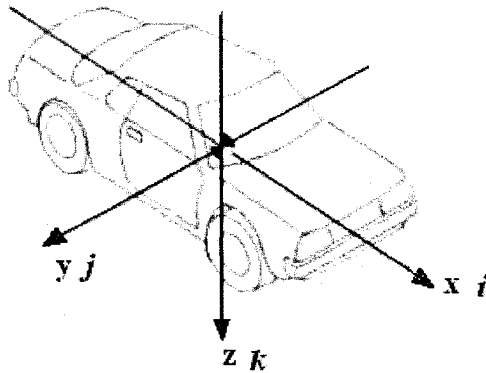


**Figure 3.1 Vehicle body frame of reference**

2) Vehicle body coordinate frame  $x-y-z$

This coordinate frame is associated with unit vectors  $\vec{i}, \vec{j}, \vec{k}$  (Figure 3.1). It is a frame that is simultaneously coincident with the vehicle body's center of gravity

$CG$ , but it is not vehicle-fixed in that the

$x$ - and  $y$ -axes do not rotate as the vehicle rolls and pitches; That is they don't rotate about the longitudinal and the lateral axes. Instead they are parallel to the ground all the time, and are instantaneously aligned with the vehicle's longitudinal and lateral axes, respectively, while the  $z$ -axis is determined by the right hand rule. The advantages of such a setup include, (1) that only one rotation matrix is required for coordinate transformation; and (2) that  $x-y-z$  can be regarded as the vehicle's principal axes of mass moments of inertia, under the assumption of small roll and small pitch. The rotation matrix required for the transformation from  $x-y-z$  to  $X-Y-Z$  is,

$$\begin{Bmatrix} X \\ Y \\ Z \end{Bmatrix} = \begin{bmatrix} \cos \varphi & -\sin \varphi & 0 \\ \sin \varphi & \cos \varphi & 0 \\ 0 & 0 & 1 \end{bmatrix} \begin{Bmatrix} x \\ y \\ z \end{Bmatrix} \quad (3.1)$$

where  $\varphi$  is the yaw angle and is determined by  $\varphi = \int_{t_0}^t \dot{\varphi} dt$  with  $\dot{\varphi}$  being the yaw rate.

### 3) Wheel centered coordinate frame $x_{cw,n}$ - $y_{cw,n}$ - $z_{cw,n}$

This coordinate frame has unit vectors  $\vec{i}_{cw,n}$ ,  $\vec{j}_{cw,n}$ ,  $\vec{k}_{cw,n}$  attached to the wheel center  $CW_n$ ,

with the  $x_{cw,n}$ -,  $y_{cw,n}$ - and  $z_{cw,n}$ -axes being parallel to the vehicle's  $x$ -,  $y$ - and  $z$ -axes,

respectively (Figure 3.2). Hence this frame differs from the vehicle body frame only in

their coordinate origins. Unless stated otherwise, the subscript  $n$  denotes the wheel and

takes on values of 1 through 4.

### 4) Wheel base coordinate frame $x_{bw,n}$ - $y_{bw,n}$ - $z_{bw,n}$

The wheel base coordinate frame is attached to a wheel's base, with the  $y_{bw,n}$ -axis being

parallel to the wheel's rotation axis (the spin axis), the  $x_{bw,n}$ -axis parallel to the ground,

and the  $z_{bw,n}$ -axis parallel to the  $z$ -axis of the vehicle body (Figure 3.2). The frame rotates

with the wheel as it steers, or it is wheel-fixed. That is, the wheel base coordinate frame

differs from the wheel center coordinate frame by the steering angle  $\theta_n$  of the wheel. The

wheel center unit vectors  $\vec{i}_{cw,n}$ ,  $\vec{j}_{cw,n}$ ,  $\vec{k}_{cw,n}$  and the wheel base unit vectors  $\vec{i}_{bw,n}$ ,  $\vec{j}_{bw,n}$ ,  $\vec{k}_{bw,n}$  are

related by,

$$\begin{aligned}
\vec{i}_{cw,n} &= \cos \theta_n \vec{i}_{bw,n} - \sin \theta_n \vec{j}_{bw,n} & \vec{i}_{bw,n} &= \cos \theta_n \vec{i}_{cw,n} + \sin \theta_n \vec{j}_{cw,n} \\
\vec{j}_{cw,n} &= \sin \theta_n \vec{i}_{bw,n} + \cos \theta_n \vec{j}_{bw,n} & \vec{j}_{bw,n} &= -\sin \theta_n \vec{i}_{cw,n} + \cos \theta_n \vec{j}_{cw,n} \\
\vec{k}_{cw,n} &= \vec{k}_{bw,n} & \vec{k}_{bw,n} &= \vec{k}_{cw,n}
\end{aligned} \tag{3.2}$$

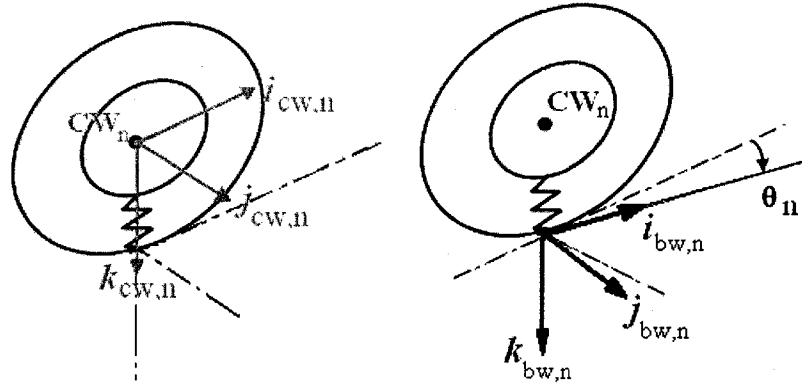


**Figure 3.2 Wheel center and wheel base coordinate frames of reference**

Figure 3.3 compares the four coordinate frames mentioned above. It illustrates how they relate to each other. It is noted that the earth-fixed  $X$ - $Y$ - $Z$ , vehicle body  $x$ - $y$ - $z$  and wheel base  $x_{bw,n}$ - $y_{bw,n}$ - $z_{bw,n}$  frames of reference follow the SAE recommended practice [3.2]. As will be seen later, the equations that govern the general, nonlinear motion of the vehicle are written in terms of the vehicle body frame of reference  $x$ - $y$ - $z$ . This choice of frame of reference greatly simplifies the derivation and calculation of the vehicle model. It should finally be pointed out that wheel chamber (rotation of a wheel about the  $x_{cw,n}$ -axis) is not considered in this study.

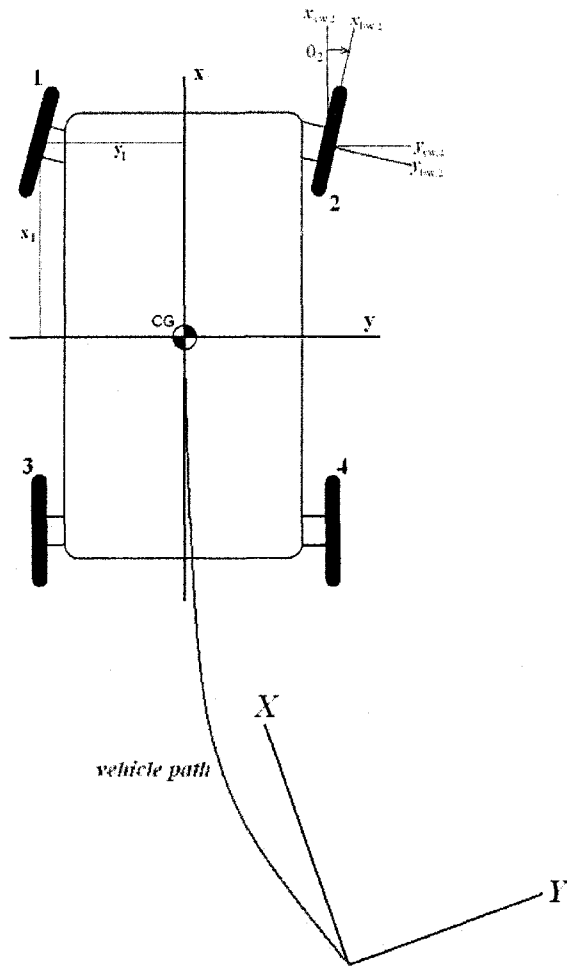


Figure 3.3 The four frames of reference used

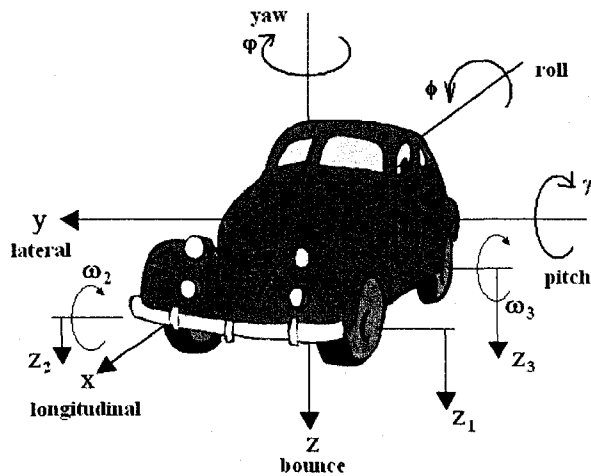


Figure 3.4 The full-car model

### 3.2 The 14-DOF Full-Car

#### Model.

The full-car model has in total 14

DOFs. They are  $x, y, z, \phi, \gamma, \varphi,$

$z_1, z_2, z_3, z_4, \omega_1, \omega_2, \omega_3, \omega_4$

(Figure 3.4,  $z_4$  and  $\omega_1, \omega_4$  not

shown) where  $x, y, z, \phi, \gamma, \varphi$  are the

longitudinal, lateral, bounce, roll,

pitch, and yaw motions of the

vehicle body;  $z_1, z_2, z_3, z_4$  the

bounce motions of the left front,

right front, left rear and right rear

wheels, and  $\omega_1, \omega_2, \omega_3, \omega_4$  the

angular motion (spin) of the left

front, right front, left rear and right

rear wheels, respectively. Features

of this 14-DOF full-car model are,

a) The vehicle body is treated as

a rigid body (the sprung mass as per terminology of [3.2]) with the six DOFs,

$$x, y, z, \phi, \gamma, \varphi;$$

b) Each wheel is modeled as a rigid body (the unsprung mass [3.2]) with bounce motion  $z_n$  and spin  $\omega_n$ ;

c) The wheel bounce  $z_n$  is considered independent of  $z$ , the bounce of the vehicle body.

Moreover, the bounces of the wheels are considered independent of each other, so are the spins;

Such a setup obviously has independent suspensions in mind, but can easily accommodate solid axle suspensions. In vehicle modeling, it is often the practice to have 2 DOFs for each axle [3.3]. With independent suspensions, these two axle DOFs turn out to be the bounce motions of the wheels at the ends of the axle; while for solid axle suspensions, one may choose to use, as the axle DOFs, the bounce of the axle's roll center and the axle rotation [3.4], with the latter being easily transformed to the former (Figure 3.5).

d) It should then be noted that each wheel center is connected to the vehicle body through a "spring-damper" combination,  $k_{sn}$  and  $c_{sn}$ ; In addition, the Coulomb friction can be included (see [3.6]). However, such friction (stop) force is not considered in the present study.

- e) The tires are considered linear springs with spring constants  $k_m$ ; a 2-Step tire stiffness model [3.6] may also be incorporated and considered in the future work; and
- f) The steering of the wheels is not treated as a DOF. However, as can be seen in Chapter 4, steering is incorporated into the model through tire-road interaction, hence becoming “a state”.

A schematic of the full car model is shown in Figure 3.6 where  $z_{sn}$  denotes road profile, or terrain.

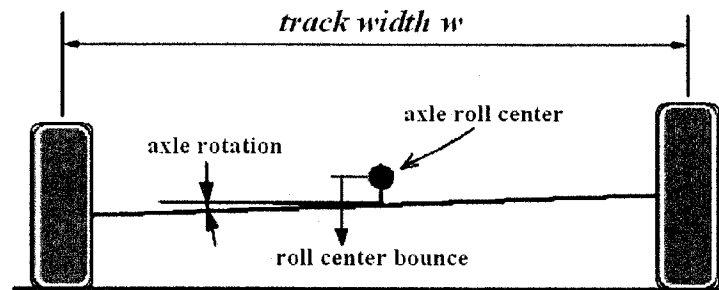


Figure 3.5 Axle roll center bounce and axle rotation as DOFs

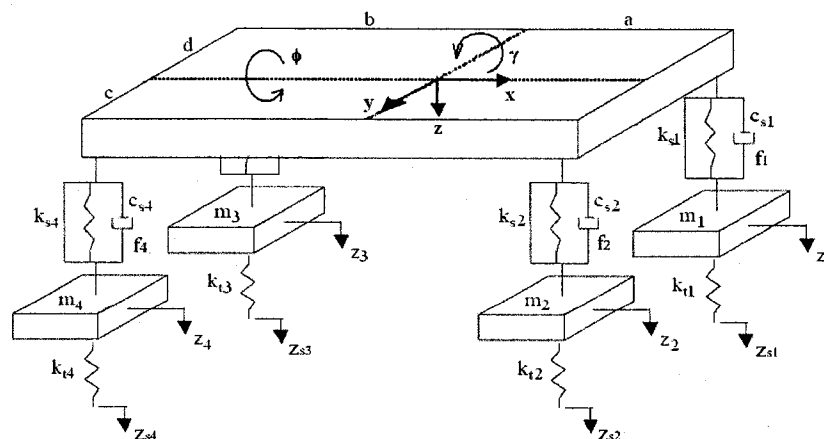


Figure 3.6 Schematic of the 14-DOF full-car dynamics model (spins not shown)

Other 14-DOF full-car models available in the literature have same or similar setup of DOFs. For example, the same DOFs were used in [3.3 – 3.5]. It is interesting to note that, while Reference [3.3] pointed out that the 14-DOF model “is quite suitable for simulating vehicle response under significant ( $\pm 10$  degrees) roll motions”, Reference [3.5] suggested that “the effect of the anti-roll bar is not negligible”, and included a simple way to integrate the roll stiffness with the suspension model. On the other hand, Reference [3.6] presented a 16-DOF full-car model. They were, six DOFs (longitudinal, lateral, bounce, roll, pitch and yaw) for the vehicle body, three DOFs per axle (axle roll, bounce and steer for solid axle suspensions, and left wheel bounce, right wheel bounce and axle steer for independent suspensions), and one DOF (the spin) per wheel. It is noted that the model in [3.6] included that of the steering system; as a result, steering angles were governed by the equations of motion of the steering system. Since steering is not modeled in the present study, steering angles are incorporated as inputs rather than as DOFs.

### **3.3 Kinematics of Vehicle Body and Wheels.**

#### **3.3.1 Velocity and Acceleration at Center of Gravity of the Vehicle Body, $CG$ .**

$V_{cg}$  and  $A_{cg}$  are conveniently expressed in terms of unit vectors  $\vec{i}, \vec{j}, \vec{k}$  of the vehicle body frame  $x$ - $y$ - $z$  (Figure 3.1)

$$\mathbf{V}_{cg} = \dot{x}\vec{i} + \dot{y}\vec{j} + \dot{z}\vec{k}, \quad \mathbf{A}_{cg} = \ddot{x}\vec{i} + \ddot{y}\vec{j} + \ddot{z}\vec{k} + \dot{x}\dot{\vec{i}} + \dot{y}\dot{\vec{j}} + \dot{z}\dot{\vec{k}} \quad (3.3)$$

Since the vehicle body frame rotates with angular velocity components of  $[0, 0, \dot{\varphi}]$ ,

or the angular velocity vector of the  $x$ - $y$ - $z$  frame is  $\boldsymbol{\Omega} = \dot{\varphi}\vec{k}$ , one can write

$$\dot{\vec{i}} = \boldsymbol{\Omega} \times \vec{i} = \dot{\varphi}\vec{j}, \quad \dot{\vec{j}} = \boldsymbol{\Omega} \times \vec{j} = -\dot{\varphi}\vec{i}, \quad \dot{\vec{k}} = \boldsymbol{\Omega} \times \vec{k} = \vec{0} \quad (3.4)$$

so that  $\mathbf{A}_{cg}$  becomes

$$\mathbf{A}_{cg} = (\ddot{x} - \dot{y}\dot{\varphi})\vec{i} + (\ddot{y} + \dot{x}\dot{\varphi})\vec{j} + \ddot{z}\vec{k} \quad (3.5)$$

It is noted that, though  $\mathbf{V}_{cg}$  and  $\mathbf{A}_{cg}$  are expressed in terms of  $x, y, z$  and  $\vec{i}, \vec{j}, \vec{k}$ , they are absolute velocity and absolute acceleration measured with respect to the global frame  $X$ - $Y$ - $Z$  which is inertial.

### 3.3.2 Velocity and Acceleration at a Wheel Center, $CW_n$ .

In determining the velocity and acceleration at a wheel center  $CW_n$ , one starts with the velocity and acceleration of the point that is at the top end of the suspension connecting the wheel center and the vehicle body. Since such a point is a point in the vehicle body, one has,

$$\mathbf{V}_{vb,n} = \mathbf{V}_{cg} + \boldsymbol{\Omega} \times \mathbf{r}_{vb,n} \quad (3.6)$$

where  $\mathbf{V}_{cg}$  is the velocity of vehicle body's  $CG$  written with respect to the  $x$ - $y$ - $z$  frame,

$\boldsymbol{\Omega} = \dot{\varphi}\vec{k}$  is the angular velocity vector of the frame, and  $\mathbf{r}_{vb,n}$  is the relative position

vector of the top end of the suspension with respect to  $CG$ . It can be shown that (Figures 3.7a, b)

$$\begin{aligned} \mathbf{r}_{vb,n} &= x_n \vec{i} + y_n \vec{j} + (-x_n \sin \gamma + y_n \sin \phi) \vec{k} \\ &\doteq x_n \vec{i} + y_n \vec{j} + (-x_n \gamma + y_n \phi) \vec{k} \end{aligned} \quad (3.7)$$

where  $x_n$  and  $y_n$  are the  $x$ - and  $y$ -coordinates of a wheel center  $n$  (see Figure 3.7c). They can be determined by the wheelbase and track width of the vehicle. Note that the small roll and small pitch assumption has been invoked in equation (3.7). Substitution of  $\mathbf{V}_{cg}$ ,  $\boldsymbol{\Omega}$  and  $\mathbf{r}_{vb,n}$  yields,

$$\mathbf{V}_{vb,n} = (\dot{x} - \dot{\phi} y_n) \vec{i} + (\dot{y} + \dot{\phi} x_n) \vec{j} + \dot{z} \vec{k} \quad (3.8)$$

and

$$\mathbf{A}_{vb,n} = (\ddot{x} - \ddot{\phi} y_n - \dot{\phi} \dot{y} - \dot{\phi}^2 x_n) \vec{i} + (\ddot{y} + \ddot{\phi} x_n + \dot{\phi} \dot{x} - \dot{\phi}^2 y_n) \vec{j} + \ddot{z} \vec{k} \quad (3.9)$$

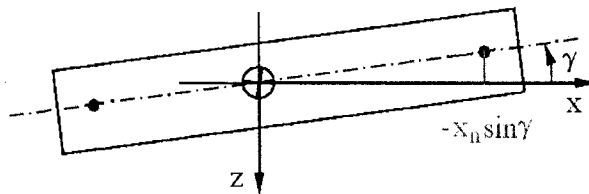


Figure 3.7a Side view of the vehicle body showing  $-x_n \sin \gamma$

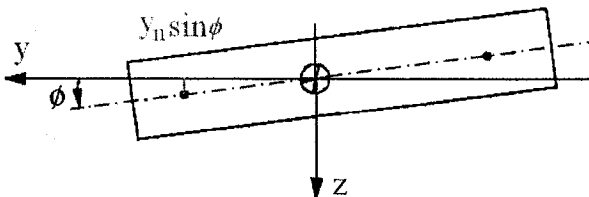


Figure 3.7b Front view of the vehicle body showing  $y_n \sin \phi$

Now, if it is assumed that the wheel centers will assume the  $x$ - and  $y$ -components of  $V_{vb,n}$  and  $A_{vb,n}$ , so that the relative motion between the vehicle body and the wheels will only occur in the vertical direction (or along the  $z$ -direction). The velocity and acceleration of the wheel centers are then,

$$\mathbf{V}_{cw,n} = (\dot{x} - \dot{\varphi}y_n)\vec{i} + (\dot{y} + \dot{\varphi}x_n)\vec{j} + \dot{z}_n\vec{k} \quad (3.10)$$

and

$$\mathbf{A}_{cw,n} = (\ddot{x} - \ddot{\varphi}y_n - \dot{\varphi}\dot{y} - \dot{\varphi}^2x_n)\vec{i} + (\ddot{y} + \ddot{\varphi}x_n + \dot{\varphi}\dot{x} - \dot{\varphi}^2y_n)\vec{j} + \ddot{z}_n\vec{k} \quad (3.11)$$

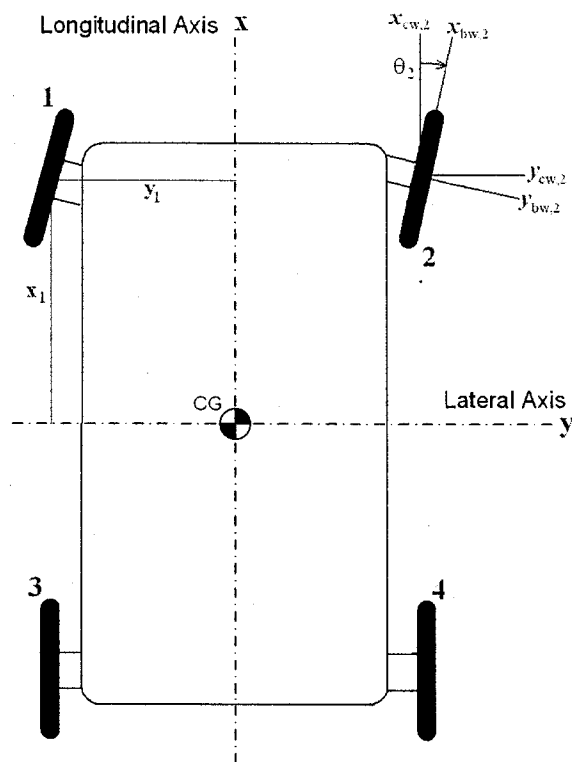


**Figure 3.7c** Locations of wheel centers in the vehicle body frame of reference

It should be mentioned that  $V_{cw,n}$  and  $A_{cw,n}$  are absolute velocity and absolute acceleration measured with respect to the  $X$ - $Y$ - $Z$  frame but expressed in terms of  $x$ ,  $y$ ,  $z$  and  $\vec{i}, \vec{j}, \vec{k}$ . The relative displacement between a wheel center and the vehicle body represents the compression experienced by the suspension located between the wheel and the vehicle body. This relative displacement and its time-derivative are

$$\begin{aligned}\Delta z_n &= z - x_n \sin \gamma + y_n \sin \phi - z_n \doteq z - x_n \gamma + y_n \phi - z_n \\ \Delta \dot{z}_n &= \dot{z} - x_n \dot{\gamma} \cos \gamma + y_n \dot{\phi} \cos \phi - \dot{z}_n \doteq \dot{z} - x_n \dot{\gamma} + y_n \dot{\phi} - \dot{z}_n\end{aligned}\quad (3.12)$$

It should be pointed out that the present treatment of the kinematics of the wheel centers is different from that of [3.6] in which the wheel centers were regarded points in the vehicle body. Such a treatment, however, leads to the same expression for  $A_{cw,n}$ . Details of such an approach are presented in Appendix A.

### 3.4 Dynamics of Vehicle Body and Wheels.

Once the absolute accelerations at  $CG$  of the vehicle body and at  $CW_n$  of the wheel centers are determined, free-body diagrams (FBDs) should be sketched and Newton's second law of motion applied. In the derivations that follow, certain FBDs of [3.7] are utilized where appropriate. However, all equations of motion are re-developed. It is noted that all equations of motion are written with respect to the  $x$ - $y$ - $z$  coordinates.

### 3.4.1 Linear Motions of the Vehicle Body.

The reaction force exerted by a wheel center onto the lower end of the “spring-damper” combination is (see Figure 3.8, showing forces from wheels 2 and 3 only),

$$\mathbf{F}_n = P_{x_{cw,n}} \vec{i} + P_{y_{cw,n}} \vec{j} - P_{z_{cw,n}} \vec{k} \quad (3.13)$$

Therefore, the equations of motion are, by virtue of Newton’s second law of motion,

(1) for the linear motion in the longitudinal direction

$$M_b \ddot{x} = M_b \dot{y} \dot{\varphi} + \sum P_{x_{cw,n}} \quad (3.14)$$

(2) for the linear motion in the lateral direction

$$M_b \ddot{y} = -M_b \dot{x} \dot{\varphi} + \sum P_{y_{cw,n}} \quad (3.15)$$

and (3) for the linear motion in the vertical direction (or the bounce motion)

$$M_b \ddot{z} = M_b g - \sum P_{z_{cw,n}} \quad (3.16)$$

Note that in above equations, the summation is with respect to  $n$ , that is,  $\sum = \sum_{n=1}^4$ . This notation is used throughout the remainder of the thesis unless stated otherwise.

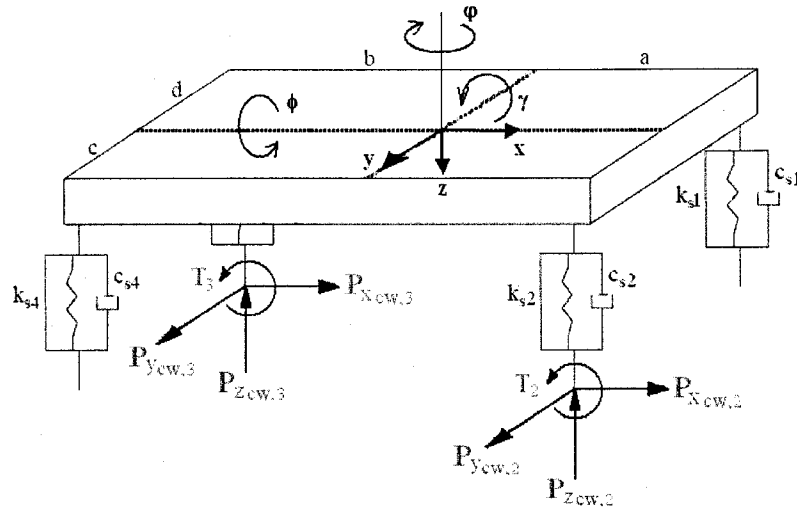


**Figure 3.8 FBD of vehicle body**  
(showing forces and torques from wheels 2 and 3 only)

### 3.4.2 Angular Motions of the Vehicle Body.

To arrive at the equations of motion for the angular motions of the vehicle body, one recognizes that the  $x$ - $y$ - $z$  frame is a rotating frame of reference. Since the frame rotates about the  $z$ -axis only (that is,  $\Omega_x = 0, \Omega_y = 0, \Omega_z = \dot{\phi}$ ), while the vehicle rotates relative to the  $x$ - $y$ - $z$  axes with the angular velocity components of  $[\dot{\phi}, \dot{\gamma}, 0]$ , the angular velocity components of the vehicle body are then  $\omega_x = \Omega_x + \dot{\phi} = \dot{\phi}$ ,  $\omega_y = \Omega_y + \dot{\gamma} = \dot{\gamma}$  and  $\omega_z = \Omega_z + 0 = \dot{\phi}$ . The equations of angular motion of the vehicle body are therefore

[3.8]

$$\sum \vec{M}_{cg} = \frac{d\vec{h}_{cg}}{dt} + \vec{\Omega} \times \vec{h}_{cg} \quad (3.17)$$

where the angular momentum about the  $CG$  is [3.7]

where the angular momentum about the CG is [3.7]

$$\begin{aligned}\vec{h}_{cg} = & (I_{x,cg}\omega_x - I_{xy,cg}\omega_y - I_{xz,cg}\omega_z)\vec{i} \\ & - (I_{yx,cg}\omega_x - I_{y,cg}\omega_y + I_{yz,cg}\omega_z)\vec{j} \\ & - (I_{zx,cg}\omega_x + I_{zy,cg}\omega_y - I_{z,cg}\omega_z)\vec{k}\end{aligned}\quad (3.18)$$

In equation (3.18),  $I_{x,cg}$ ,  $I_{y,cg}$  and  $I_{z,cg}$  are the mass moments of inertia of the vehicle body about the  $x$ -,  $y$ -, and  $z$ -axes, respectively. Terms such as  $I_{st,cg}$ , for example, denote the mass product of inertia of the vehicle body about the  $s$ - and  $t$ -axes, and  $I_{xy,cg} = I_{yx,cg}$ ,  $I_{yz,cg} = I_{zy,cg}$  and  $I_{zx,cg} = I_{xz,cg}$ . Since symmetry in the  $x$ - $y$  and  $y$ - $z$  planes can be reasonably assumed for most vehicles, this leads to  $I_{xy,cg} = I_{yx,cg} = I_{yz,cg} = I_{zy,cg} = 0$ .

Equation (3.18) then simplifies to

$$\vec{h}_{cg} = (I_{x,cg}\omega_x - I_{xz,cg}\omega_z)\vec{i} + I_{y,cg}\omega_y\vec{j} - (I_{zx,cg}\omega_x - I_{z,cg}\omega_z)\vec{k}\quad (3.19)$$

It is then recognized that  $I_{xz,cg}$ , or  $I_{zx,cg}$ , is either not available for most vehicles, or when available, is many orders of magnitude smaller than  $I_{x,cg}$ ,  $I_{y,cg}$  and  $I_{z,cg}$  and may be neglected. This leads to a further simplification of equation (3.19) that gives rise to

$$\vec{h}_{cg} = I_{x,cg}\omega_x\vec{i} + I_{y,cg}\omega_y\vec{j} + I_{z,cg}\omega_z\vec{k}\quad (3.20)$$

Substituting equation (3.20) into (3.17) yields,

$$\begin{aligned}\sum M_{x,cg} &= I_{x,cg}\dot{\omega}_x - I_{y,cg}\omega_y\Omega_z = I_{x,cg}\ddot{\phi} - I_{y,cg}\dot{\gamma}\dot{\phi} \\ \sum M_{y,cg} &= I_{y,cg}\dot{\omega}_y + I_{x,cg}\omega_x\Omega_z = I_{y,cg}\ddot{\gamma} + I_{x,cg}\dot{\phi}\dot{\phi} \\ \sum M_{z,cg} &= I_{z,cg}\dot{\omega}_z = I_{z,cg}\ddot{\phi}\end{aligned}\quad (3.21)$$

where the left hand sides (LHS) represent the sums of moments due to forces about the  $x$ -,  $y$ -, and  $z$ -axes, respectively. The angular motion about the longitudinal  $x$ -axis (or the roll motion) is then governed by

$$\begin{aligned} I_{x,cg}\ddot{\phi} &= I_{y,cg}\dot{\gamma}\dot{\phi} - \sum [P_{z_{cw,n}} y_n] \cos \phi - \sum [P_{y_{cw,n}} z_{w,n}] \\ &\doteq I_{y,cg}\dot{\gamma}\dot{\phi} - \sum [P_{z_{cw,n}} y_n] - \sum [P_{y_{cw,n}} z_{w,n}] \end{aligned} \quad (3.22)$$

the angular motion about the lateral  $y$ -axis (or the pitch motion) by

$$\begin{aligned} I_{y,cg}\ddot{\gamma} &= -I_{x,cg}\dot{\phi}\dot{\gamma} + \sum T_n + \sum [P_{z_{cw,n}} x_n] \cos \gamma + \sum [P_{x_{cw,n}} z_{w,n}] \\ &\doteq -I_{x,cg}\dot{\phi}\dot{\gamma} + \sum T_n + \sum [P_{z_{cw,n}} x_n] + \sum [P_{x_{cw,n}} z_{w,n}] \end{aligned} \quad (3.23)$$

and the angular motion about the vertical  $z$ -axis (or the yaw motion) by

$$I_{z,cg}\ddot{\psi} = -\sum [P_{x_{cw,n}} y_n] + \sum [P_{y_{cw,n}} x_n] \quad (3.24)$$

The FBD of the vehicle body as viewed from the  $x$ -axis,  $y$ -axis and the top is given in Figure 3.9. In equations (3.22) and (3.23),  $z_{w,n} = z_n + H - z$  is the  $z$ -coordinate difference between the  $CG$  and a wheel center at time  $t$ .  $H$  is the initial  $z$ -coordinate difference, see Figure 3.10. Obviously,  $z(0) = z_n(0) = 0$ .

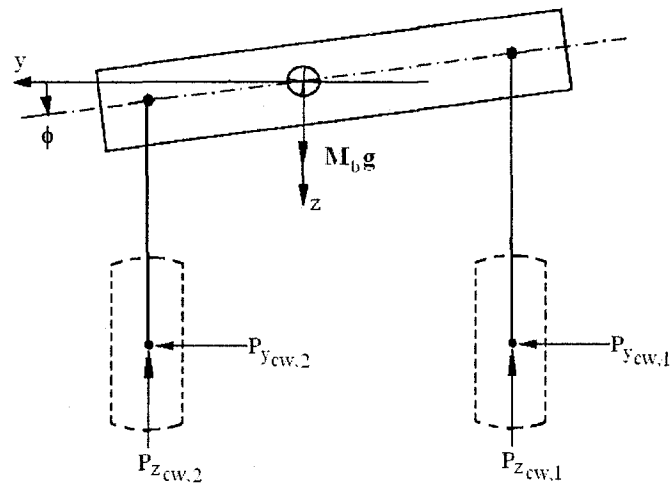


**Figure 3.9a** FBD of the vehicle body as viewed along the  $x$ -axis  
(wheels included for reference only)

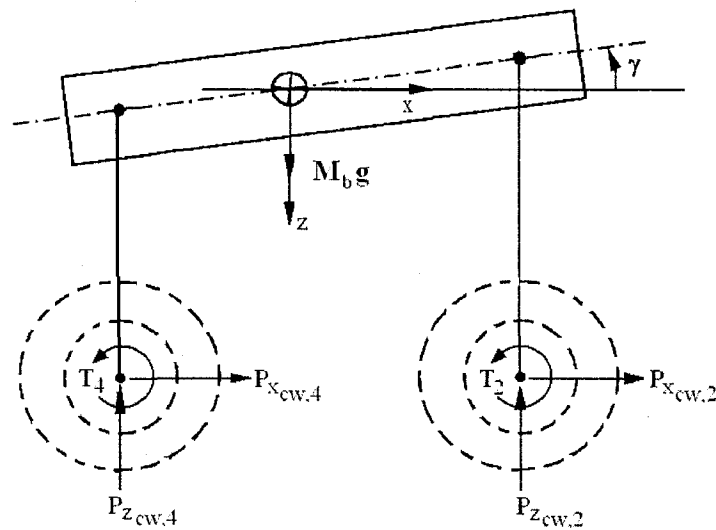


**Figure 3.9b** FBD of the vehicle body as viewed along the  $y$ -axis  
(wheels included for reference only)

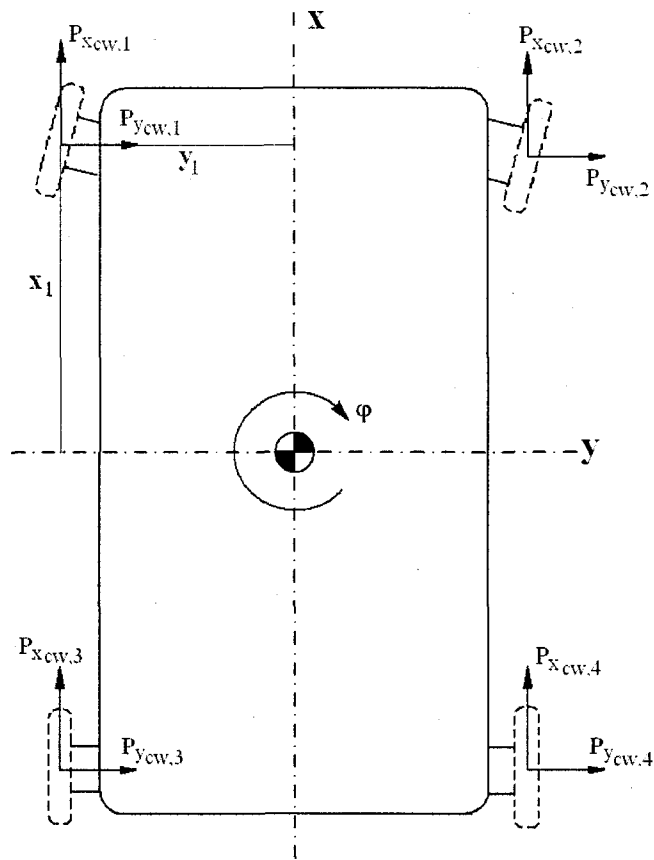


**Figure 3.9c FBD of the vehicle body as viewed along the top (wheels included for reference only)**

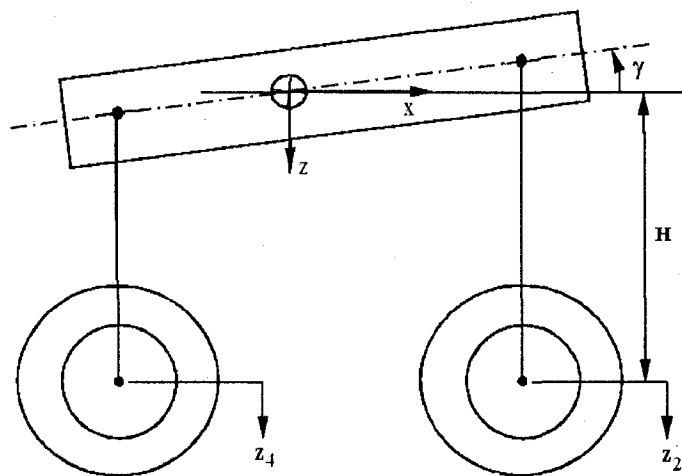


**Figure 3.10 Vehicle body as viewed along the y-axis showing  $H$ ,  $z$  and  $z_n$**

### 3.4.3 Forces on the Wheel Base and Equations of Motion of the Wheels.

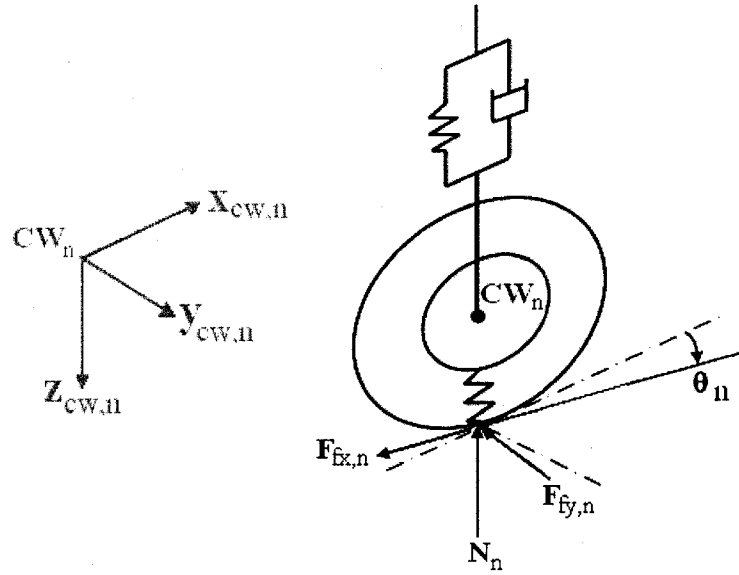


**Figure 3.11 Forces exerted by road surface onto the wheel bases**

Reaction force exerted by the road surface onto a wheel base is (Figure 3.11)

$$\begin{aligned}
 \vec{F}_{bw,n} &= -F_{fx,n} \vec{i}_{bw,n} - F_{fy,n} \vec{j}_{bw,n} - N_n \vec{k}_{bw,n} \\
 &= (-F_{fx,n} \cos \theta_n + F_{fy,n} \sin \theta_n) \vec{i}_{cw,n} \\
 &\quad + (-F_{fx,n} \sin \theta_n - F_{fy,n} \cos \theta_n) \vec{j}_{cw,n} - N_n \vec{k}_{cw,n}
 \end{aligned} \tag{3.25}$$

where equation (3.2) has been applied. With the FBD of a wheel (Figure 3.12), applying

Newton's second law of motion, the equations of motion of the wheel center are,

(1) for the linear motion in the longitudinal direction

$$[\ddot{x} - \dot{\varphi} y_n] m_n = [\dot{\varphi} \dot{y} + \dot{\varphi}^2 x_n] m_n - P_{x_{cw,n}} - F_{fx,n} \cos \theta_n + F_{fy,n} \sin \theta_n \tag{3.26}$$

(2) for the linear motion in the lateral direction

$$[\dot{y} + \dot{\varphi} x_n] m_n = -[\dot{\varphi} \dot{x} - \dot{\varphi}^2 y_n] m_n - P_{y_{cw,n}} - F_{fx,n} \sin \theta_n - F_{fy,n} \cos \theta_n \tag{3.27}$$

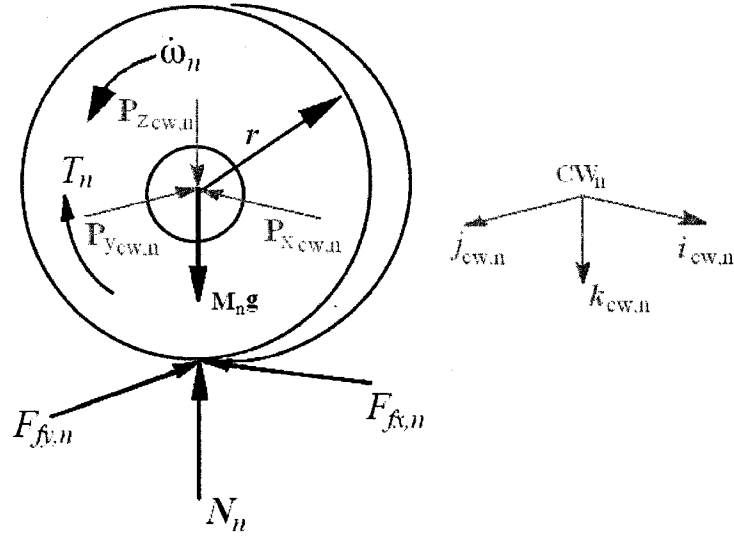


**Figure 3.12 FBD of a wheel**

(3) for the linear motion in the vertical motion

$$m_n \ddot{z}_n = P_{z,cw,n} + m_n g - N_n \quad (3.28)$$

and (4) for the spin motion of the wheel, by considering the spin axis of a wheel (spin axis passes through the wheel center and is parallel to  $y_{bw,n}$ .)

$$I_{spin} \dot{\omega}_n = -r F_{fx,n} - T_n \quad (3.29)$$

It is observed that the LHS of equations (3.26) and (3.27) each involves two acceleration terms. On the other hand, equations (3.28) and (3.29) do not exhibit the coupling between accelerations. Obviously, existence of such coupling complicates equation solving.

#### 3.4.4 Forces Developed in the Spring-Damper Combinations.

All “spring-damper” combinations considered are assumed massless. Equilibrium of each in the vertical direction yields

$$P_{z_{cw,n}} = P_{z_{cw,n}}^0 + k_{sn} (z - x_n \gamma + y_n \phi - z_n) + c_{sn} (\dot{z} - x_n \dot{\gamma} + y_n \dot{\phi} - \dot{z}_n) \quad (3.30)$$

where  $k_{sn}$ ,  $c_{sn}$  are the spring constant and damping coefficient of the spring-damper combination,  $P_{z_{cw,n}}^0$  is the initial spring force required to support the vehicle body weight

$M_b g$ . It is found that

$$\begin{aligned} P_{z_{cw,1}}^0 &= M_b g \frac{b}{l} \frac{d}{w}, P_{z_{cw,2}}^0 = M_b g \frac{b}{l} \frac{c}{w}, P_{z_{cw,3}}^0 = M_b g \frac{a}{l} \frac{d}{w}, P_{z_{cw,4}}^0 = M_b g \frac{a}{l} \frac{c}{w}, \\ \therefore \sum_{n=1}^4 P_{z_{cw,n}}^0 &= M_b g. \end{aligned} \quad (3.31)$$

with  $l = a + b$ , and  $w = c + d$  being the wheelbase and track width, respectively. The  $x$ -

and  $y$ - components of the forces are determined as follows, from equations (3.26) and

(3.27)

$$P_{x_{cw,n}} = [-\ddot{x} + \ddot{\phi} y_n + \dot{\phi} \dot{y} + \dot{\phi}^2 x_n] m_n - F_{fx,n} \cos \theta_n + F_{fy,n} \sin \theta_n \quad (3.32)$$

$$P_{y_{cw,n}} = [-\ddot{y} - \ddot{\phi} x_n - \dot{\phi} \dot{x} + \dot{\phi}^2 y_n] m_n - F_{fx,n} \sin \theta_n - F_{fy,n} \cos \theta_n \quad (3.33)$$

#### 3.4.5 Forces Developed in the Contact Points Between a Wheel and Road Surface.

If  $k_{tn}$  is the tire's stiffness and  $z_{sn}$  the road profile, respectively, equilibrium in the vertical  $z$ -direction yields (Figure 3.13)

$$N_n = P_{z_{cw,n}}^0 + m_n g + k_{tn}(z_n - z_{sn}) \quad (3.34)$$

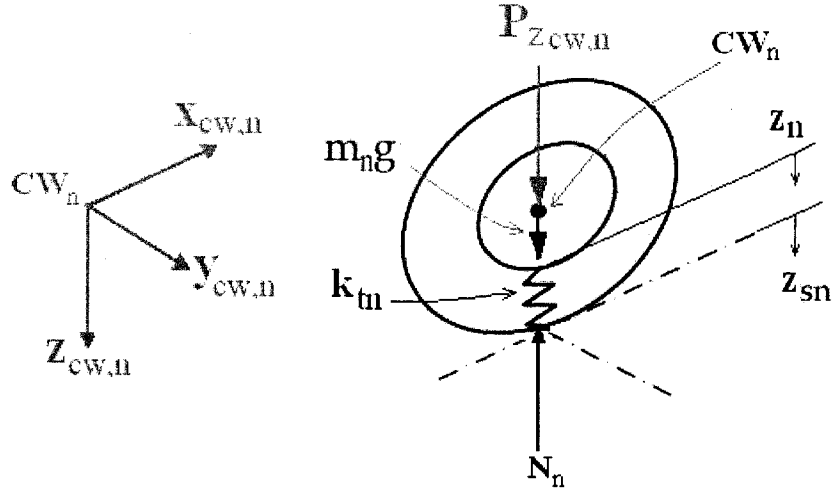


**Figure 3.13 Free body diagram of a wheel  
(showing only forces in the z-direction)**

#### 3.4.6 Bounce and Spin Motions of the Wheels.

Substituting equations (3.30) and (3.34) into (3.28) yields,

$$\begin{aligned} m_n \ddot{z}_n &= k_{sn} z - (k_{sn} + k_{tn}) z_n - k_{sn} (x_n \gamma - y_n \phi) \\ &+ c_{sn} \dot{z} - c_{sn} \dot{z}_n - c_{sn} (x_n \dot{\gamma} - y_n \dot{\phi}) + k_{tn} z_{sn} \end{aligned} \quad (3.35)$$

and equation (3.29) is repeated here for easy reference.

$$I_{spin} \dot{\omega}_n = -r F_{fx,n} - T_n \quad (3.36)$$

#### 3.4.7 Bounce Motion of the Vehicle Body.

Substitution of equation (3.30) into (3.16) gives,

$$M_b \ddot{z} = -\sum [k_{sn} (z + y_n \phi - x_n \gamma - z_n) + c_{sn} (\dot{z} + y_n \dot{\phi} - x_n \dot{\gamma} - \dot{z}_n)] \quad (3.37)$$

It is noted that the four equations governing  $\ddot{z}_n$  (equation 3.35) and  $\dot{\omega}_n$  (equation 3.36), and the equation governing  $\ddot{z}$  (equation 3.37) are not coupled to one another. This, however, is not the case with the longitudinal, lateral, roll, pitch and yaw motions of the vehicle as demonstrated by equations (3.38)-(3.42) given below.

#### 3.4.8 Longitudinal, Lateral, Roll, Pitch and Yaw Motions of the Vehicle Body.

Defining  $M_{tot} = M_b + \sum m_n$  which is the total mass including that of the vehicle and those of the wheels. Substituting equation (3.32) into (3.14) yields

$$\begin{aligned} & M_{tot}\ddot{x} - \sum [y_n m_n] \ddot{\phi} \\ & = M_b \dot{y} \dot{\phi} - \sum (F_{fx,n} \cos \theta_n - F_{fy,n} \sin \theta_n) + \sum [\dot{\phi} \dot{y} + \dot{\phi}^2 x_n] m_n \end{aligned} \quad (3.38)$$

Substituting equation (3.33) into (3.15) results in,

$$\begin{aligned} & M_{tot}\ddot{y} + \sum [x_n m_n] \ddot{\phi} \\ & = -M_b \dot{x} \dot{\phi} - \sum (F_{fx,n} \sin \theta_n + F_{fy,n} \cos \theta_n) - \sum [\dot{\phi} \dot{x} - \dot{\phi}^2 y_n] m_n \end{aligned} \quad (3.39)$$

Substituting equations (3.30) and (3.33) into (3.22) gives,

$$\begin{aligned} & -\sum [z_{w,n} m_n] \ddot{y} - \sum [x_n z_{w,n} m_n] \ddot{\phi} + I_{x,cg} \ddot{\phi} \\ & = I_{y,cg} \dot{\gamma} \dot{\phi} + \sum [(F_{fx,n} \sin \theta_n + F_{fy,n} \cos \theta_n) z_{w,n}] \\ & - \sum \{ [k_{sn}(z - x_n \gamma + y_n \phi - z_n)] y_n \} - \sum \{ [c_{sn}(\dot{z} - x_n \dot{\gamma} + y_n \dot{\phi} - \dot{z}_n)] y_n \} \\ & + \sum \{ [\dot{\phi} \dot{x} - \dot{\phi}^2 y_n] z_{w,n} m_n \} \end{aligned} \quad (3.40)$$

Substituting equations (3.30) and (3.32) into (3.23) results in,

$$\begin{aligned}
& \sum [z_{w,n} m_n] \ddot{x} - \sum [y_n z_{w,n} m_n] \ddot{\phi} + I_{y,cg} \ddot{\gamma} \\
&= -I_{x,cg} \dot{\phi} \dot{\phi} + \sum T_n - \sum [(F_{fx,n} \cos \theta_n - F_{fy,n} \sin \theta_n) z_{w,n}] \\
&+ \sum \{ [k_{sn}(z - x_n \gamma + y_n \phi - z_n)] x_n \} + \sum \{ [c_{sn}(\dot{z} - x_n \dot{\gamma} + y_n \dot{\phi} - \dot{z}_n)] x_n \} \\
&+ \sum \{ [\dot{\phi} \dot{y} + \dot{\phi}^2 x_n] z_{w,n} m_n \}
\end{aligned} \tag{3.41}$$

And substituting equations (3.32) and (3.33) into (3.24) yields,

$$\begin{aligned}
& -\sum [y_n m_n] \ddot{x} + \sum [x_n m_n] \ddot{y} + \{ I_{z,cg} + \sum [(x_n^2 + y_n^2) m_n] \} \ddot{\phi} \\
&= -\sum [(F_{fx,n} \sin \theta_n + F_{fy,n} \cos \theta_n) x_n] + \sum [(F_{fx,n} \cos \theta_n - F_{fy,n} \sin \theta_n) y_n] \\
&- \sum \{ [\dot{\phi} \dot{x} - \dot{\phi}^2 y_n] (x_n m_n) \} - \sum \{ [\dot{\phi} \dot{y} + \dot{\phi}^2 x_n] (y_n m_n) \}
\end{aligned} \tag{3.42}$$

Equations (3.38) through (3.42) form a set of five simultaneous equations that can

be recast into the following matrix form,

$$\begin{bmatrix} a_{11} & & & & a_{15} \\ & a_{22} & & & a_{25} \\ & & a_{32} & a_{33} & a_{35} \\ a_{41} & & & a_{44} & a_{45} \\ a_{51} & a_{52} & & & a_{55} \end{bmatrix} \begin{bmatrix} \ddot{x} \\ \ddot{y} \\ \ddot{\phi} \\ \ddot{\gamma} \\ \ddot{\phi} \end{bmatrix} = \begin{bmatrix} b_1 \\ b_2 \\ b_3 \\ b_4 \\ b_5 \end{bmatrix} \tag{3.43}$$

where the nonzero elements are

$$\begin{aligned}
a_{11} &= a_{22} = M_{tot} \\
a_{15} &= a_{51} = -\sum [y_n m_n] \\
a_{25} &= a_{52} = \sum [x_n m_n] \\
a_{32} &= -a_{41} = -\sum [z_{w,n} m_n] \\
a_{33} &= I_{x,cg} \\
a_{35} &= -\sum [x_n z_{w,n} m_n] \\
a_{44} &= I_{y,cg} \\
a_{45} &= -\sum [y_n z_{w,n} m_n] \\
a_{55} &= I_{z,cg} + \sum [(x_n^2 + y_n^2) m_n]
\end{aligned} \tag{3.44a}$$

and

$$b_1 = M_b \dot{y} \dot{\phi} + \sum [\dot{\phi} \dot{y} + \dot{\phi}^2 x_n] m_n - \sum (F_{fx,n} \cos \theta_n - F_{fy,n} \sin \theta_n) \quad (3.44b)$$

$$b_2 = -M_b \dot{x} \dot{\phi} - \sum [\dot{\phi} \dot{x} - \dot{\phi}^2 y_n] m_n - \sum (F_{fx,n} \sin \theta_n + F_{fy,n} \cos \theta_n) \quad (3.44c)$$

$$\begin{aligned} b_3 &= I_{y,cg} \dot{\gamma} \dot{\phi} + \sum \{ [\dot{\phi} \dot{x} - \dot{\phi}^2 y_n] z_{w,n} m_n \} \\ &+ \sum \{ [(F_{fx,n} \sin \theta_n + F_{fy,n} \cos \theta_n) z_{w,n}] \\ &- \sum \{ [k_{sn}(z - x_n \gamma + y_n \phi - z_n)] y_n \} \\ &- \sum \{ [c_{sn}(\dot{z} - x_n \dot{\gamma} + y_n \dot{\phi} - \dot{z}_n)] y_n \} \end{aligned} \quad (3.44d)$$

$$\begin{aligned} b_4 &= -I_{x,cg} \dot{\phi} \dot{\phi} + \sum \{ [\dot{\phi} \dot{y} + \dot{\phi}^2 x_n] z_{w,n} m_n \} \\ &+ \sum T_n - \sum \{ [(F_{fx,n} \cos \theta_n - F_{fy,n} \sin \theta_n) z_{w,n}] \\ &+ \sum \{ [k_{sn}(z - x_n \gamma + y_n \phi - z_n)] x_n \} \\ &+ \sum \{ [c_{sn}(\dot{z} - x_n \dot{\gamma} + y_n \dot{\phi} - \dot{z}_n)] x_n \} \end{aligned} \quad (3.44e)$$

$$\begin{aligned} b_5 &= \sum \{ [(F_{fx,n} \cos \theta_n - F_{fy,n} \sin \theta_n) y_n] \\ &- \sum \{ [(F_{fx,n} \sin \theta_n + F_{fy,n} \cos \theta_n) x_n] \\ &- \sum \{ [\dot{\phi} \dot{x} - \dot{\phi}^2 y_n] (x_n m_n) \} \\ &- \sum \{ [\dot{\phi} \dot{y} + \dot{\phi}^2 x_n] (y_n m_n) \} \end{aligned} \quad (3.44f)$$

The 5x5 coefficient matrix [A] of equation (3.43) is rank-sufficient. In fact, by inputting the matrix into the symbolic computation software MAPLE [3.9] (see Figure 3.14a), the matrix can be inverted analytically (see Figure 3.14b, where the five separate rows vectors represent each row elements of the [A]<sup>-1</sup> matrix). Or it can be inverted numerically depending on computational effectiveness. Note that the [A] matrix is time-varying (see, for example, elements  $a_{35}$  and  $a_{45}$ ) which requires inversion at every

time step of integration. Following inversion, the five equations become decoupled. The

linear and angular accelerations can then be determined. That is

$$\begin{bmatrix} \ddot{x} & \ddot{y} & \ddot{\phi} & \ddot{\gamma} & \ddot{\psi} \end{bmatrix}^T = [A]^{-1} \begin{bmatrix} b_1 & b_2 & b_3 & b_4 & b_5 \end{bmatrix}^T \quad (3.45)$$

$$\begin{bmatrix} a_{11} & 0 & 0 & 0 & a_{15} \\ 0 & a_{11} & 0 & 0 & a_{25} \\ 0 & a_{32} & a_{33} & 0 & a_{35} \\ -a_{32} & 0 & 0 & a_{44} & a_{45} \\ a_{15} & a_{25} & 0 & 0 & a_{55} \end{bmatrix}$$

**Figure 3.14a** [A] Matrix as inputted into MAPLE

$$\begin{bmatrix} \frac{a_{11} a_{55} - a_{25}^2}{a_{11} (a_{11} a_{55} - a_{15}^2 - a_{25}^2)}, \frac{a_{15} a_{25}}{a_{11} (a_{11} a_{55} - a_{15}^2 - a_{25}^2)}, 0, 0, \\ -\frac{a_{15}}{a_{11} a_{55} - a_{15}^2 - a_{25}^2} \end{bmatrix}$$

$$\begin{bmatrix} \frac{a_{15} a_{25}}{a_{11} (a_{11} a_{55} - a_{15}^2 - a_{25}^2)}, \frac{a_{11} a_{55} - a_{15}^2}{a_{11} (a_{11} a_{55} - a_{15}^2 - a_{25}^2)}, 0, 0, \\ -\frac{a_{25}}{a_{11} a_{55} - a_{15}^2 - a_{25}^2} \end{bmatrix}$$

$$\begin{bmatrix} -\frac{a_{15} (-a_{11} a_{35} + a_{32} a_{25})}{a_{33} a_{11} (a_{11} a_{55} - a_{15}^2 - a_{25}^2)}, -\frac{a_{11} a_{32} a_{55} - a_{11} a_{25} a_{35} - a_{32} a_{15}^2}{a_{33} a_{11} (a_{11} a_{55} - a_{15}^2 - a_{25}^2)}, \\ \frac{1}{a_{33}}, 0, \frac{-a_{11} a_{35} + a_{32} a_{25}}{a_{33} (a_{11} a_{55} - a_{15}^2 - a_{25}^2)} \end{bmatrix}$$

$$\begin{bmatrix} \frac{a_{11} a_{32} a_{55} + a_{11} a_{15} a_{45} - a_{32} a_{25}^2}{a_{44} a_{11} (a_{11} a_{55} - a_{15}^2 - a_{25}^2)}, \frac{a_{25} (a_{11} a_{45} + a_{32} a_{15})}{a_{44} a_{11} (a_{11} a_{55} - a_{15}^2 - a_{25}^2)}, 0, \\ \frac{1}{a_{44}}, -\frac{a_{11} a_{45} + a_{32} a_{15}}{a_{44} (a_{11} a_{55} - a_{15}^2 - a_{25}^2)} \end{bmatrix}$$

$$\begin{bmatrix} -\frac{a_{15}}{a_{11} a_{55} - a_{15}^2 - a_{25}^2}, -\frac{a_{25}}{a_{11} a_{55} - a_{15}^2 - a_{25}^2}, 0, 0, \\ \frac{a_{11}}{a_{11} a_{55} - a_{15}^2 - a_{25}^2} \end{bmatrix}$$

**Figure 3.14b** [A]<sup>-1</sup> Matrix as determined by MAPLE

Now that the entire set of 14 equations of motion, equations (3.35), (3.36), (3.37) and (3.45) with  $n = 1, \dots, 4$ , are defined, they will be rewritten in the state variable format, with the 28 state variables being  $z_1, z_2, z_3, z_4, \omega_1, \omega_2, \omega_3, \omega_4, z, x, y, \phi, \gamma, \varphi, \dot{z}_1, \dot{z}_2, \dot{z}_3, \dot{z}_4, \dot{\omega}_1, \dot{\omega}_2, \dot{\omega}_3, \dot{\omega}_4, \dot{z}, \dot{x}, \dot{y}, \dot{\phi}, \dot{\gamma}, \dot{\varphi}$ . Of these state variables, the vehicle body velocities  $\dot{x}, \dot{y}$  are velocities written in terms of the local (vehicle body) coordinates. They should be transformed to the global (earth-fixed) coordinates as follows

$$\begin{aligned}\dot{X} &= \dot{x} \cos \varphi - \dot{y} \sin \varphi \\ \dot{Y} &= \dot{x} \sin \varphi + \dot{y} \cos \varphi\end{aligned}\tag{3.46}$$

such that the 28 state variables are now  $z_1, z_2, z_3, z_4, \omega_1, \omega_2, \omega_3, \omega_4, z, X, Y, \phi, \gamma, \varphi, \dot{z}_1, \dot{z}_2, \dot{z}_3, \dot{z}_4, \dot{\omega}_1, \dot{\omega}_2, \dot{\omega}_3, \dot{\omega}_4, \dot{z}, \dot{X}, \dot{Y}, \dot{\phi}, \dot{\gamma}, \dot{\varphi}$ . They can then be solved for by numerically integrating the 28 first-order ordinary differential equations (ODEs) by a ODE solver such as the 4-th order Runge-Kutta method. It should be noted that in equation (3.46),  $\varphi$  is the yaw angle which is a state variable and is the integral of yaw rate over the time interval  $t_0$  to  $t$ ,

$$\text{i.e., } \varphi = \int_{t_0}^t \dot{\varphi} dt.$$

### 3.5 Simplification of the 14-DOF Full-Car Model.

In this section, the versatility of the previously presented full-car model will be demonstrated. The full-car model will be simplified to various car models available in the literature, ranging from quarter-car models and half-car models to other full-car models.

Most of the models have been surveyed or reviewed in Chapter 2. For easy reference, they will be recited and renumbered. It should be noted that, in Figure 3.15 through 3.18, the symbols have been changed, from what were used in the respective references, to those used in the thesis. This is done with consistency in mind.

### 3.5.1 Simplification to Quarter-Car Models

Quarter-car models, which include just one wheel and the associated suspension and the vehicle body mass, are widely used for suspension analysis. A quarter-car model can be obtained by neglecting friction and by setting  $x = y = \phi = \gamma = \varphi = \dot{x} = \dot{y} = \dot{\phi} =$

$$\dot{\gamma} = \dot{\varphi} = \ddot{x} = \ddot{y} = \ddot{\phi} = \ddot{\gamma} = \ddot{\varphi} = 0, \dot{\gamma} = \dot{\varphi} = \ddot{x} = \ddot{y} = \ddot{\phi} = \ddot{\gamma} = \ddot{\varphi} = 0,$$

$$m_n = M_w, k_{sn} = k_s, c_{sn} = c_s, k_{tn} = k_t, z_{sn} = z_s, z_n = z_w, \dot{z}_n = \dot{z}_w, T_n = 0. \text{ Equations}$$

(3.35) through (3.42) are then reduced to

$$M_w \ddot{z}_w = k_s (z - z_w) + c_s (\dot{z} - \dot{z}_w) + k_t (z_s - z_w) \quad (3.47a)$$

$$M_b \ddot{z} = -4 [k_s (z - z_w) + c_s (\dot{z} - \dot{z}_w)] \quad (3.47b)$$

It is further found that equations (3.36) and (3.38) through (3.42) are identically equal to zero. Since the sprung mass is  $M_s = M_b / 4$ , un-sprung mass is the wheel mass  $M_w$ , one then has

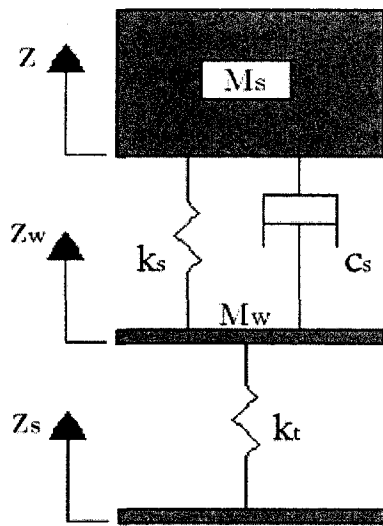


**Figure 3.15** A quarter-car model [3.13]

$$M_w \ddot{z}_w = k_s(z - z_w) + c_s(\dot{z} - \dot{z}_w) + k_t(z_s - z_w) \quad (3.48)$$

$$M_s \ddot{z} = -[k_s(z - z_w) + c_s(\dot{z} - \dot{z}_w)] \quad (3.49)$$

Equations (3.48) and (3.49) are identical to equation (2.1) of [3.10] and equation (8) of [3.11] respectively, and equations (2.1) and (2.2) of [3.12]. A typical quarter-car model [3.13] is illustrated in Figure 3.15.

### 3.5.2 Simplification to Pitch-Bounce Half-Car Models

Half-car models typically include the so-called pitch-bounce models, the roll-bounce models and the roll-yaw models [3.10]. The pitch-bounce models represent the left- or right-half of the vehicle, or two axles of the vehicle. The roll-bounce models consist of the front- or rear-half of the vehicle, or a single axle. Both the pitch-bounce and the roll-bounce models include the bounce motions of the vehicle and wheels. To the contrast, the roll-yaw models have no bounce motions [3.10], including instead only the lateral motions as the DOFs of the models. The more general roll-yaw models are not discussed here because torsional deflections in the suspensions have also not been considered; and

steering angles have also not been included as DOFs of the system. A typical pitch-bounce model is shown in Figure 3.16.

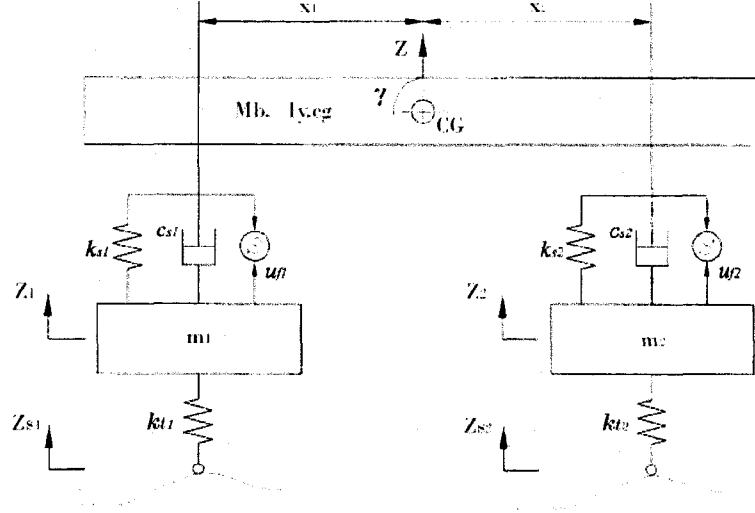


**Figure 3.16** A half-car model showing pitch and bounce motions [3.14]

Setting  $x = y = \phi = \varphi = \dot{x} = \dot{y} = \dot{\phi} = \dot{\varphi} = \ddot{x} = \ddot{y} = \ddot{\phi} = \ddot{\varphi} = 0, T_n = \omega_n = \dot{\omega}_n =$

$F_{fx,n} = F_{fy,n} = 0$ , and considering only the vertical force components from the

suspensions, equations of motion (3.35) through (3.42) are reduced to,

$$m_n \ddot{z}_n = k_{sn}(z - z_n - x_n \gamma) + c_{sn}(\dot{z} - \dot{z}_n - x_n \dot{\gamma}) + k_{tn}(z_{sn} - z_n) \quad (3.50)$$

$$M_b \ddot{z} = -\sum [k_{sn}(z - z_n - x_n \gamma) + c_{sn}(\dot{z} - \dot{z}_n - x_n \dot{\gamma})] \quad (3.51)$$

$$I_{y,CG} \ddot{\gamma} = \sum \{ [k_{sn}(z - z_n - x_n \gamma) + c_{sn}(\dot{z} - \dot{z}_n - x_n \dot{\gamma})] x_n \} \quad (3.52)$$

Equations (3.36), (3.38), (3.39), (3.40) and (3.42) are identically equal to zero. Note

that Equations (3.50), (3.51) and (3.52) are identical to equations (1a), (1b), (1c) and (1d)

of [3.14].

### 3.5.3 Simplification to Roll-Bounce Half-Car Models

Mathematically, the roll-bounce models are not very different from the pitch-bounce models. The assumptions are  $x = y = \gamma = \varphi = \dot{x} = \dot{y} = \dot{\gamma} = \dot{\varphi} = \ddot{x} = \ddot{y} = \ddot{\gamma} = \ddot{\varphi} = 0$ ,  $F_{fx,n} = F_{fy,n} = T_n = \omega_n = \dot{\omega}_n = 0$ . The equations of motion for this case reduce to

$$m_n \ddot{z}_n = k_{sn}(z - z_n + y_n \phi) + c_{sn}(\dot{z} - \dot{z}_n + y_n \dot{\phi}) + k_{tn}(z_{sn} - z_n) \quad (3.53)$$

$$M_b \ddot{z} = -\sum [k_{sn}(z - z_n + y_n \phi) + c_{sn}(\dot{z} - \dot{z}_n + y_n \dot{\phi})] \quad (3.54)$$

$$I_{x,cg} \ddot{\phi} = -\sum \{ [k_{sn}(z - z_n + y_n \phi) + c_{sn}(\dot{z} - \dot{z}_n + y_n \dot{\phi})] y_n \} \quad (3.55)$$

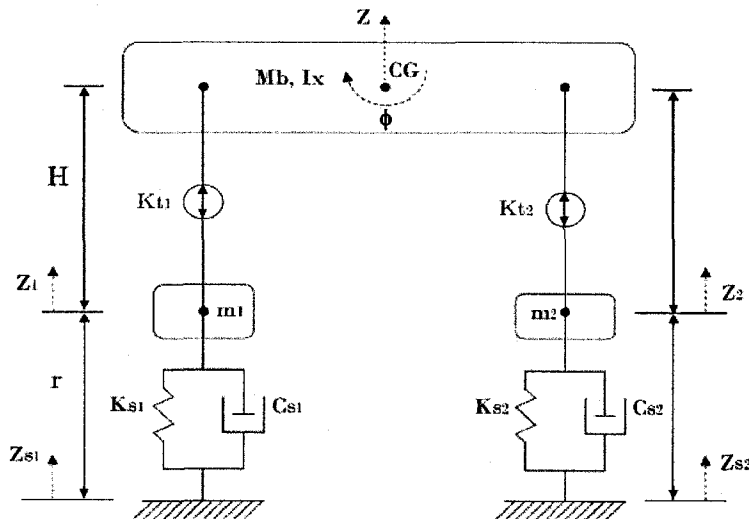


Figure 3.17 A half-car model showing roll and bounce motions [3.15]

A roll-bounce half-car model is shown in Figure 3.17. Physically pitch-bounce and roll-bounce models are however different and serve different purposes. Though both can be used to analyze suspensions, the roll-bounce models enable the investigation of

rollover of vehicles; while the pitch-bounce models are appropriate for ride comfort analysis.

### 3.5.4 Simplification to a 7-DOF Full-Car Models.

The 7-DOF full-car model is often studied ([3.12, 3.16, 3.18], and with the seat bounce excluded in [3.17, 3.19]). These DOFs are shown in Figure 3.18, including the bounces of the vehicle body and the wheels, respectively, and roll and pitch. To simplify the 14-DOF model to the 7-DOF one, one needs to set  $x = y = \varphi = \dot{x} = \dot{y} = \dot{\varphi} = \ddot{x} = \ddot{y} = \ddot{\varphi} = 0$ ,

$T_n = \omega_n = \dot{\omega}_n = F_{fx,n} = F_{fy,n} = 0$ . As a result, the equations of motion become,

$$m_n \ddot{z}_n = k_{sn}(z - z_n - x_n \gamma + y_n \phi) + c_{sn}(\dot{z} - \dot{z}_n - x_n \dot{\gamma} + y_n \dot{\phi}) + k_{tn}(z_{sn} - z_n) \quad (3.56)$$

$$M_b \ddot{z} = -\sum [k_{sn}(z - z_n + y_n \phi - x_n \gamma) + c_{sn}(\dot{z} - \dot{z}_n + y_n \dot{\phi} - x_n \dot{\gamma})] \quad (3.57)$$

$$I_{x,cg} \ddot{\phi} = -\sum \{ [k_{sn}(z - z_n - x_n \gamma + y_n \phi) + c_{sn}(\dot{z} - \dot{z}_n - x_n \dot{\gamma} + y_n \dot{\phi})] y_n \} \quad (3.58)$$

$$I_{y,cg} \ddot{\gamma} = \sum \{ [k_{sn}(z - z_n - x_n \gamma + y_n \phi) + c_{sn}(\dot{z} - \dot{z}_n - x_n \dot{\gamma} + y_n \dot{\phi})] x_n \} \quad (3.59)$$

Equation (3.36), (3.38), (3.39) and (3.42) are identically equal to zero. Equation (3.56), (3.57), (3.58) and (3.59) hence form the equations of motion of the model.

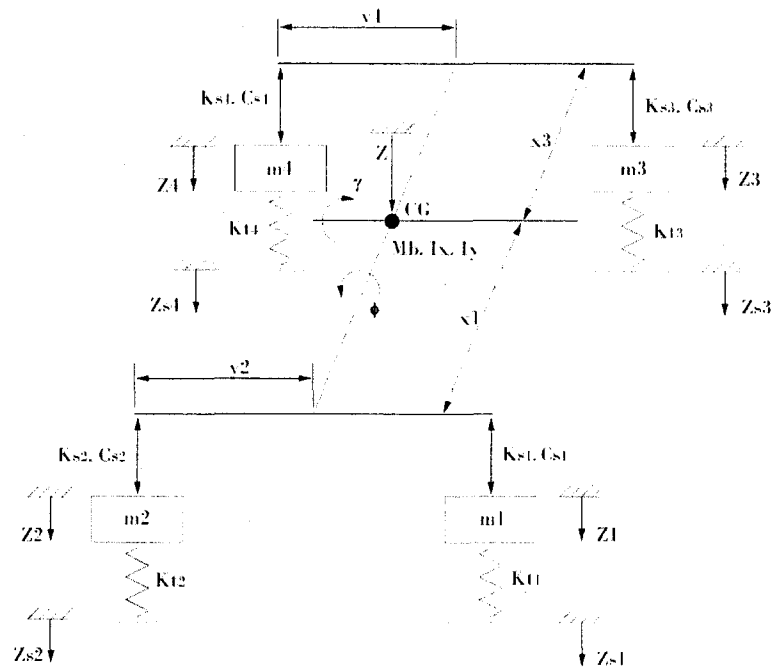


Figure 3.18 A 7-DOF full-car Model [3.12]

### 3.6 Concluding Remarks.

In this chapter, a 14-DOF full-car dynamic model has been developed. The resulting equations of motion are equations (3.35) through (3.42). The last five equations, (3.38) through (3.42), are coupled and have to be solved simultaneously.

The full car model can be simplified to (1) a quarter-car model defined by equations (3.48) and (3.49); (2) a pitch-bounce half-car model defined by equations (3.50) – (3.52); (3) a roll-bounce half-car model defined by equations (3.53) – (3.55); and (4) a 7-DOF full-car model defined by equations (3.56) – (3.59). These simplified models will be

tested with results presented in Chapters 5 and 6. Before proceeding, however, the modeling of friction forces has to be dealt with.

## CHAPTER 4

### ROAD-TIRE FRICTION

So far all necessary components of the dynamic model of a vehicle have been considered with the exception of the friction force. As was concluded in Section 3.5, vehicle motion is primarily determined by the interaction forces between the tires and the road, or the road contact forces. Therefore, one of the crucial elements of vehicle modeling is to properly model the road-tire friction force.

This chapter deals with this crucial element of road-tire friction. A brief literature review will first be given, followed by the details of the 1-D and 2-D LuGre dynamic friction models. For purpose of comparison other friction models such as the “Magic Formula” and the 3-D brush model are also looked at. The chapter concludes with formulation needed to incorporate the 2-D LuGre friction model into the dynamic full-car model that was presented in Chapter 3.

#### **4.1 Literature Review.**

The behavior of road-tire friction is well known to be highly nonlinear. Many friction models have been proposed attempting to capture the essence of the complicated friction phenomena with reasonable complexity [4.1]. Since there is a wide range of physical

phenomena that cause friction, from elastic and plastic deformations, to fluid mechanics, etc., the nature of the models is quite different. They can be static or dynamic. They can be described by differential equations, differential-algebraic equations, and so on [4.1].

Traditionally road-tire friction was modeled by a static (or steady-state) model.

However, this steady-state point of view was rarely valid since in reality the tires can experience continuous phase change between vehicle's acceleration and braking. This called for the need in developing friction models that would capture the transient behaviour of the road-tire contact forces under time-varying velocity. These dynamic friction models are usually described by ordinary differential equations.

A friction model discussed extensively in the recent literature [4.2-4.7] came to the author's attention. This dynamic friction model, known as the LuGre model, was introduced [4.8] as the result of collaboration between Lund Institute of Technology of Sweden and Laboratoire d'Automatique de Grenoble of France (LuGre). The LuGre friction model has been demonstrated to be an accurate model for capturing most of the steady-state and transient friction behaviours that have been observed experimentally, and to be suitable for the type of in-depth exploration of wheel torque capability [4.2 – 4.8, 4.10].

The LuGre model can be used when considering the cases of either rigid or non-rigid road-tire contact. The rigid contact case treats the wheel as rigid; as a result, the single point contact lump model is formulated [4.4, 4.5, 4.7]. The non-rigid contact renders a distribution model to describe the interaction on the contact patch [4.2 - 4.4, 4.6]. The distributed model would no doubt yield friction behaviors that are closer to reality. However, in keeping with the rigid wheel assumption adopted in Chapter 3, and in aim of simplicity of modeling and numerical simulation, the focus of the present study will be on the point contact LuGre model. The distributed formulation will be recommended for future work.

The advantage of the point contact LuGre model is that the physical parameters entering the model can be selected by a vehicle designer to match the experimental data and be used to describe the condition of road surface. Most importantly, the model is appropriate for normal vehicle motion situation, such as steady-state or transient phases between braking and acceleration; not to mention that the LuGre model has been extensively discussed and applied due to its simplicity in model derivation, ease of model parameter identification, and high accuracy in predicting the frictional behaviors.

## 4.2 The LuGre Dynamic Friction Model.

In Chapter 3 it has been shown that two components of friction force,  $F_{fx}$  and  $F_{fy}$  (see, for example, Figures 3.11 and 3.12, and equations (3.25) and so on), are needed to determine the motions of the vehicle. Thus, a two-dimensional friction model is required for describing the longitudinal and lateral frictions. Such forces are needed in various vehicle dynamics simulation studies, especially vehicle handling studies. The longitudinal and lateral frictions are related to  $N$ , the normal force developed at the contact point between the tire and the road surface:

$$F_{fx} = \mu_x N, \quad F_{fy} = \mu_y N \quad (4.1)$$

where  $\mu_x$  and  $\mu_y$  are the coefficients of friction in the longitudinal and lateral directions, respectively. They are also known as the normalized tire friction. Note that the subscripts  $x$  and  $y$  denote the  $x_{bw}$ - and  $y_{bw}$ -axes (of the wheel base coordinate frame) defined in Section 3.1, see Figure 3.2 in particular. In this chapter the subscript  $n$  ( $n = 1, \dots, 4$ ) has been dropped for simplicity. It is understood that the equations and discussions presented in this chapter are applicable to all four tire-road contact points.

### 4.2.1 The One-Dimensional LuGre Dynamic Friction Model.

The LuGre Model interprets friction as the interaction of microscopic surface asperities

which act as the bristles (rubber elements of the tire) and deflect as the surfaces move with respect to one another (Figure 4.1). The deformation of the bristles gives rise to the friction. The frictional force is given as a function of internal deflected state  $\eta$ , (see [4.2] for example), with  $\eta(t)$  satisfying the differential equation

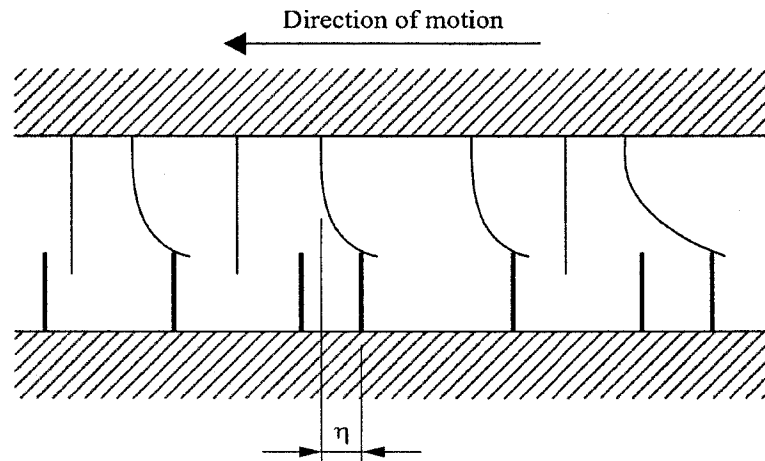


**Figure 4.1** The average internal deflected state  $\eta$  in the direction of motion

$$\frac{d\eta(t)}{dt} = V_r - \frac{\sigma_0 |V_r|}{g(V_r)} \eta(t) \quad (4.2)$$

and the friction is related through

$$F_f = \left[ \sigma_0 \eta(t) + \sigma_1 \frac{d\eta(t)}{dt} + \sigma_2 V_r \right] N \quad (4.3)$$

and the coefficient of friction,  $\mu$ , is

$$\mu = \sigma_0 \eta(t) + \sigma_1 \frac{d\eta(t)}{dt} + \sigma_2 V_r \quad (4.4)$$

In equations (4.2) through (4.4),  $\eta(t)$  is the internal state that describes the deflection of an elementary rubber element,  $V_r$  is the relative velocity between the contact surfaces,  $N$  is the contact normal force exerted on the wheel by the ground,  $\sigma_0$  is the rubber lumped

stiffness,  $\sigma_1$  is the rubber lumped damping,  $\sigma_2$  is the viscous relative damping, and  $g(V_r)$  is a speed dependent sliding function which represents the transitions between the static and kinetic friction coefficients as a function of relative velocity between the contact surface.

$$g(V_r) = \mu_k + (\mu_s - \mu_k)e^{\left(-\frac{|V_r|}{v_s}\right)^\delta} \quad (4.5)$$

where  $\mu_k$  is a parameter representing kinetic friction,  $\mu_s$  a parameter representing static friction, and  $v_s$  the Stribeck velocity [4.9], which refers to the low slip or low relative velocity region, where a decrease in friction force is seen. The constant parameter  $\delta$  in equation (4.5) is known as the Stribeck exponent [4.6]. It is a shape parameter used to capture the steady-state friction or slip characteristic, and typically has values in the range of 0.5 to 2.0 [4.6]. The Stribeck velocity and shape parameter affect the rate of transition between  $\mu_s$  and  $\mu_k$ . Figure 4.2 shows how  $v_s$  and  $\delta$  affect  $g(V_r)$ . Typically, a smaller  $v_s$  or a larger  $\delta$  suggests a quicker transition from  $\mu_s$  to  $\mu_k$ .

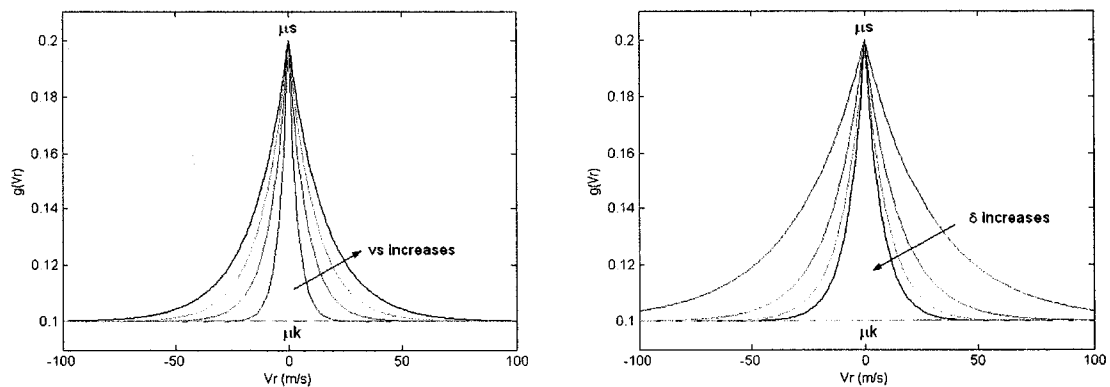


**Figure 4.2** The effect on  $g(V_r)$  due to changes in friction parameters

#### 4.2.2 The Two-Dimensional LuGre Dynamic Friction Model.

The extension of the LuGre friction from the longitudinal one-dimensional (1-D) model to the longitudinal and lateral two-dimensional (2-D) model has been proposed in [4.3, 4.5 - 4.7]. A simple extension would be to assume that the bristle deflections are directionally independent, so as to apply equation (4.2) along the longitudinal ( $x$ ) and lateral ( $y$ ) directions separately. This would result in,

$$\frac{d\eta_{x,y}(t)}{dt} = V_{rx,y} - \frac{\sigma_{0x,y} |V_{rx,y}|}{g_{x,y}(V_{rx,y})} \eta_{x,y} \quad (4.6)$$

Equation (4.6) should be looked at as two independent sub-models where  $g_{x,y}(V_{rx,y})$

were two independent friction functions with two different sets of parameters; that is,

$$g_x(V_{rx}) = \mu_{kx} + (\mu_{sx} - \mu_{kx}) e^{\left(-\left|\frac{V_{rx}}{v_{sx}}\right|\right)^{\delta_x}} \quad \text{and} \quad g_y(V_{ry}) = \mu_{ky} + (\mu_{sy} - \mu_{ky}) e^{\left(-\left|\frac{V_{ry}}{v_{sy}}\right|\right)^{\delta_y}}.$$

Physically this would mean that two bristles would deflect independently in two directions. In reality there is only a single bristle at the contact point; therefore there exists a single, unique, friction [4.6]. A different expression for  $g_{x,y}(V_{rx,y})$  was given in [4.6],

$$g_{x,y}(V_{rx,y}) = \left| \frac{V_{rx,y}}{V_r} \right| g(V_r) \quad (4.7)$$

Equation (4.7) yields positive longitudinal and lateral components of the road-tire sliding friction force  $g(V_r)$  (see Figure 4.2). Substituting equation (4.7) into equation (4.6) yields the deflection equations for the combined longitudinal and lateral motion. Unlike

in equation (4.6), the two sub-models are now coupled with the sliding friction function and the relative speed. That is,

$$\frac{d\eta_{x,y}(t)}{dt} = V_{rx,y} - \frac{\sigma_{0x,y} |V_r|}{g(V_r)} \eta_{x,y} \quad (4.8)$$

where the longitudinal and lateral frictional coefficients are, from equation (4.3),

$$\begin{aligned} \mu_{x,y} &= \sigma_{0x,y} \eta_{x,y}(t) + \sigma_{1x,y} \frac{d\eta_{x,y}(t)}{dt} + \sigma_{2x,y} V_{rx,y} \\ &= \sigma_{0x,y} \eta_{x,y}(t) + \sigma_{1x,y} \left( V_{rx,y} - \frac{\sigma_{0x,y} |V_r|}{g(V_r)} \eta_{x,y} \right) + \sigma_{2x,y} V_{rx,y} \end{aligned} \quad (4.9)$$

where  $\sigma_{0x}, \sigma_{0y}$  are the bristle stiffness constants;  $\sigma_{1x}, \sigma_{1y}$  are the bristle damping coefficient constants; and  $\sigma_{2x}, \sigma_{2y}$  are the bristle viscous damping coefficient associated with the  $x$  and  $y$  directions, respectively. These parameters can be identified from experimental data if possible, or pre-assigned as constants for simulation purposes.

### 4.3 Steady-State Characteristics.

In most literature it is common that the steady-state friction characteristics are expressed as a function of slip coefficients. In 2-D steady-state friction model, the lateral friction is expressed as a function of slip angles, and the longitudinal friction as a function of slip ratio. The steady-state analysis of friction models is widely employed in the study of road-tire interaction.

The steady-state characteristics of the deflected rubber element are obtained by setting  $\frac{d\eta_{x,y}(t)}{dt}$  to zero and by solving equation (4.8) to obtain [4.10]

$$\eta_{(ss)x,y} = \frac{g(V_r)V_{rx,y}}{\sigma_{0x,y}|V_r|} \quad (4.10)$$

Substituting equation (4.10) into (4.9), the steady-state frictional coefficients are found to be [4.10]

$$\mu_{(ss)x,y} = \left[ \frac{g(V_r)}{|V_r|} + \sigma_{2x,y} \right] V_{rx,y} \quad (4.11)$$

This steady-state solution can be used to calibrate and identify the model parameters by fitting this model to experimental data or to the “Magic formula” which will be introduced in the next section.

#### 4.3.1 The “Magic Formula”.

One of the most well-known models for static frictional coefficient is the Pacejka’s model [4.11], also known as the “magic formula”. This model has been shown to suitably match experimental results and accurately describe the tire steady-state curves. It has been the benchmark for validating the steady-state conditions for dynamic tire friction models. In Reference [4.11] Pacejka presented the following formula for describing the friction function.

$$\mu = D \sin(C \arctan(BM - E(BM - \arctan(BM)))) \quad (4.12)$$

where  $M$  is either the longitudinal slip ratio  $s$ , or slip angle  $\beta$ . The parameters  $B$ ,  $C$ ,  $D$  and  $E$  can be identified through curve-fitting with experiment data. Different sets of parameters can then be used to generate plots of the longitudinal friction coefficient,  $\mu_x(s)$ , as a function of slip ratio,  $s$ , and plots of the lateral friction coefficient,  $\mu_y(\beta)$ , as a function of slip angle,  $\beta$ . Thus, to observe the relation of steady-state friction characteristics between the LuGre and the “magic formula” and to identify the parameters, it is convenient to express the LuGre friction model in terms of the slip coefficients.

#### 4.3.2 Definition of Slip.

In vehicle dynamics, slip is the relative motion between a tire and the road surface it is moving on. This slip can be generated either by the tire's rotational speed ( $\omega$ ) being greater or less than the free-rolling speed ( $V_x$ ). It is usually described as a ratio or percentage slip ( $s$ ), or by the tire's plane of rotation being at an angle to its direction of motion, which is also known as the slip angle ( $\beta$ ). Examining equation (4.2), one may realize that when the vehicle travels at a constant speed with no slip and no steer at the contact interfaces between the tires and the road, that is, where  $V_r = 0$ , the right hand side (RHS) of equation (4.2) becomes zero, or the dynamic deflection of the bristle,  $\eta(t)$ , is constant; since the bristle has no initial deflection, the dynamic deflection is then  $\eta(t) = 0$ .

From equation (4.3) it is seen that the tire friction forces described by the LuGre friction model is zero, or  $F_f=0$ .

The relative velocity is defined in the wheel plane  $x$ - $y$  where  $O$  is the contact point (Figure 4.3) with the following components

$$\begin{aligned} V_{rx} &= V \cos(\beta) + r\omega = V_x + r\omega \\ V_{ry} &= V \sin(\beta) \end{aligned} \quad (4.13)$$

so that

$$V_r = \sqrt{V_{rx}^2 + V_{ry}^2} \quad (4.14)$$

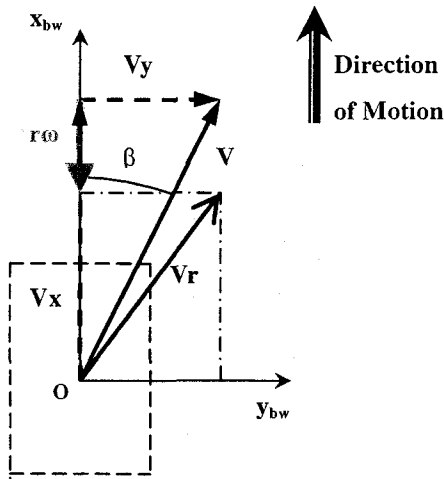


**Figure 4.3a Slip for braking**

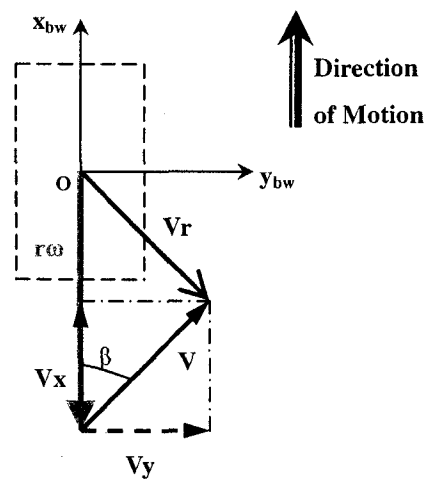


**Figure 4.3b Slip for acceleration**

In equation (4.13),  $V = \sqrt{V_x^2 + V_y^2}$  is the wheel hub translational speed along the direction of travel with components  $[V_x, V_y]$ ;  $\omega$  is the wheel hub rotational speed;  $\beta$  is the slip angle or the angle between the direction of travel and the longitudinal axis of the wheel coordinate. Note that for the wheel-center coordinate frame defined in Chapter 3, a

wheel coordinate. Note that for the wheel-center coordinate frame defined in Chapter 3, a negative wheel angular velocity  $\omega$  implies a forward motion.

The longitudinal slip  $s$ , and the lateral slip  $q$ , both need to be defined under two separate cases, braking and acceleration. For the braking case (Figure 4.3a), the slips (identified by a subscript  $b$ ) are given by

$$\begin{aligned} s_b &= \frac{V \cos(\beta) + r\omega}{V \cos(\beta)} = \frac{V_{r_x}}{V_x} & V_x > -r\omega \text{ and } V_x \neq 0 \\ q_b &= \frac{V_{r_y}}{V_x} = \tan(\beta) \end{aligned} \quad (4.15)$$

For the case of acceleration (Figure 4.3b), the slips (identified by a subscript  $a$ ) are

$$\begin{aligned} s_a &= \frac{V \cos(\beta) + r\omega}{r\omega} = \frac{V_{r_x}}{r\omega} & r\omega > -V_x \text{ and } \omega \neq 0 \\ q_a &= \frac{V_{r_y}}{r\omega} = (1 - s_a) \tan(\beta) \end{aligned} \quad (4.16)$$

The longitudinal slip is always positive within the interval  $[0, 1]$ . When  $s = 0$  there is no sliding, whereas  $s = 1$  indicates full sliding or skidding. The lateral slip is a function of slip angle and directionally dependent.

With the slip rates now defined,  $\mu_{SSx}(s)$  and  $\mu_{SSy}(\beta)$  of equation (4.11) can be determined. For braking, the sliding function  $g(V_r)$  in equation (4.5) becomes

$$g(V_r) = \mu_k + (\mu_s - \mu_k) e^{-\left(\frac{V_x \sqrt{q_b(\beta)^2 + s_b^2}}{v_s}\right)^\delta} \quad (4.17)$$

and for acceleration

$$g(V_r) = \mu_k + (\mu_s - \mu_k) e^{-\left(\frac{r\omega \sqrt{q_a(\beta)^2 + s_a^2}}{v_s}\right)^\delta} \quad (4.18)$$

Finally, the frictional parameters are, from equation (4.11)

$$\mu_{(ss)x} = \left[ \frac{g(V_r)}{\sqrt{q_b(\beta)^2 + S_b^2}} + \sigma_{2x}V_x \right] S_b, \quad \mu_{(ss)y} = \left[ \frac{g(V_r)}{\sqrt{q_b(\beta)^2 + S_b^2}} + \sigma_{2y}V_x \right] q_b(\beta) \quad (4.19)$$

for steady-state braking at some constant velocity,  $V$ , and

$$\mu_{(ss)x} = \left[ \frac{g(V_r)}{\sqrt{q_a(\beta)^2 + S_a^2}} + \sigma_{2x}r\omega \right] S_a, \quad \mu_{(ss)y} = \left[ \frac{g(V_r)}{\sqrt{q_a(\beta)^2 + S_a^2}} + \sigma_{2y}r\omega \right] q_a(\beta) \quad (4.20)$$

for steady-state driving at some constant  $\omega$ . It should be pointed out that the steady-state behavior of the LuGre dynamic road-tire friction model can only be obtained for a specified constant velocity  $V$  or constant angular velocity  $\omega$ , and may be validated with the Pacejka's "magic formula".

#### 4.4 Validation of Steady-State Behavior with the Magic Formula.

To validate the steady-state behavior of the LuGre model presented above, experimental data presented in [4.2] are used as the basis of comparison. Reference [4.2] listed two sets of parameters, used in conjunction with the "magic formula", for vehicle braking and cornering. These two sets of parameters are given in Table 4.1, along with parametric values used in the present study. It is seen that parameter  $B$  has a value of 18.0 instead of the 0.178 listed in [4.2]. The 18.0 value is found after a number of trials-and-error in the present study. This is necessary in order to best-fit experimental data of [4.2]. The source of the discrepancy is not fully understood. One possible cause may be the lack of units in

[4.2]. The resulting tire static curves, plots of friction force versus slip, are shown in Figure 4.4.

As to the LuGre model, model parameters are identified by best-fitting the steady-state behavior, equation (4.19), to the “magic formula” plots. In Figure 4.4, the plots are those of forces  $F_x(s)$  and  $F_y(\delta)$ . They are obtained by multiplying equation (4.19) by a normal force,  $N = 2000\text{N}$ , which was used in [4.2]. The LuGre model parameters are identified after a number of trials-and-error in the present study. They are listed in Table 4.2 as well. Note that  $\sigma_{2x}$  and  $\sigma_{2y}$  are set to zero, which implies an dry frictional contact assumption. It is also noted that the  $\mu_s$  has a value greater than unity. This is because  $\mu_s$  and  $\mu_k$  are simply frictional parameters used in conjunction with the LuGre friction model. They are not to be interpreted as the coefficient of friction used with the well-known theory of dry (Coulomb) friction. In Figure 4.4,  $F_x$  is plotted as a function of  $s$  for braking by setting  $\beta = 2.0^\circ$  and  $V = 60 \text{ km/h}$ . On the other hand, the plot of  $F_y$  versus  $\beta$  is obtained with the setting of  $s = 0.05$  and  $V = 70 \text{ km/h}$ . The very close match between the “magic formula” and the LuGre model as seen in Figure 4.4 shows that by selecting appropriate parameters, the LuGre model provides an excellent representation for the steady-state behavior of the road-tire friction.

**Table 4.1 Magic Formula Parameters**

Parameters		$B$	$C$	$D$	$E$
Ref. [4.2]	$F_x$ (braking)	0.178	1.55	2193	0.432
	$F_y$ (cornering)	0.244	1.5	1936	-0.132
Present study	$F_x$ (braking)	18.0	1.55	2193	0.432
	$F_y$ (cornering)	0.244	1.5	1936	-0.132

**Table 4.2 LuGre Model Parameters**

Parameters		$\mu_k$	$\mu_s$	$\nu_s$	$\delta$	$\sigma_{2x}$	$\sigma_{2y}$
Present study	$F_x$ (braking)	0.72	1.35	5.5	0.75	0.0	0.0
	$F_y$ (cornering)	0.65	1.35	5.5	0.75	0.0	0.0

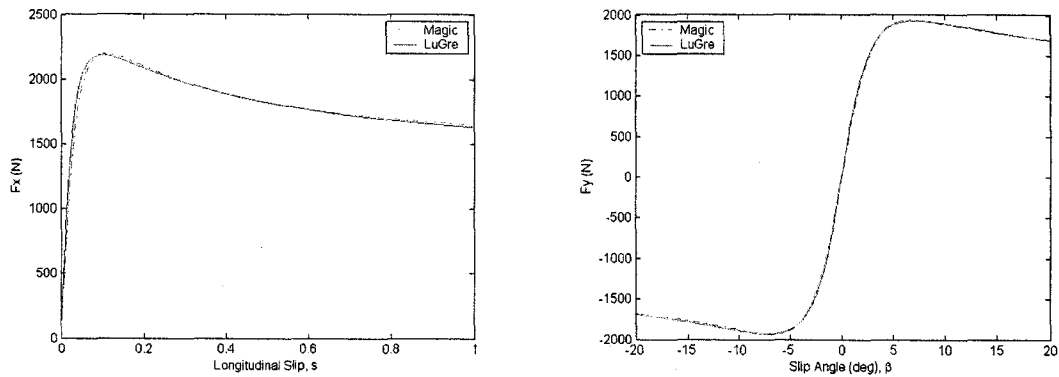


**Figure 4.4 Steady-state friction forces  $F_x(s)$  and  $F_y(\beta)$**

#### 4.4 Incorporating the LuGre Friction Model.

The dynamic LuGre model, in the form of equation (4.9), is derived under the assumption that the wheels travel along the longitudinal, or  $x$ -direction only. In order to incorporate the steering of the wheels, it is then considered that a wheel is rotated from the longitudinal direction by an angle of, say,  $\theta$  (see Figure 4.5b). Since “The changes in the

bristle deflection are measured as a result of rotation of the measurement frame rather than as a result of changes in the actual displacement” [4.10], only the transferring from the measurement frame  $x$ - $y$ - $z$  to the global coordinate frame  $X$ - $Y$ - $Z$  is required. It should be noted that in Figure 4.5a the measurement frame  $x$ - $y$ - $z$  initially coincides with the  $X$ - $Y$ - $Z$  global coordinate frame. As shown in Figure 4.5, this measurement frame is in fact the wheel base coordinate frame defined in Chapter 3. The wheel rotation is taken as the steering input  $\theta(t)$  from the driver. Note that the deflection of a bristle,  $\eta$ , always makes an angle of  $\lambda$  with respect to the global coordinate  $X$ . Expressing the  $\eta$  vector with respect to the wheel base coordinate frame, one has,

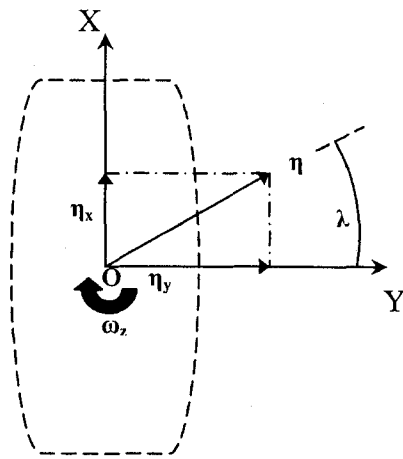


**Figure 4.5a Bristle deformation before rotation**

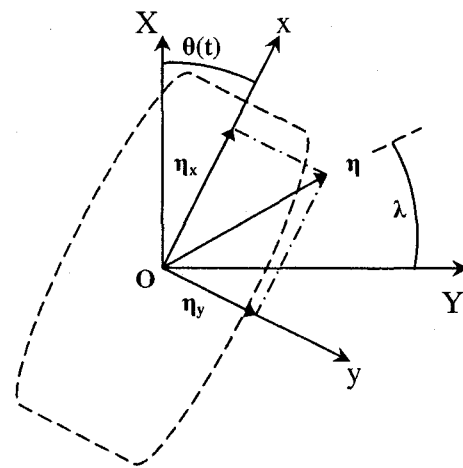


**Figure 4.5b Bristle deformation after rotation**

$$\eta = \eta_x \vec{i}_{bw} + \eta_y \vec{j}_{bw} + \eta_z \vec{k}_{bw} \quad (4.21)$$

The bristle deflection component  $\eta_z$  may be neglected because it is assumed to be small compared to the longitudinal and lateral deflections. Equation (4.21) becomes

$$\boldsymbol{\eta} = \eta_x \vec{i}_{bw} + \eta_y \vec{j}_{bw} \quad (4.22)$$

Next, the time derivative of the bristle deformation expressed in the wheel base coordinate frame can be written as

$$\dot{\boldsymbol{\eta}} = \dot{\eta}_x \vec{i}_{bw} + \dot{\eta}_y \vec{j}_{bw} + \eta_x \dot{\vec{i}}_{bw} + \eta_y \dot{\vec{j}}_{bw} \quad (4.23)$$

Since the wheel base coordinate frame rotates only about  $z_{bw}$  as the wheel steers (see Figure 3.2), one has

$$\dot{\vec{i}}_{bw} = \omega_{zb} \vec{j}_{bw}, \quad \dot{\vec{j}}_{bw} = -\omega_{zb} \vec{i}_{bw} \quad (4.24)$$

where  $\omega_{zb}$  is the rotational velocity of the wheel about  $z_{bw}$ . Substituting equation (4.24) into equation (4.23) yields

$$\dot{\boldsymbol{\eta}} = (\dot{\eta}_x - \omega_{zb} \eta_y) \vec{i}_{bw} + (\dot{\eta}_y + \omega_{zb} \eta_x) \vec{j}_{bw} \quad (4.25)$$

where the coupling effect due to combined translational and rotational motion of the wheel is clearly reflected by terms such as  $\omega_{zb} \eta_x$  and  $\omega_{zb} \eta_y$ . Next, equation (4.8) is revised taking into account (4.25) so that

$$\begin{aligned} \frac{d\eta_x(t)}{dt} &= V_{rx} - \frac{\sigma_{0x} |V_r|}{g(V_r)} \eta_x + \omega_{zb} \eta_y \\ \frac{d\eta_y(t)}{dt} &= V_{ry} - \frac{\sigma_{0y} |V_r|}{g(V_r)} \eta_y - \omega_{zb} \eta_x \end{aligned} \quad (4.26)$$

Finally, the dynamic tire frictional coefficients with respect to the wheel base coordinate frame are,

$$\begin{aligned}
 \mu_x &= \sigma_{0x}\eta_x(t) + \sigma_{1x}\frac{d\eta_x(t)}{dt} + \sigma_{2x}V_{rx} \\
 &= \sigma_{0x}\eta_x(t) + \sigma_{1x}\left(V_{rx} - \frac{\sigma_{0x}|V_r|}{g(V_r)}\eta_x + \omega_{zb}\eta_y\right) + \sigma_{2x}V_{rx} \\
 \mu_y &= \sigma_{0y}\eta_y(t) + \sigma_{1y}\frac{d\eta_y(t)}{dt} + \sigma_{2y}V_{ry} \\
 &= \sigma_{0y}\eta_y(t) + \sigma_{1y}\left(V_{ry} - \frac{\sigma_{0y}|V_r|}{g(V_r)}\eta_y - \omega_{zb}\eta_x\right) + \sigma_{2y}V_{ry}
 \end{aligned}
 \tag{4.27}$$

The final task is to extend the friction model, equation (4.27), from a single wheel to the full-car model. Since the wheels are not modeled as separate systems from the vehicle body, the friction model needs to be defined with respect to the vehicle body frame as was done in Chapter 3.

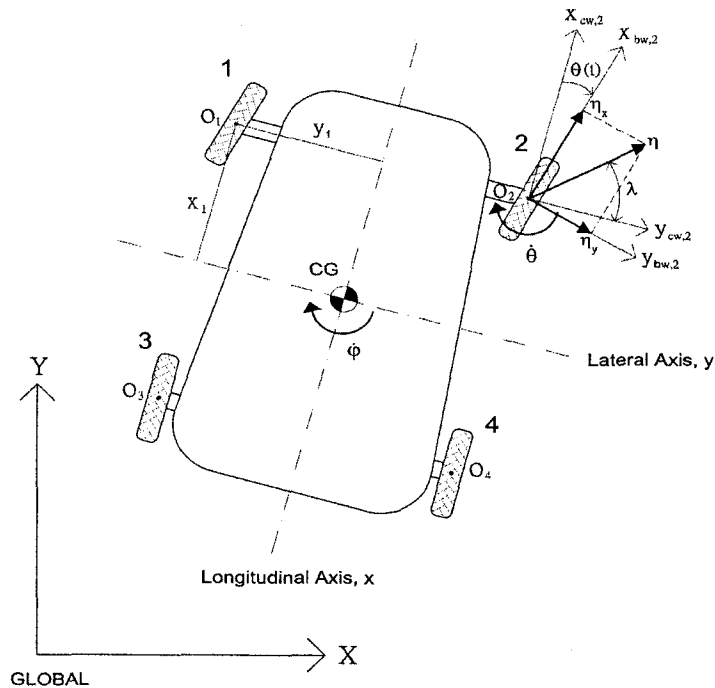


**Figure 4.6 Total bristle deflection with respect to the global frame**

As illustrated in Figure 4.6, the total rate of rotation of the wheel base frame with respect to the global frame is the sum of the yaw rate of the vehicle body,  $\dot{\varphi}$ , and the steering rate  $\dot{\theta}(t)$ . For a full-car model, the  $n$ -th ( $n = 1, \dots, 4$ ) bristle dynamic equation and tire frictional parameters are obtained from equations (4.26) and (4.27)

$$\begin{aligned}\dot{\eta}_{x,n}(t) &= V_{rx,n} - \frac{\sigma_{0x}|V_{r,n}|}{g(V_{r,n})}\eta_{x,n} + (\dot{\varphi} + \dot{\theta}_n(t))\eta_{y,n} \\ \dot{\eta}_{y,n}(t) &= V_{ry,n} - \frac{\sigma_{0y}|V_{r,n}|}{g(V_{r,n})}\eta_{y,n} - (\dot{\varphi} + \dot{\theta}_n(t))\eta_{x,n}\end{aligned}\quad (4.28)$$

and,

$$\begin{aligned}\mu_{x,n} &= \sigma_{0x}\eta_{x,n}(t) + \sigma_{1x}\dot{\eta}_{x,n}(t) + \sigma_{2x}V_{rx,n} \\ &= \sigma_{0x}\eta_{x,n}(t) + \sigma_{1x}\left(V_{rx,n} - \frac{\sigma_{0x}|V_{r,n}|}{g(V_{r,n})}\eta_{x,n} + (\dot{\varphi} + \dot{\theta}_n(t))\eta_{y,n}\right) + \sigma_{2x}V_{rx,n} \\ \mu_{y,n} &= \sigma_{0y}\eta_{y,n}(t) + \sigma_{1y}\dot{\eta}_{y,n}(t) + \sigma_{2y}V_{ry,n} \\ &= \sigma_{0y}\eta_{y,n}(t) + \sigma_{1y}\left(V_{ry,n} - \frac{\sigma_{0y}|V_{r,n}|}{g(V_{r,n})}\eta_{y,n} - (\dot{\varphi} + \dot{\theta}_n(t))\eta_{x,n}\right) + \sigma_{2y}V_{ry,n}\end{aligned}\quad (4.29)$$

where the relative velocity of the  $n$ -th wheel,  $V_{r,n} = [V_{rx,n}, V_{ry,n}]$ , is defined as the velocity of the contact point of wheel  $n$  with respect to the ground. Since the velocity of the ground is zero, the total velocity of the contact point becomes simply the relative velocity,

$$V_{r,n} = V_{translation,n} + V_{rotation,n}\quad (4.30)$$

where the translational velocity of contact point equals that of the wheel center, or  $V_{cw,n}$ , as defined by equation (3.11). That is

$$V_{translation,n} = V_{cw,n}\quad (4.31)$$

The second term,  $V_{rotation,n}$ , represents the velocity of the contact point rotating about the  $y_{cw,n}$ -axis of the  $n$ -th wheel (see Figure 3.12). If the wheel is spinning at  $\omega_n$ ,

$$V_{rotation,n} = r\omega_n \vec{i}_{bw,n} \quad (4.32)$$

where  $r$  is the wheel radius which is assumed to be the same for all four wheels.

Substituting equations (3.11) and (4.32) gives

$$V_{r,n} = [\dot{x} - \dot{\varphi}y_n] \vec{i} + [\dot{y} + \dot{\varphi}x_n] \vec{j} + \dot{z}_n \vec{k} + r\omega_n \vec{i}_{bw,n} \quad (4.33)$$

In the above equation,  $\dot{z}_n \vec{k}$  may be neglected just as the  $\eta_z$  component of the bristle deflection was neglected earlier in equation (4.22). Furthermore, unit vectors  $\vec{i}, \vec{j}$

and  $\vec{i}_{bw,n}, \vec{j}_{bw,n}$  are related via equation (3.2). Noting that  $\vec{i} = \vec{i}_{cw,n}, \vec{j} = \vec{j}_{cw,n}$ , one then has,

$$V_{r,n} = [(\dot{x} - \dot{\varphi}y_n) \cos \theta_n + (\dot{y} + \dot{\varphi}x_n) \sin \theta_n + \omega_n r] \vec{i}_{bw,n} + [(\dot{y} + \dot{\varphi}x_n) \cos \theta_n - (\dot{x} - \dot{\varphi}y_n) \sin \theta_n] \vec{j}_{bw,n} \quad (4.34)$$

#### 4.6 Concluding Remarks.

The dynamic LuGre friction model, when applied to the full-car model, consists of equation (4.29) where the relative velocities are determined by equation (4.34). The  $x$ - and  $y$ -components of the frictional force, which are needed for the full-car model developed in Chapter 3, are

$$\begin{aligned}
F_{fx,n} &= \mu_{x,n} N_n \\
&= \left[ \sigma_{0x} \eta_{x,n}(t) + \sigma_{1x} \left( V_{rx,n} - \frac{\sigma_{0x} |V_{r,n}|}{g(V_{r,n})} \eta_{x,n} + (\dot{\varphi} + \dot{\theta}_n(t)) \eta_{y,n} \right) + \sigma_{2x} V_{rx,n} \right] N_n \\
F_{fy,n} &= \mu_{y,n} N_n \\
&= \left[ \sigma_{0y} \eta_{y,n}(t) + \sigma_{1y} \left( V_{ry,n} - \frac{\sigma_{0y} |V_{r,n}|}{g(V_{r,n})} \eta_{y,n} - (\dot{\varphi} + \dot{\theta}_n(t)) \eta_{x,n} \right) + \sigma_{2y} V_{ry,n} \right] N_n
\end{aligned} \tag{4.35}$$

where the relative velocities are again determined by equation (4.34). In determining frictional force components, steering angles  $\theta_n(t)$  ( $n = 1, \dots, 4$ ) and their time derivatives  $\dot{\theta}_n(t)$  ( $n = 1, \dots, 4$ ) are considered inputs to the system rather than state variables. The steering angles and their respective derivatives are independent of each other when considering independent suspensions. Specifically – to paraphrase the suggestion by [4.10] – the rear steering angles are fixed at zero steers, the front steering angles are constrained according to Figure 4.7, “so that no wheel slip is induced by the steering geometry, allowing for the possibility of zero relative velocity solutions at all four wheels.”

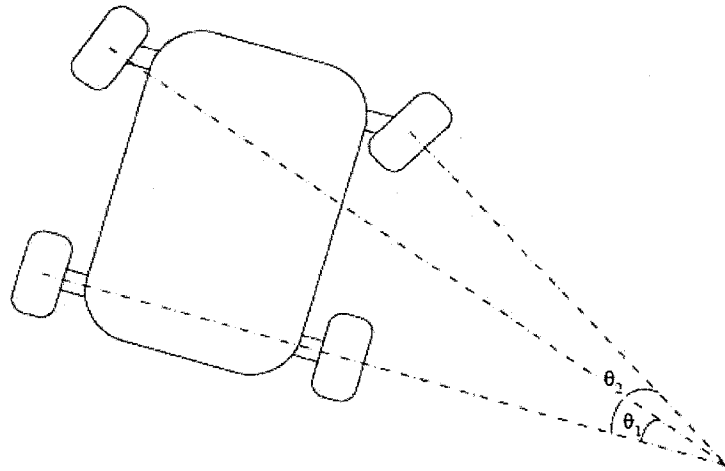


**Figure 4.7 Vehicle steering geometry definition [4.10]**

## CHAPTER 5

### NUMERICAL STUDIES OF VEHICLE DYNAMICS

In Chapters 3 and 4, all the necessary components for a vehicle dynamic model have been developed. Next, the model is to be put through different cases to verify the model's capability in representing various vehicle dynamic situations, the assumptions behind different simplifications, and the model's accuracy. The selected cases are from recent publications in the area of vehicle dynamic and control, including issues of ride comfort and handling.

The objective is to utilize the present vehicle model to reproduce the results as presented by other researchers. Identical conditions and physical parameters are identified and implemented where applicable. Because of assumptions made in the referenced publications, modifications of the presently developed vehicle model are necessary. The chapter emphasizes on comparing the models, and identifying the differences or similarities among them, so as to demonstrate the range of applicability of the present model.

## 5.1 A Planar Model of a Three-Wheeled Vehicle.

### 5.1.1 A Half-Car Model by Gawade et.al.

An in-plane seven degrees-of-freedom (DOF) mathematical model of a three-wheel vehicle (TWV) was presented in [5.1] to study the effect of road bumps on occupant injury. The system equations may be used to calculate the forces and positions of interacting components while the TWV was passing over bumps of different profiles, and to examine the lift-off phenomenon (which is a measurement of vehicle stability) and the ride comfort of the TWV. Wheel lift-off occurs when the normal reactions exerted by the road onto a wheel goes to zero, causing the tire to lose contact with the ground. Ride comfort, on the other hand, can be measured by the time history of the maximum upward acceleration and/or the frequency spectrum of the acceleration.

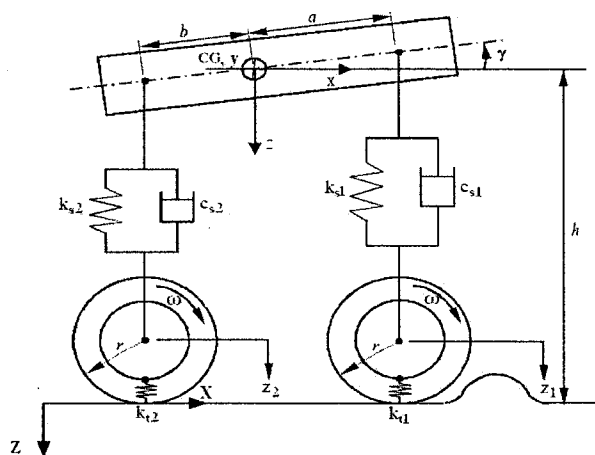


**Figure 5.1 The planar TWV model**

The planar TWV model shown in Figure 5.1 (where symbols have been changed from those of [5.3] for the sake of consistency) was assumed to travel over the bump with a

constant longitudinal speed and without steering. The vehicle body, front wheel and a

lumped rear wheel were considered rigid, and were connected with linear suspensions.

Though the wheels themselves were considered rigid, tire stiffness was incorporated into the model. The seven DOFs considered were the longitudinal motion, bounce and pitch for the vehicle body; and the bounce and spin motions for each of the wheels. Vehicle body's lateral motion, roll and yaw were not considered since it was a half-car planar model. Furthermore, the no-slip assumption was made, such that  $\dot{\omega} = -\ddot{x}/r$ , and the road-tire friction forces were [5.1],

$$F_{fx,n} = \frac{I_{spin,n}\dot{\omega}_n - T_n}{r} = -\frac{I_{spin,n}\ddot{x}}{r^2} - \frac{T_n}{r} \quad n = 1,2 \quad (5.1)$$

### 5.1.2 The Present Model.

Introducing some simplification into the general model presented in sections 3.4.6 - 3.4.8 by setting  $\ddot{y} = \dot{y} = y = \ddot{\phi} = \dot{\phi} = \phi = \ddot{\varphi} = \dot{\varphi} = \varphi = F_{fy,n} = 0$ , the equations of motion for the bounce and spin motions of the wheels are then given by

$$\begin{aligned} m_n \ddot{z}_n &= k_{sn}(z - x_n \gamma - z_n) + c_{sn}(\dot{z} - x_n \dot{\gamma} - \dot{z}_n) - k_{tn}(z_n - z_{sn}) \\ I_{spin,n} \dot{\omega}_n &= -r F_{fx,n} - T_n \end{aligned} \quad (5.2)$$

Equation of motion for the bounce motion of the vehicle body is given by

$$M_b \ddot{z} = -\sum [k_{sn}(z - x_n \gamma - z_n) + c_{sn}(\dot{z} - x_n \dot{\gamma} - \dot{z}_n)] \quad (5.3)$$

and for the longitudinal and pitch motions of the vehicle body, one has

$$M_{tot} \ddot{x} = -\sum (F_{fx,n}) \quad (5.4)$$

and

$$I_{y, cg} \ddot{\gamma} = -\sum (z_{w,n} m_n) - \sum (F_{fx,n} z_{w,n}) + \sum [k_{sn} (z - x_n \gamma - z_n) x_n] + \sum [c_{sn} (\dot{z} - x_n \dot{\gamma} - \dot{z}_n) x_n] \quad (5.5)$$

In equations (5.2) through (5.5),  $m_1$  is the mass of the front wheel, and  $m_2$  is the combined mass of the two rear wheels. Accordingly,  $I_{span,1}$  is the mass moment of inertia of the front wheels, and  $I_{span,2}$  is the combined mass moment of inertia of the two rear wheels. The wheel index  $n$  runs over 1 and 2, or  $\sum = \sum_{n=1}^2$ , and  $M_{tot} = M_b + m_1 + m_2$ . These equations of motion are proven identical to those proposed in [5.1]. As to the longitudinal frictional force,  $F_{fx,n}$ , the LuGre friction model may be implemented to better capture the behavior of the tires when in contact with the road. The parameters of the LuGre friction model used for the present study are taken from [4.7] and listed in Table 5.1.

**Table 5.1 Parameters for LuGre Friction Model**

Parameters	Values	Units
$\mu_k$	0.57	-
$\mu_s$	1.41	-
$v_s$	2.66	m/s
$\delta$	0.5	-
$\sigma_{0x}$	267.00	m <sup>-1</sup>
$\sigma_{1x}$	1.33	s/m
$\sigma_{2x}$	0.0001	s/m

### 5.1.3 Results and Discussions.

The differential equations of motion for both models are then solved using MatLab®. For comparison, one of the scenarios investigated in [5.1] has been chosen where the vehicle travels over a road bump modeled as a half-sine wave with amplitude of 0.1 m and transverse distance of 2.0 m (Figure 5.2). The bump is located 0.5m ahead of the center of front wheel along the longitudinal axis. The vehicle is set to travel at its wheel lift-off speed of 5.11 m/s which was determined by [5.1]. Other parameters are given in Table 5.2. Wheel torques  $T_1$  and  $T_2$  are zero.

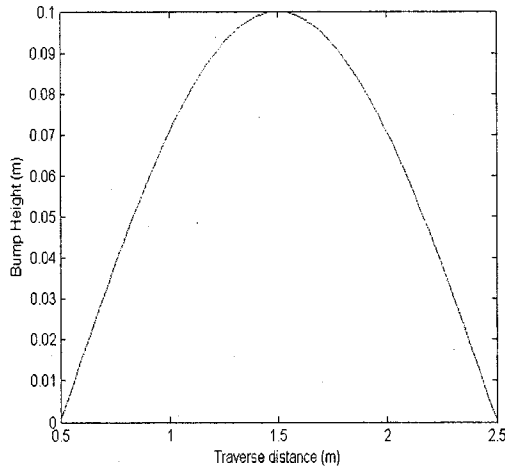


**Figure 5.2 Half-sine wave road profile**

**Table 5.2 Parameters for the TWV**

Parameter	Value	Unit
$M_b$	504	kg
$m_1$	8.5	kg
$m_2$	18.0	kg
$k_{s1}$	32736	N/m
$k_{s2}$	105414	N/m
$k_{t1}$	238260	N/m
$k_{t2}$	500980	N/m
$c_{s1}$	3250	N.s/m
$c_{s2}$	6470	N.s/m
$x_1$	1.437	m
$x_2$	-0.563	m
$h$	0.530	m
$r$	0.210	m
$I_{y,cg}$	170.000	kg.m <sup>2</sup>
$I_{spin,1}$	0.110	kg.m <sup>2</sup>
$I_{spin,2}$	0.220	kg.m <sup>2</sup>

The normal reaction forces, vertical acceleration of the vehicle body and its frequency spectrum from both models are shown in Figures 5.3 and 5.4. It is clearly seen that both models yield identical time and frequency responses. Wheel lift-off is seen when the rear wheels are positioned at  $x = 3.65$  m (Figure 5.3b) and the peak reaction is observed at rear wheels at  $x = 4.66$  m.

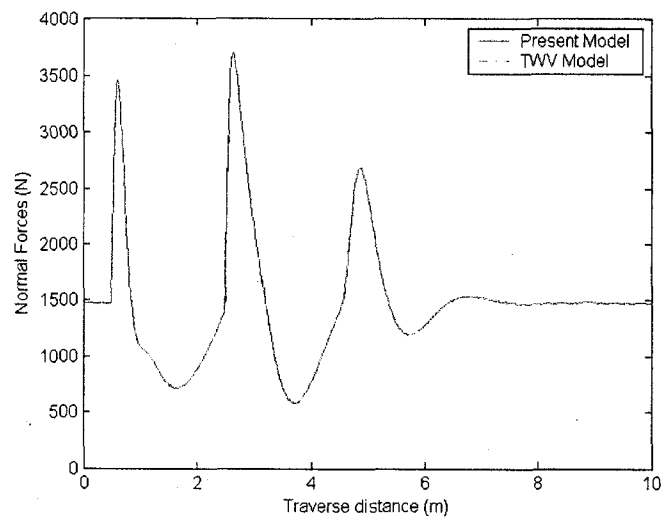


**Figure 5.3a** Normal reaction at front wheel

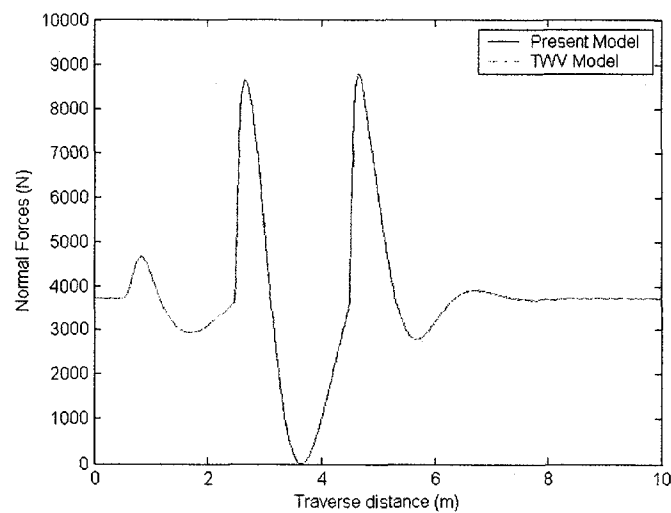


**Figure 5.3b** Normal reaction at rear wheels

As to ride comfort, results of the time history and the frequency spectrum of the vertical acceleration (Figure 5.4) show the same level of vibration with dominant frequency at about 2 Hz with an amplitude of  $5.25 \text{ m/s}^2$ .

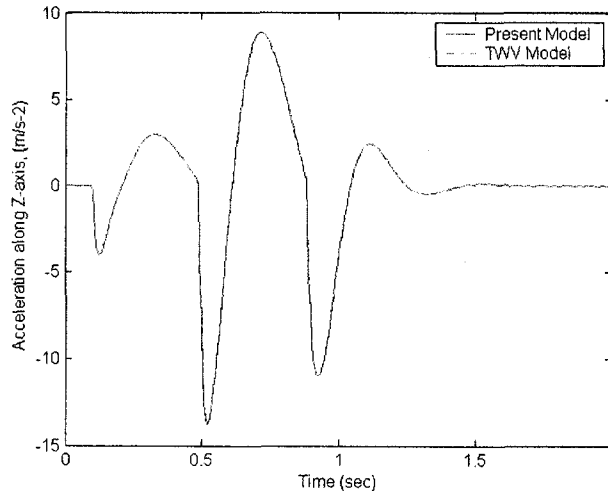


**Figure 5.4a Vertical acceleration of the vehicle body – Time history**

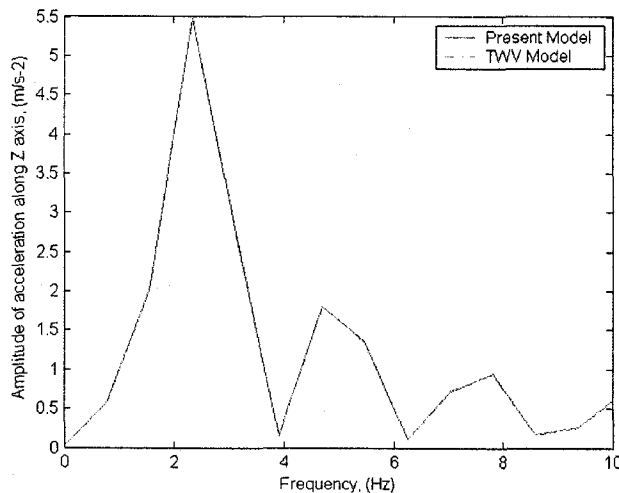
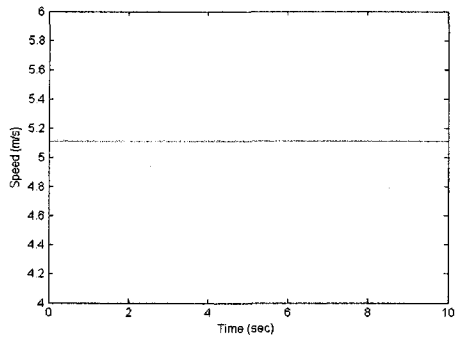


**Figure 5.4b Vertical acceleration of the vehicle body – Frequency spectrum**

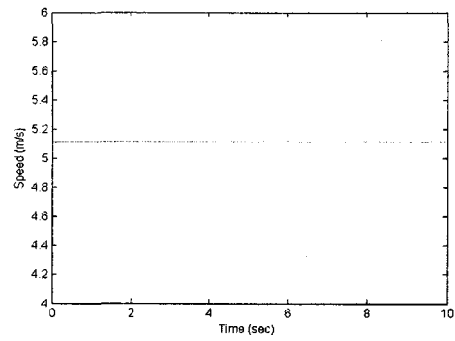
To make sure that the no slip condition is true, longitudinal speed of the vehicle body and the spinning velocity of the wheels are plotted (Figure 5.5), which verifies that

the relation  $\omega = -\dot{x}/r$  is maintained. Frictional forces are shown in Figure 5.6. They are constantly zero.

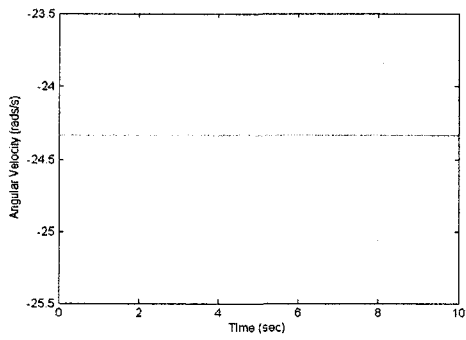
Recalling from Chapter 4 (see Sections 4.2.1 and 4.3.2, in particular) that when the vehicle travels at a constant speed with no slip and no steer, the tire friction forces will be constant and equal to zero. The wheels will experience the pure rolling motions. In the LuGre friction model, the frictional force is given as a function of the bristle deflected behavior and is depended on the rate of change in relative speed or slip at the contact surface between the tire and the road. Thus, with no-slip at the contact interfaces and the expression given by equation (5.1), one may realize that a non-zero tire friction force appears only when the vehicle is imposed by external forces or wheel torque for acceleration or deceleration. The constant zero friction forces represent the dynamic equilibrium and the steady-state motion of vehicle and wheels, which is what the present planar TWV model is expected to simulate. Note that the constant longitudinal speed, the zero steer and the absence of wheel torques all point to the vehicle moving along a straight path, and having zero acceleration. Since there are no applied wheel torques, friction forces at the tire-road contact points will have to be zero for Newton's second law to be satisfied. The friction forces may be expressed as in equation (5.1) or by the LuGre friction model, with the latter being chosen for the present model.



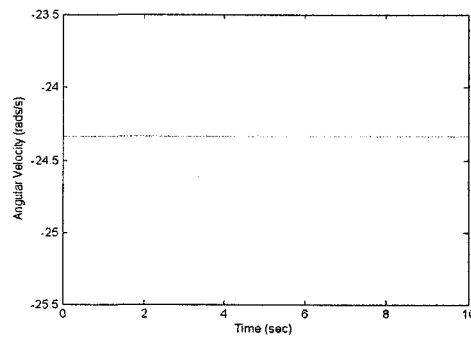
**a. Longitudinal velocity, Ref. [5.1]**



**b. Longitudinal velocity, present model**



**c. Spinning velocity, Ref. [5.1]**



**d. Spinning velocity, present model**

**Figure 5.5 Comparisons of the present model and Ref. [5.1]**

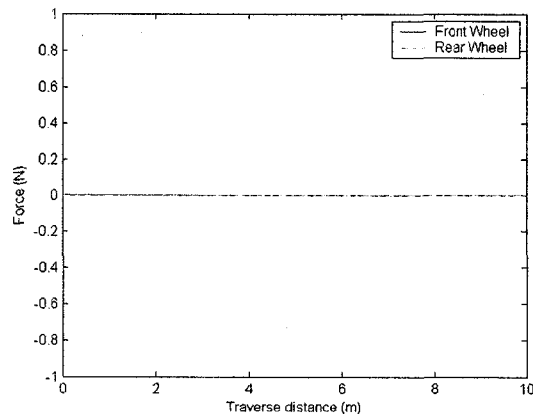


**Figure 5.6 Frictional forces**

## 5.2 A 7-DOF Full-Car Model.

A 7-DOF full-car model was discussed in [5.2]. The work focused on ride comfort with the implementation of active-suspensions, and a PID controlled passenger seat. The controls of the vehicle body's bounce and pitch motions, and the seat's bounce motion were used alternatively to obtain the optimal comfort. In the suspension systems, a linear dry friction model was introduced in studying the vertical response of the vehicle body. In what follows, only the mathematical structure of the vehicle model is extracted, and the present model is simplified to having the same DOFs. The aim is to investigate the vehicle's responses to vertical road disturbances.

### 5.2.1 A Full-Car Model by Rahmi.

This model was reviewed in Section 3.5.4, see Figure 3.18 in particular. The DOFs included the bounces of the vehicle body and the wheels, respectively; and the roll and pitch of the vehicle body. The model was considered to be stationary in the sense that the horizontal motions, that is, the longitudinal, lateral and yaw motions, were neglected. Wheel spinning was also discarded. The resulting state equations were nonlinear because of the trigonometric terms involved. In addition, the model consisted of four independent suspensions with friction on dampers. The friction was described by, where  $n = 1, \dots, 4$

$$f_n = C e_n (\Delta \dot{z}_n) \quad (5.6)$$

$$C e_n = \begin{cases} N & \text{if } |\Delta \dot{z}_n| < \varepsilon \\ \frac{N}{\pi} (2\rho_n - \sin 2\rho_n) + \frac{4R}{\pi (\Delta \dot{z}_n)} \cos \rho_n & \text{otherwise} \end{cases} \quad (5.7)$$

$$\rho_n = \sin^{-1} \left( \frac{\varepsilon}{\Delta \dot{z}_n} \right) \quad (5.8)$$

In the above equations,  $\Delta \dot{z}_n$  is the relative velocity between the two ends of the  $n$ -th suspension, and is determined by equation (3.12). The parameter  $\varepsilon$  is a small constant band values implemented to prevent the complete locking of the suspension when  $\Delta \dot{z}_n = 0$ . The constant  $R$  is given as the dry friction force under the condition of low  $\Delta \dot{z}_n$ . In the range where  $|\Delta \dot{z}_n| > \varepsilon$ , the damping friction approaches  $R$ . Reference [5.2] listed the values of  $\varepsilon$  and  $R$  (see Table 5.3). They had been verified with experimental data, see [5.2]. Figure 5.7 shows the behavior of this friction model.

**Table 5.3 Parameters  $\varepsilon$  and  $R$ \***

Parameters	Values	Unit
$\varepsilon$	0.0012	m/s
$R$	22	N

\* from [5.2]

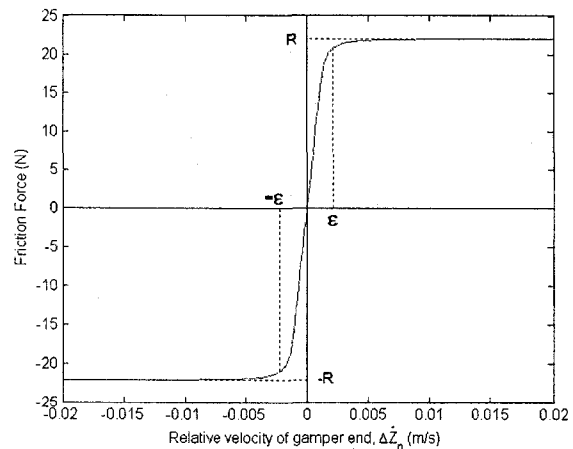


**Figure 5.7 Dry friction behavior**

It should be pointed out that the additional DOF representing the seat bounce motion is excluded, in order to compare with the present model. As a result, passive, instead of active, suspension is employed. Time responses of the model are made by simulating the vehicle traveling over the bump without steering.

### 5.2.2 The Present Model.

The present model is reduced to 7 DOFs since  $\ddot{x} = \dot{x} = x = \ddot{y} = \dot{y} = y = \ddot{\phi} = \dot{\phi} = \phi = \dot{\omega}_n = \omega_n = 0$ .

In addition, the external forces components generated from road-tire interactions and wheel torque inputs are not considered. As a result, the internal reaction forces  $P_{xcw,n}$  and  $P_{ycw,n}$  are zero. The new set of state equations becomes, for the bounce motions of the wheels,

$$\begin{aligned} m_n \ddot{z}_n &= k_{sn}(z + y_n \phi - x_n \gamma - z_n) \\ &+ c_{sn}(\dot{z} + y_n \dot{\phi} - x_n \dot{\gamma} - \dot{z}_n) - k_{tn}(z_n - z_{sn}) + f_n \end{aligned} \quad (5.9)$$

for the bounce motion of the vehicle body,

$$M_b \ddot{z} = - \sum \left[ \begin{array}{l} k_{sn}(z + y_n \phi - x_n \gamma - z_n) \\ + c_{sn}(\dot{z} + y_n \dot{\phi} - x_n \dot{\gamma} - \dot{z}_n) \end{array} \right] - \sum f_n \quad (5.10)$$

and for the pitch-roll motions of the vehicle body,

$$\begin{aligned} I_{x,cg} \ddot{\phi} &= - \sum \{ [k_{sn}(z - x_n \gamma + y_n \phi - z_n)] y_n \} \\ &- \sum \{ [c_{sn}(\dot{z} - x_n \dot{\gamma} + y_n \dot{\phi} - \dot{z}_n)] y_n \} + \sum y_n f_n \\ I_{y,cg} \dot{\gamma} &= \sum \{ [k_{sn}(z - x_n \gamma + y_n \phi - z_n)] x_n \} \\ &+ \sum \{ [c_{sn}(\dot{z} - x_n \dot{\gamma} + y_n \dot{\phi} - \dot{z}_n)] x_n \} + \sum x_n f_n \end{aligned} \quad (5.11)$$

For easy comparison, the dry friction model of equations (5.6) through (5.8) is used.

### 5.2.3 Simulation Results and Discussions.

To observe the time responses of the models, both models are hypothetically given a constant vehicle speed of 10 m/s over the bump without steering. The model parameters are listed in Table 5.4. A ramp-like bump profile is selected with a height of 0.035 m and a span of 0.1 m, as shown in Figure 5.8. The road disturbance is inputted to each wheel with a time delay (see Figure 5.9) between the front and rear axles. That is, the time delay is  $\Delta t = (a + b)/V$ , where  $a + b$  is the wheelbase (see Figure 3.6), and  $V$  the longitudinal speed of the vehicle.

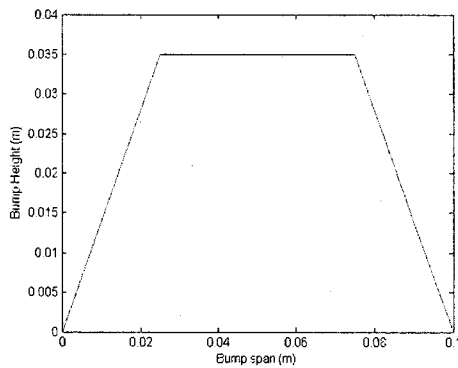


Figure 5.8 Ramp-like bump profile

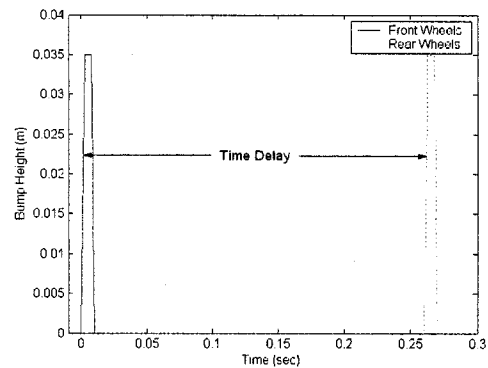
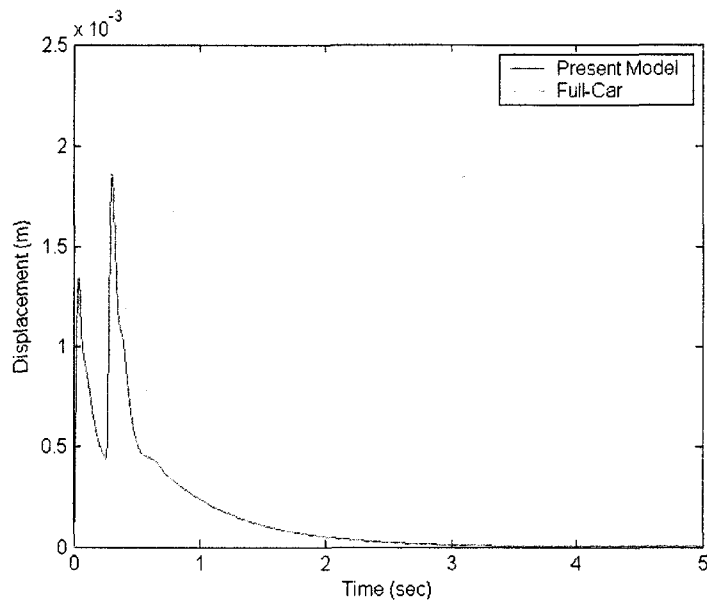


Figure 5.9 Time-delay at 10 m/s

The simulation results are shown in Figures 5.10 and 5.11. The time responses from both models are found to be identical. The time-delay effect of axles traveling over the bump is clearly seen in vertical displacement and acceleration, and pitch angle (figure 5.10); it is also seen in the dampers' friction forces (Figure 5.11).

**Table 5.4 Model Parameters**

<b>Vehicle Body</b>		
Parameter	Description (Unit)	Value
$M_b$	Vehicle point mass at <i>CG</i> (kg)	1100
$x_1, x_2$	<i>x</i> -coordinates of front axles to <i>CG</i> (m)	1.2
$x_3, x_4$	<i>x</i> -coordinates of rear axles to <i>CG</i> (m)	-1.4
$y_1, y_3$	<i>y</i> -coordinates of left wheels to <i>CG</i> (m)	-0.75
$y_2, y_4$	<i>y</i> -coordinates of right wheels to <i>CG</i> (m)	0.75
$I_{x,CG}$	Moment of inertia about <i>x</i> -axes (kg m <sup>2</sup> )	550
$I_{y,CG}$	Moment of inertia about <i>y</i> -axes (kg m <sup>2</sup> )	1848
<b>Wheels</b>		
$m_1, m_2$	Mass for front Wheels (kg)	25
$m_3, m_4$	Mass for rear Wheels (kg)	45
<b>Suspension/Tire Stiffness</b>		
$k_{s1}, k_{s2}$	Front suspension spring coefficient (N/m)	15000
$k_{s3}, k_{s4}$	Rear suspension spring coefficient (N/m)	17000
$c_s$	All suspension damping coefficient (N.s/m)	2500
$k_t$	All tire stiffness coefficient (N/m)	250000



**Figure 5.10a Vertical displacement of vehicle body**

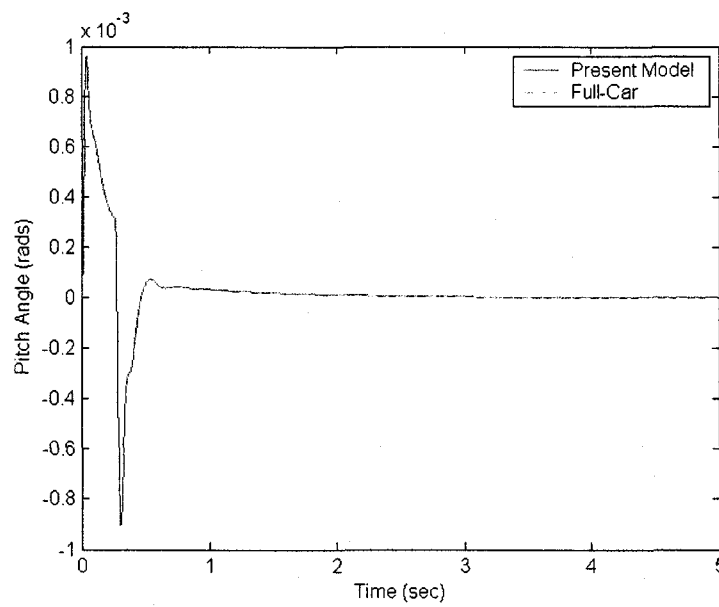


**Figure 5.10b Pitch angle of vehicle body**

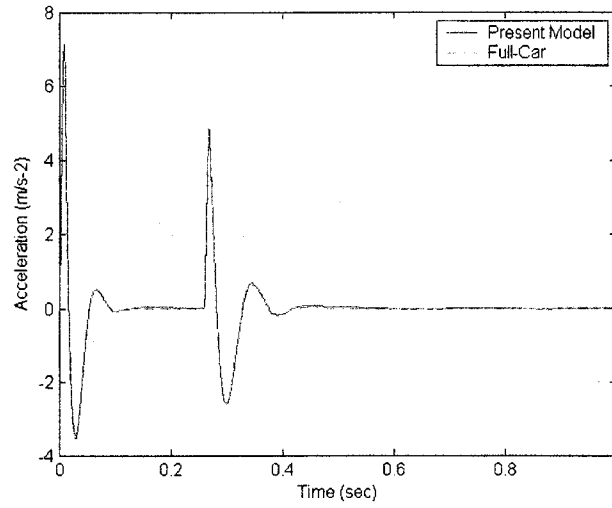


**Figure 5.10c Vertical acceleration of vehicle body**

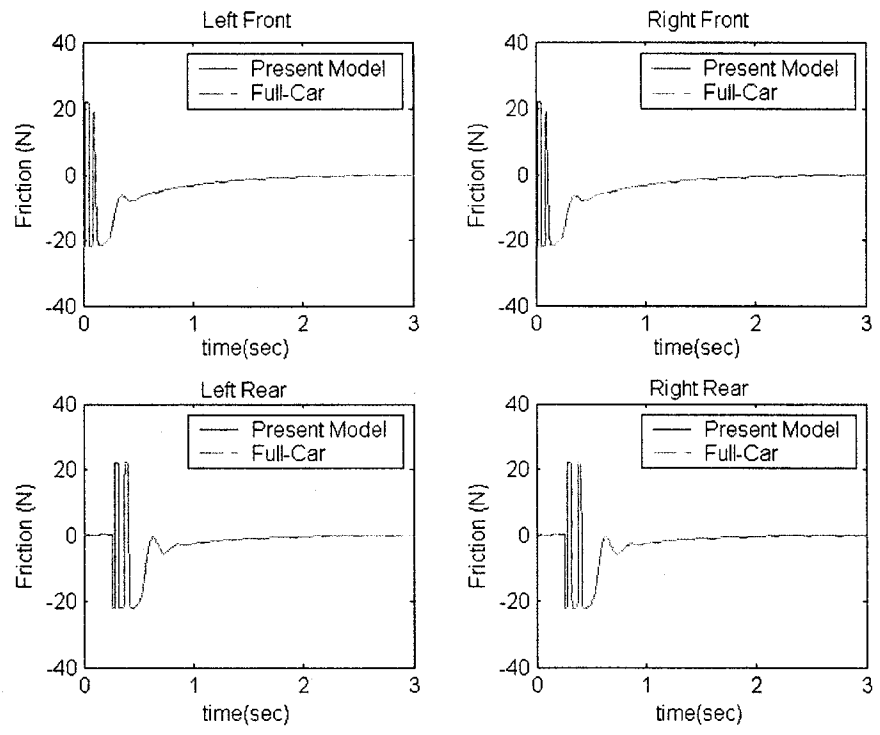


**Figure 5.11 Damper friction forces**

### **5.3 A Full-Car Model for Maneuver Simulation.**

#### 5.3.1 The Full-Car Model by Villella.

In studying ground vehicle handling, a 7-DOF full-car model with the application of the 2-D LuGre friction model has been introduced by [5.3] of Georgia Institute of Technology. The focus of the study was the effect of the wheels' input torques on the lateral-yaw response of the vehicle. The vehicle model included five lumped masses, one lumped translational mass that was the vehicle body, and four lumped rotational masses that were the four wheels. The translational mass was to represent the horizontal motion of the vehicle body while the rotational masses were to represent the spinning motion of the wheels. Most importantly, the model had no suspensions due to the assumption that "suspension forces are internal to a vehicle system and have no effect on the motion of the entire system in the horizontal plane" [5.3]. As a result, the effects of pitch-roll, and the bounce of the wheels were neglected while the vehicle was cornering. The DOFs included the longitudinal motion, and the lateral motions and the yaw of the vehicle body; and the spins of the wheels, for a total of seven.

In addition to the absence of a suspension system, an analytical method for solving for normal force distribution amongst the four wheel contact points was proposed, where the solution produced the forces necessary to maintain zero pitch and roll conditions. The

resulting algebraic equations depended only on the vehicle's geometric parameters, friction forces, and steering angles. As to frictional force, the 2-D LuGre model of Reference [4.2] was implemented. In contrast to the static friction model, such as the "magic formula", the large transient friction forces were captured as the steer angle is changing, where a rapid increase of contact forces may be achieved.

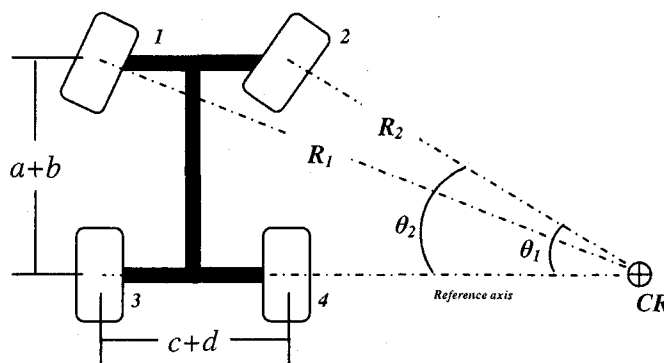


**Figure 5.12 Steering geometry definition (showing right steering) [5.3]**

The inputs to the model were composed of four independent wheel torques, and four time-varying steering signals sent from the driver.

These four steering signals were

not independent. As demonstrated by the steering geometry definition of Figure 5.12, which shows only the geometry of a right steer, the rear steering angles were fixed at zero steer, and the front steer angles,  $\theta_1$  and  $\theta_2$ , were constrained by having their respective  $y$ -axes,  $R_1$  and  $R_2$ , intersect at the same point. The reason of so doing was, according to [5.3], "so that no wheel slip is induced by the steering geometry, allowing for the possibility of zero relative velocity solutions at all four wheels." In other words, in order not to introduce "artificial slip", the input steer angles are not independent. Instead, the

angles are given by  $\theta_1, \theta_2 = \tan^{-1} \left( \frac{(a+b)}{\frac{(a+b)}{\tan \theta_1} + (c+d)} \right)$  and  $\theta_3 = \theta_4 = 0$ , for the case of left

steering; and by  $\theta_1, \theta_2 = \tan^{-1} \left( \frac{(a+b)}{\frac{(a+b)}{\tan \theta_1} - (c+d)} \right)$  and  $\theta_3 = \theta_4 = 0$ , for the case of right

steering, where  $(a+b)$  and  $(c+d)$  are the wheelbase length and width of the vehicle, respectively.

### 5.3.2 The present model.

The present model, whose development was dealt with in Chapter 3, has 14 DOFs in total, and considers the vehicle body and the wheels as two inter-dependent sub-systems of rigid-bodies. The suspensions, or the “spring-damper” units, represent the connections of the wheels to the vehicle body, and introduce the required inertial coupling, restraints and forces between the two sub-systems. Normal forces are solved from the consideration of dynamic equilibrium. It is interesting to note that, although the present model has 14 DOFs compared with the 7 DOFs used in [5.3], it requires less CPU time than that by the approach of [5.3]. A typical run of [5.3] takes 38 seconds of CPU time; while the present model requires, on average, 5 to 10 seconds less. In addition, it should be noted that in the remainder of this chapter, the results obtained by using the approach of [5.3] will be denoted “G-Tech” in the plots for the abbreviation of Georgia Institute of Technology.

### 5.3.3 Simulation Results and Discussions.

The state-space equations of motion for both models are solved using MatLab®. A few scenarios are considered. Note that for all scenarios, the vehicle is maneuvered under the steering input of  $\theta_1(t)$  given in Figure 5.13. The steering transition begins with zero to -10 degrees (-0.176 radians) and back to zero, which causes the vehicle to turn left. The other

three steering inputs are therefore,  $\theta_2 = \tan^{-1} \left( \frac{(a+b)}{\frac{(a+b)}{\tan \theta_1} + (c+d)} \right)$  and  $\theta_3 = \theta_4 = 0$ .

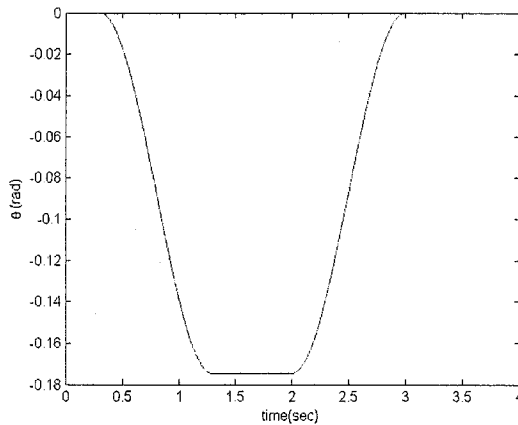


**Figure 5.13 Driver steering input**

The other model parameters are listed in Table 5.5. Note that the friction parameters are taken from [5.3]; the vehicle mass, mass moment of inertia and geometry parameters are taken from measurements on a 1998 Honda

Civic by the United States National Highway Traffic Safety Administration (NHTSA) [5.4]; the spring-damping-tire stiffness constants are taken from [5.2]. It should be pointed out that, though the wheel's mass moment of inertia is taken from [5.3], the wheel mass and geometry are chosen according to Honda's specification [5.4] owing to data availability.

Several simulation scenarios are examined. First, the vehicle is given steer angles for a turn maneuver on pavement road with no wheel torque input to the wheels. Next, the vehicle is subjected to the same steer angles and road surface conditions but input torques are applied to all four wheels so as to simulate four-wheel drive. Finally, the model is put to an icy road surface and simulations are performed for a four-wheel driven, a front-wheel driven and a rear-wheel driven vehicle, respectively.

#### 5.3.3.1 Simulation of turn maneuver without input torques to the wheels.

Initially, the model is simulated under turn maneuver on pavement road with no wheel torque input to the wheels. The simulation is run with an initial longitudinal speed of 15 m/s [5.3]. Initial wheel speeds are then determined via no-slip condition  $\dot{x} = r\omega$ , leading to the values of -75 rad/s. The negative sign is needed due to the use of wheel center coordinates, see Section 3.1, and Figure 3.2 in particular. All other states are initially zero. The simulated results show the extent to which vehicle dynamics is influenced by the friction between the road and wheels.

**Table 5.5 Model Parameters**

Parameter	Description (Unit)	Value
<b>Vehicle Body [5.4]</b>		
$M_b$	Vehicle point mass at $CG$ (kg)	1140
$x_1, x_2$	$x$ -coordinates of front axles to $CG$ (m)	1.1
$x_3, x_4$	$x$ -coordinates of rear axles to $CG$ (m)	-1.5
$y_1, y_3$	$y$ -coordinates of left wheels to $CG$ (m)	-0.7
$y_2, y_4$	$y$ -coordinates of right wheels to $CG$ (m)	0.7
$H+r$	Height from ground surface to $CG$ (m)	0.5
$I_{x,cg}$	Moment of inertia about $x$ -axis ( $kg\ m^2$ )	365
$I_{y,cg}$	Moment of inertia about $y$ -axis ( $kg\ m^2$ )	1617
$I_{z,cg}$	Moment of inertia about $z$ -axis ( $kg\ m^2$ )	1785
<b>Wheels [5.4]</b>		
$m_n$	Mass of one wheel (kg)	25
$r$	Wheel radius (m)	0.2
$I_{spin}$	Moment of inertia about $y_{cw}$ ( $kg\ m^2$ )	0.1361
<b>Suspension and Tire Stiffness [5.2]</b>		
$k_s$	Suspension spring constant (N/m)	17000
$c_s$	Suspension damper coefficient (N.s/m)	2500
$k_t$	Tire stiffness constant (N/m)	250000
<b>LuGre Friction [5.3]</b>		
$\sigma_{0x}$	Longitudinal rubber stiffness ( $m^{-1}$ )	178
$\sigma_{1x}$	Longitudinal rubber damping (s/m)	1
$\sigma_{2x}$	Longitudinal viscous relative damping (s/m)	0
$\sigma_{0y}$	Lateral rubber stiffness ( $m^{-1}$ )	500
$\sigma_{1y}$	Lateral rubber damping (s/m)	2
$\sigma_{2y}$	Lateral viscous relative damping (s/m)	0
$\delta$	Stribeck exponent	0.5
$v_s$	Stribeck velocity (m/s)	5.5
<b>Coefficient of Friction [5.3]</b>		
$\mu_k$	Kinetic, rubber-asphalt contact	0.8
$\mu_s$	Static, rubber-asphalt contact	1.2
$\mu_k$	Kinetic, rubber-ice contact	0.1
$\mu_s$	Static, rubber-ice contact	0.2

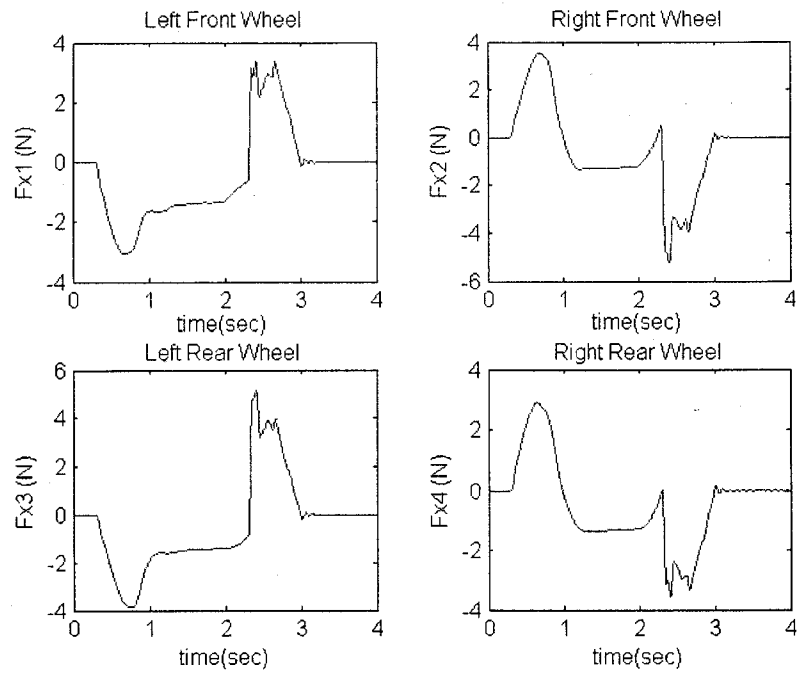


**Figure 5.14a Longitudinal friction forces**

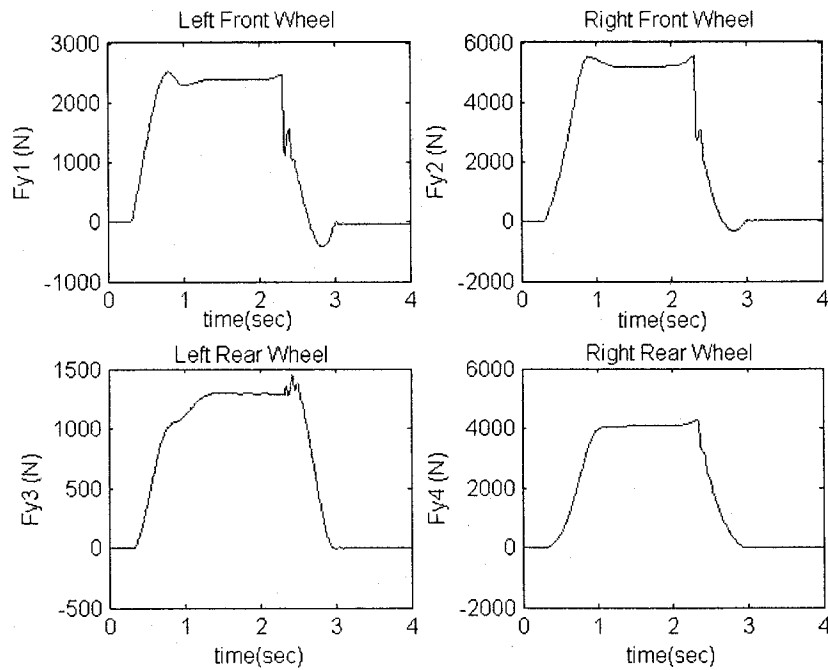


**Figure 5.14b Lateral friction forces**

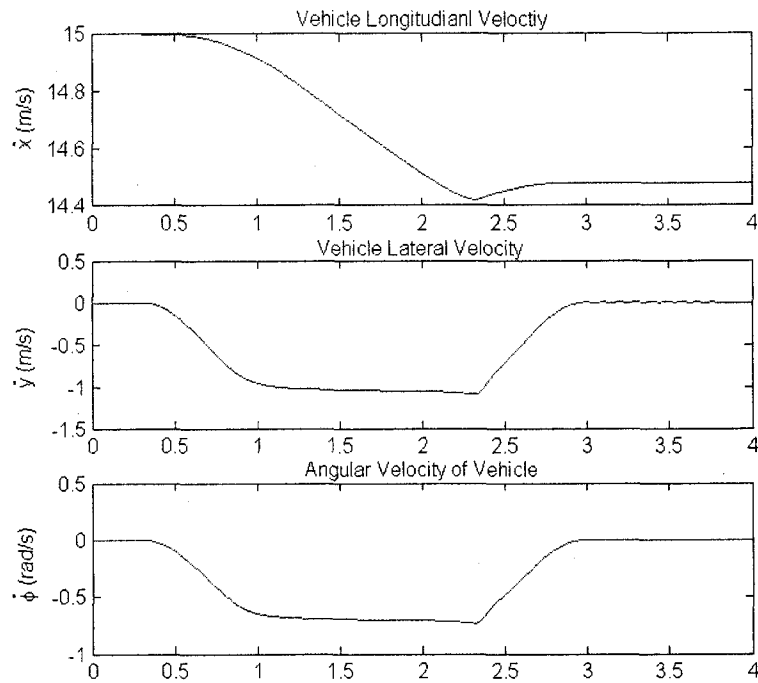


**Figure 5.15 Vehicle body speeds for pavement road with no torque input**

1) Vehicle body velocities in the horizontal plane are shown in Figure 5.15. From

Figure 5.14a, it is clearly seen that the speed change as shown in Figure 5.15 is due to the emergence of friction forces. The longitudinal speed decreases slightly after the turn begins (0.5 s versus 0.35 s, see Figure 5.15), where the presence of longitudinal frictional forces dissipates the forward kinetic energy, resulting in a lower speed slightly ahead of the completion of the turn ( $t = 2.75$  s versus 3.0 s, see Figure 5.13). On the other hand, the appearance of lateral frictional forces accelerates the vehicle in the lateral direction, and the moment created by these friction forces about the mass center of the vehicle body causes the yaw motion of

the vehicle. In other words, the lateral speed and yaw rate increases and returns to zero at the completion of the turn without visible time-lag or advance (Figure 5.15).

- 2) The motions of the wheels are also influenced by friction. See Figure 5.16 for each wheel's rotational speed, where, due to the use of wheel center coordinates, a negative rotational speed represents a forward rolling motion. The wheel's rotational speeds on the left and right sides of the vehicle diverge as the left wheels slow down and the right wheels speed up to traverse turns of differing radii. One may also refer to Figure 5.12. As the vehicle turns about the center of rotation,  $CR$ , each wheel center will rotate at some constant angular speed with respect to  $CR$ ; as a result, the linear speeds of the wheel centers satisfy, for a left turn in particular,  $|V_{cw2}| > |V_{cw4}| > |V_{cw1}| > |V_{cw3}|$ , since it is seen that

$R_2 > R_4 > R_1 > R_3$ . Thus, given the relation of  $\omega_n = \frac{V_{cw,n} \vec{i}}{r}$ , the wheels' rotational speeds satisfy  $|\omega_2| > |\omega_4| > |\omega_1| > |\omega_3|$ , which is clearly exhibited in Figure 5.16.

- 3) As shown in Chapter 4, the bristle deflections are a result of the relative motions. The computed relative velocities and bristle deflections are given in Figures 5.17 and 5.18. The bristles deflect longitudinally and laterally when steering begins,

reach steady-state values as the steer angle is held fixed, and return to zero deflection when cornering is complete. The dynamic coefficients of friction are proportional to bristle deflection, which is verified by Figure 5.19 where the dynamic frictional coefficients are seen to have identical traits to bristle deflections shown in Figure 5.18, albeit different magnitudes.

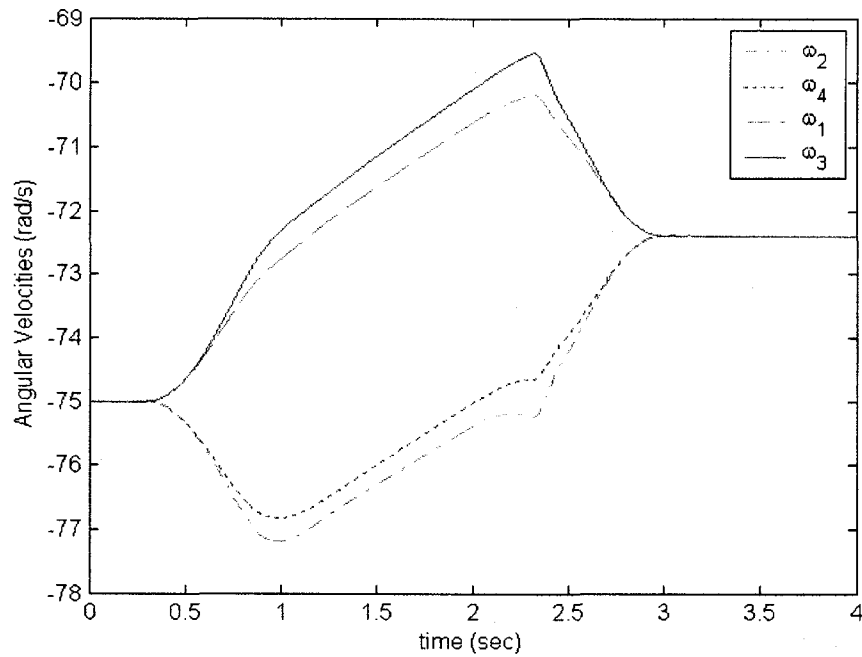


**Figure 5.16** Wheels' rotational speeds with no torque input

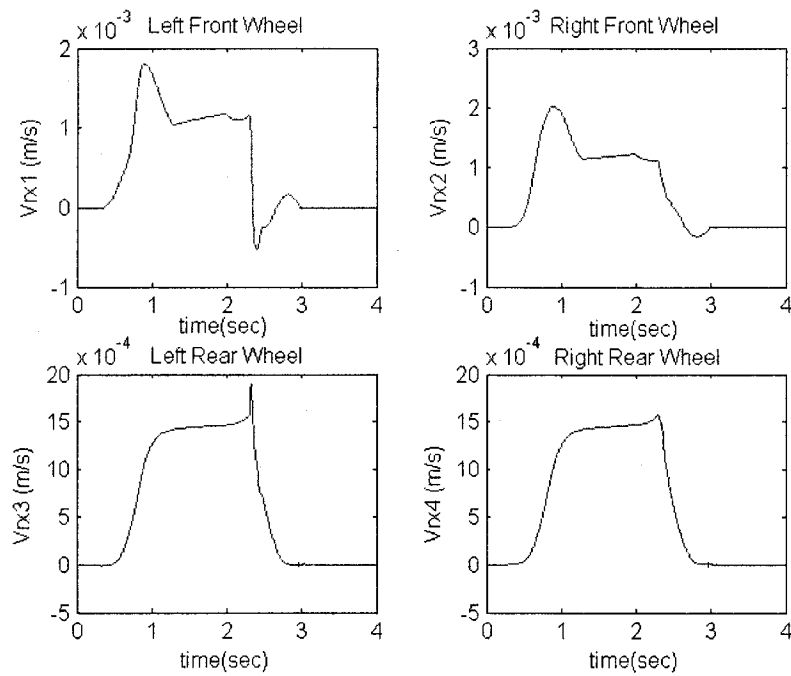


**Figure 5.17a Longitudinal relative velocity of each wheel with no torque input**

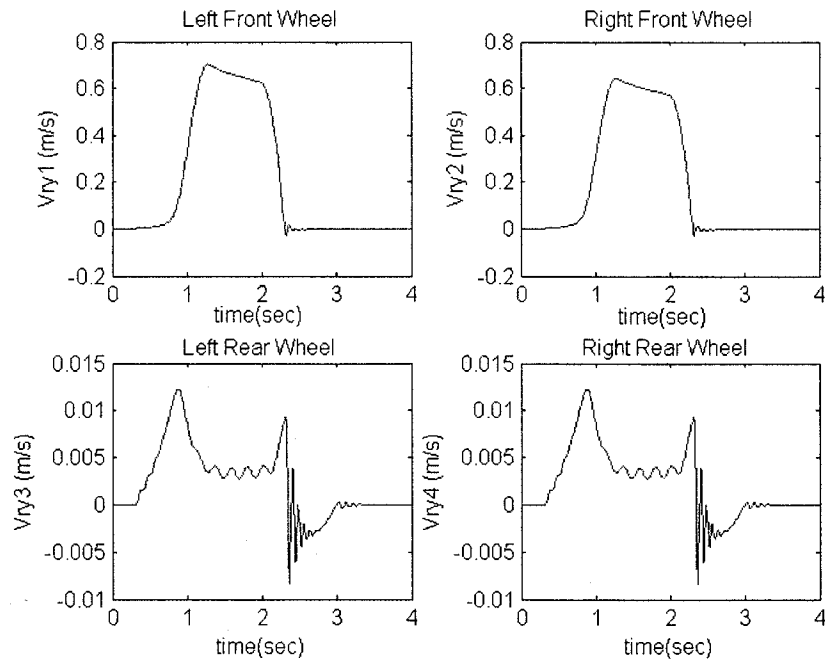


**Figure 5.17b Lateral relative velocity of each wheel with no torque input**

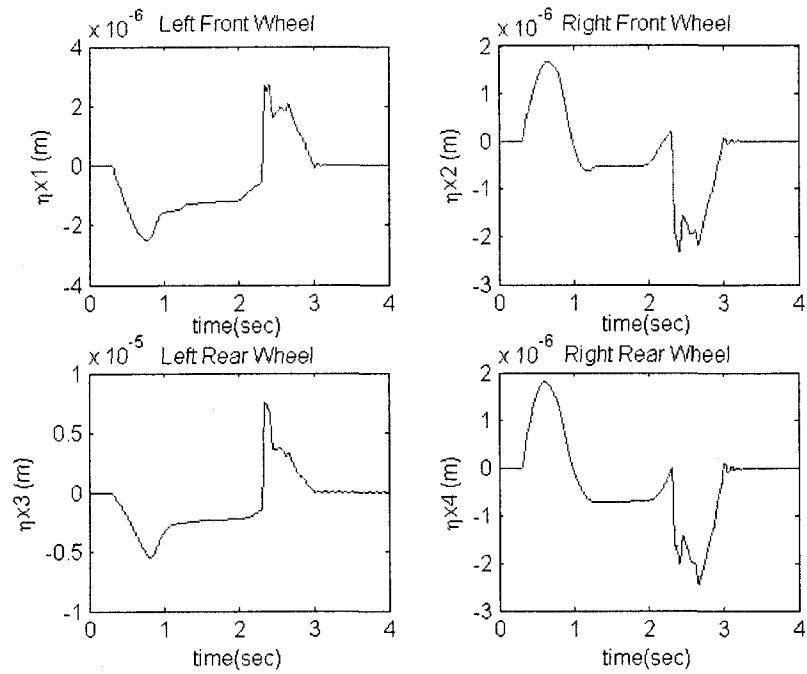


**Figure 5.18a Longitudinal bristle deflection at each wheel**

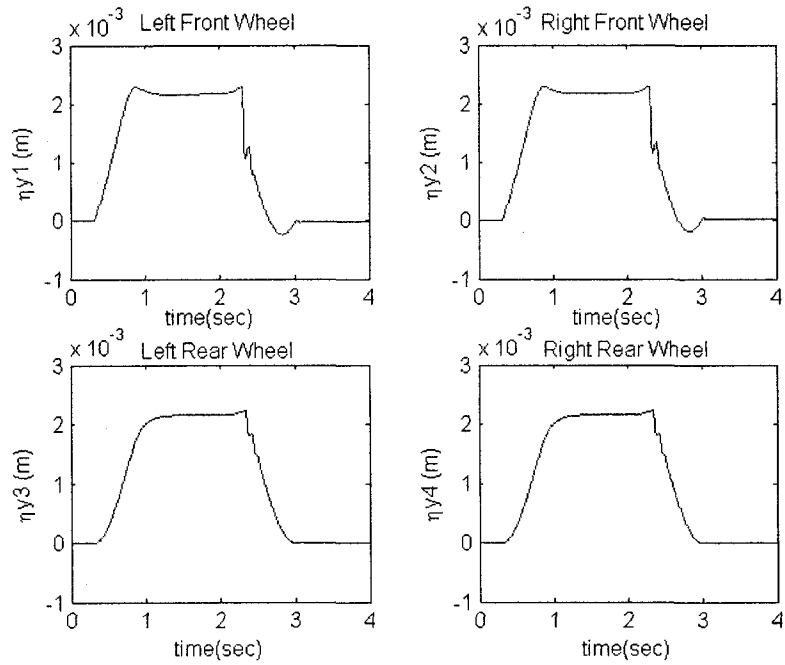


**Figure 5.18b Lateral bristle deflection at each wheel**

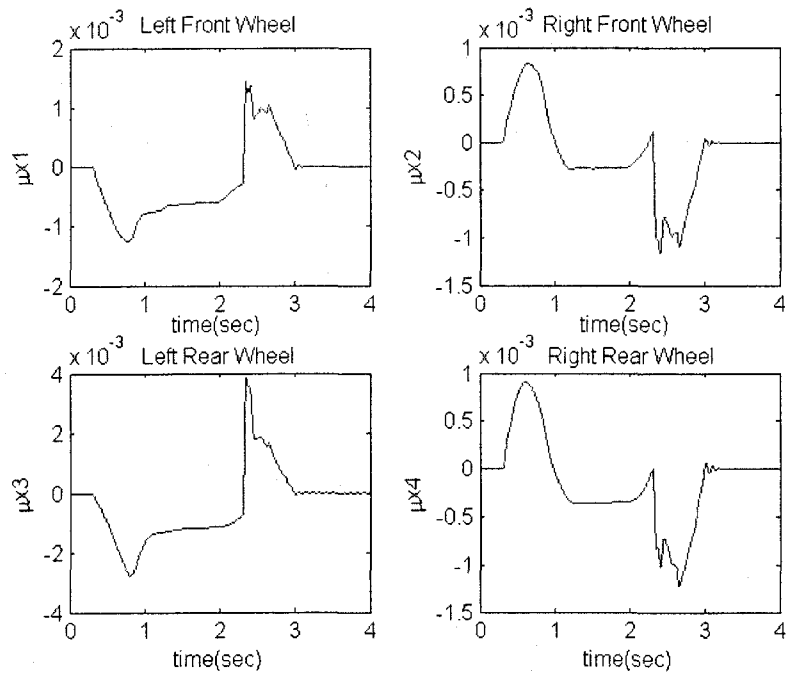


**Figure 5.19a Longitudinal dynamic friction coefficients**

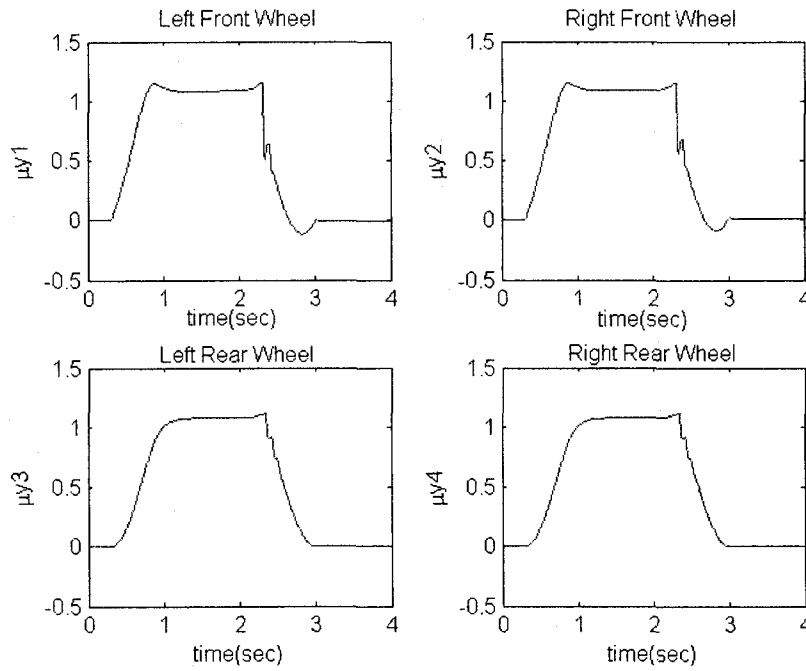


**Figure 5.19b Lateral dynamic friction coefficients**

4) Normal forces exerted on the wheels are shown in Figure 5.20. Higher normal forces at the front wheels are the result of a center of gravity which is closer to the front wheels. As the vehicle turns, the normal forces increase on the right side and decrease on the left side by the same amount. This means that the springs and tires on the left side of the vehicle are compressed more than those on the right side. Since the road surface is assumed even, the differences in tires' normal compressions or forces could result in the different lateral friction forces among the tires and further introduce a greater or a less turning moment to facilitate the tuning of the vehicle.

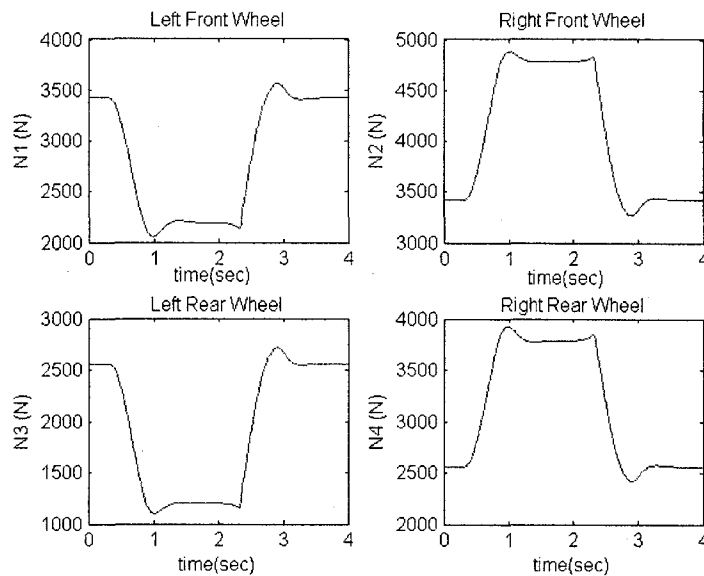


**Figure 5.20 Normal forces during turn maneuver**

Finally, by plotting the vehicle's position with respect to the global frame one is able to show the path of the vehicle, see Figure 5.21, where the dots represent successive positions of the vehicle's center of gravity,  $CG$ , and the arrows show successive traveling directions of the vehicle. The result is as expected, since the vehicle moves along a straight path, then turns left, and moves straight forward once the steering input ceases. Figure 5.21 also presents the path of the vehicle by the approach of [5.3] which is denoted as "G-Tech" as opposed to the "Present Model". The very close match seen in Figure 5.21 will be seen again in Figures 5.25b and 5.26b, for example.

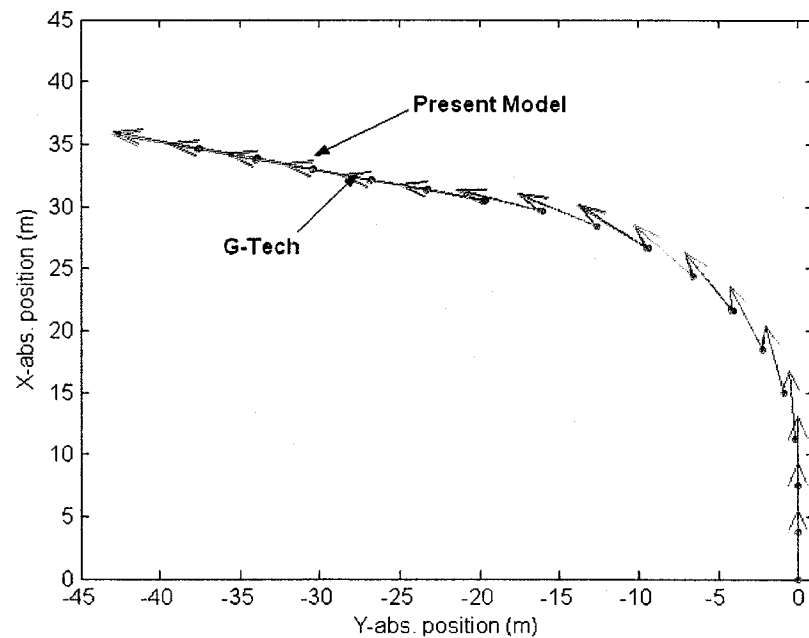


**Figure 5.21 Vehicle position with no torque input**

### 5.3.3.2 Simulation of turn maneuver with input torques to the wheels.

Next, an all-wheel drive vehicle is assumed. The present model is simulated by applying a 50 N-m input torque to each of the four wheels. Note that a positive torque will cause a wheel to roll forward (see Figure 3.12). The vehicle will accelerate on a paved road and under the same steering input as given in the previous scenario. The results of vehicle velocities are shown in Figure 5.22. The vehicle is indeed accelerating since the longitudinal speed has increased over the time period. However, the lateral velocity and yaw rate are lower than in the case of no applied torque. The lower lateral and yaw rates give rise to less turning motion. Such an effect is seen from the different paths that the vehicle will follow (see Figure 5.22). With torques applied to the wheels, the vehicle makes a wider turn. This is the result of a lower lateral frictional force “pushing the vehicle to turn.”

The longitudinal frictional forces increase by an almost equal amount among the four wheels (Figure 5.23a). These forces are negative because of the sign convention defined in Chapter 3, see Figure 3.12. Magnitude-wise, they are close to  $T_n/r_n = 250$  N, which is the tangential force at the wheel base and produced by the torque. On the other hand, the lateral frictional forces see slight increase or reduction, compared with the

pervious no-input-torque case. Overall, lower total lateral frictional force and turning moment lead to reduced lateral and angular accelerations of the vehicle body.

In addition, relative velocities  $V_{rx}$  and  $V_{ry}$  are plotted in Figure 5.24. According to the LuGre friction model, frictional forces are directly affected by  $V_r$ . It is seen in Figure 5.24 that  $V_{rx}$  and  $V_{ry}$  of the front wheels are much higher than the no-input-torque case. Since  $g(V_r)$  becomes closer to  $u_k$  when  $V_r$  increases, see equation (4.5), it is concluded that the increase in  $V_r$  causes a lower bristle deflection which in turn reduces the force produced by the bristle deflection. This means that the wheel may be unable to produce sufficient lateral frictional force to steer the vehicle as it did previously.

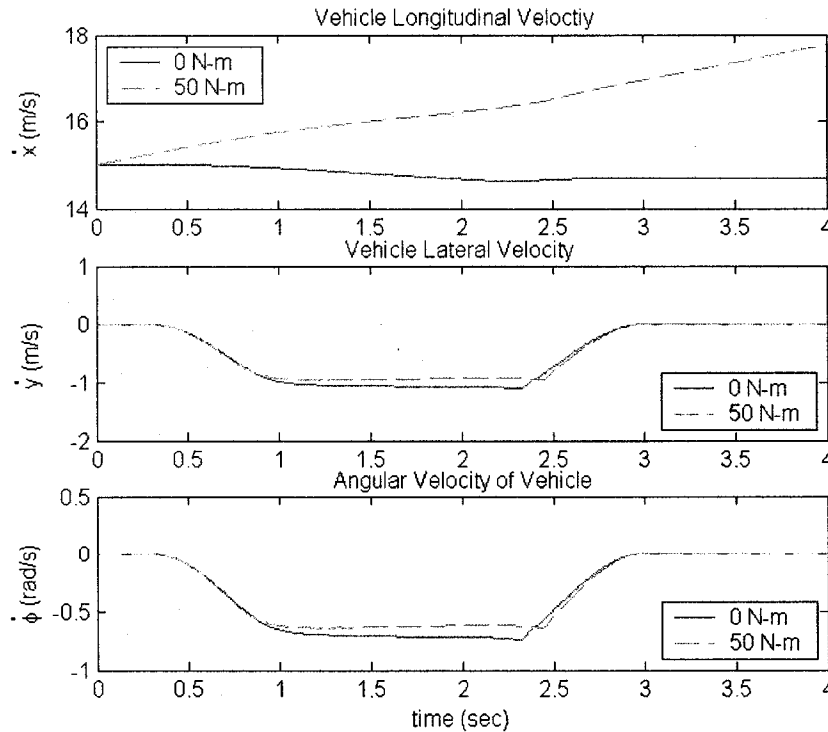


**Figure 5.22a Comparison of vehicle body speeds**

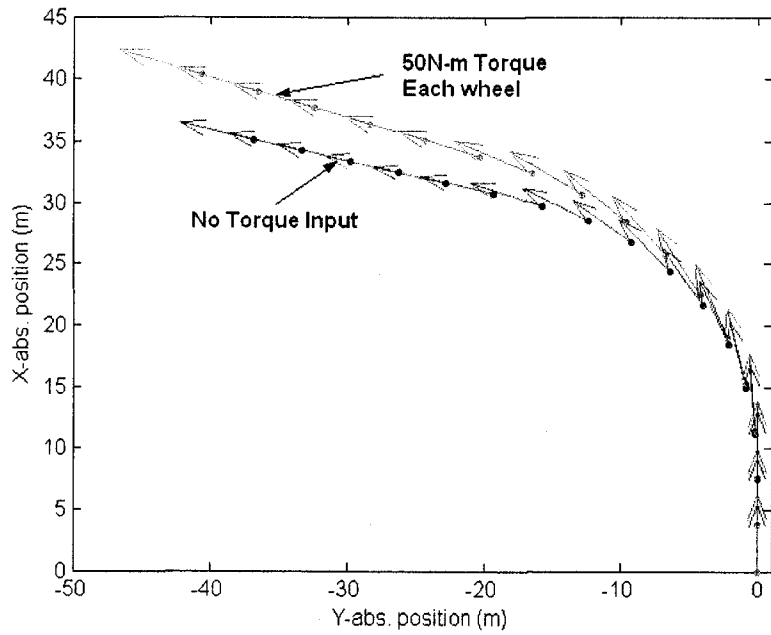


**Figure 5.22b Comparison of vehicle position**

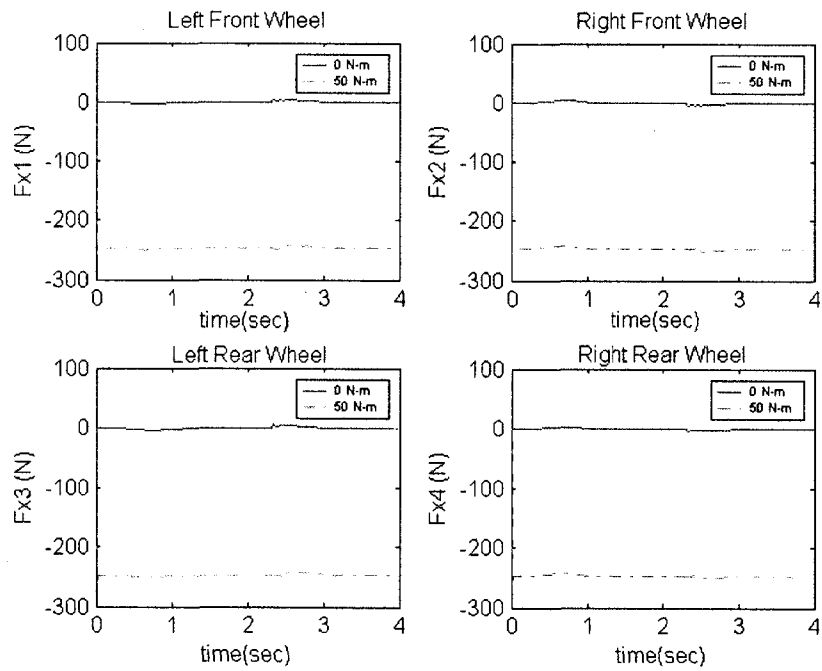


**Figure 5.23a Comparison of longitudinal frictional forces**

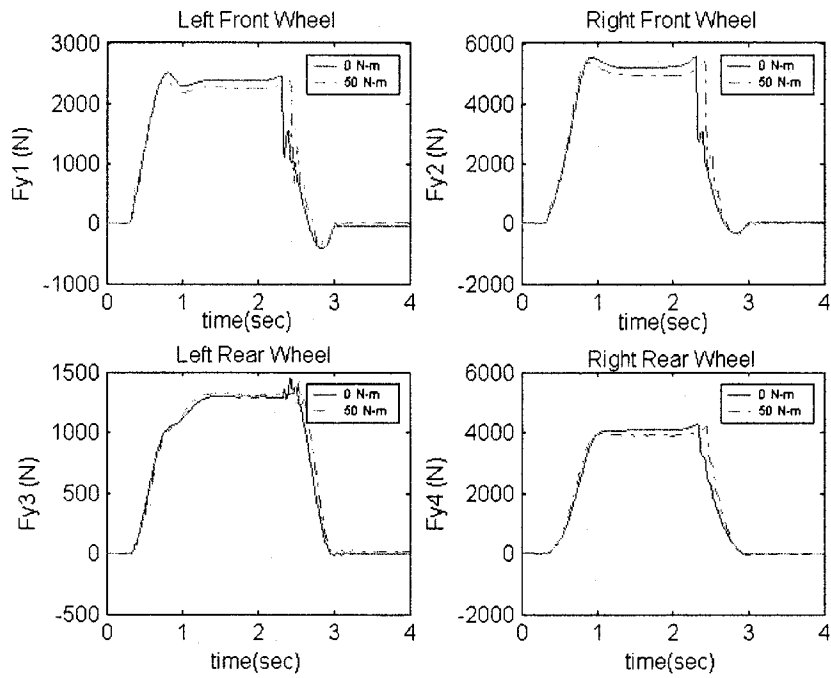


**Figure 5.23b Comparison of lateral frictional forces**

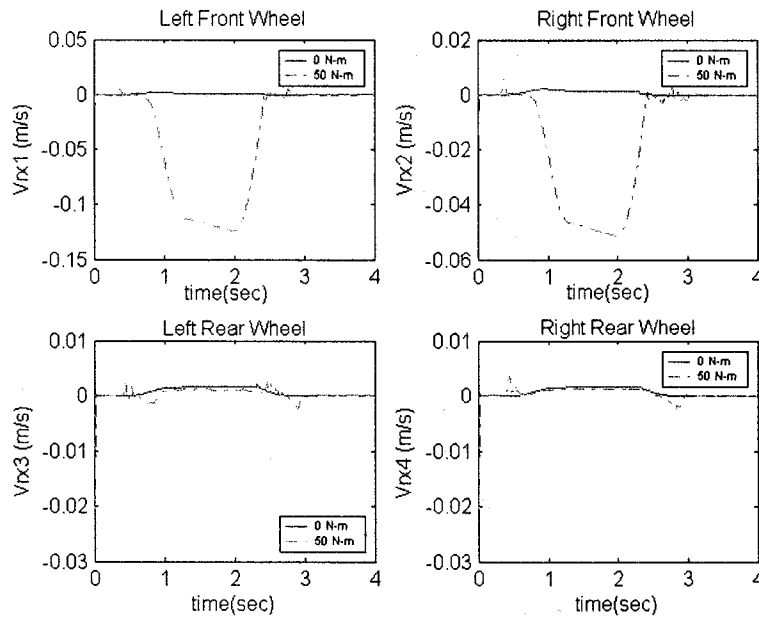


**Figure 5.24a Comparison of longitudinal relative velocities**

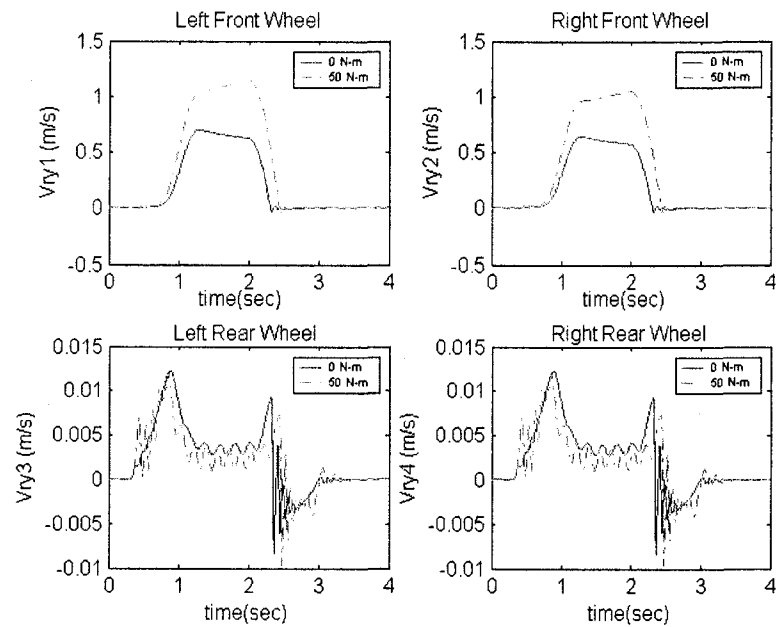


**Figure 5.24b Comparison of lateral relative velocities**

Therefore, in simulating the two scenarios, the present model seems to be able to capture the physical behavior of the vehicle. However, it is interesting to find that, though the vehicle speeds predicted by the present model and that by Vilella [5.3] are indistinguishable, the vehicle paths are visibly different, except for the case of no input torques (Figure 5.25b). It seems that the difference increases as the input torque increases (Figure 5.26b). The present model has predicted a greater turning radius. Further examination of results suggests that the cause may lie in the difference in modeling. Recalling that in [5.3], an algebraic method for solving for normal force distribution amongst the four wheel contact points was proposed, where the solution produced the forces necessary to maintain zero pitch and roll conditions. The method was governed by

the conditions of static force and moment balance for the vehicle and a hypothetical suspension whose spring constant was allowed to approach infinity. The present model, on the other hand, models the wheels' bounce motion in addition to that of the vehicle body and considers the dynamic equilibrium of the wheels as well as the vehicle body. The differences in suspension modeling results in different normal forces distribution between the two models (Figure 5.27), which in turn give rise to different lateral friction forces (Figures 5.28 and 5.29), and lead to different turning radii and driven paths. Note again that in the figures "G-Tech" refers to the approach of [5.3].

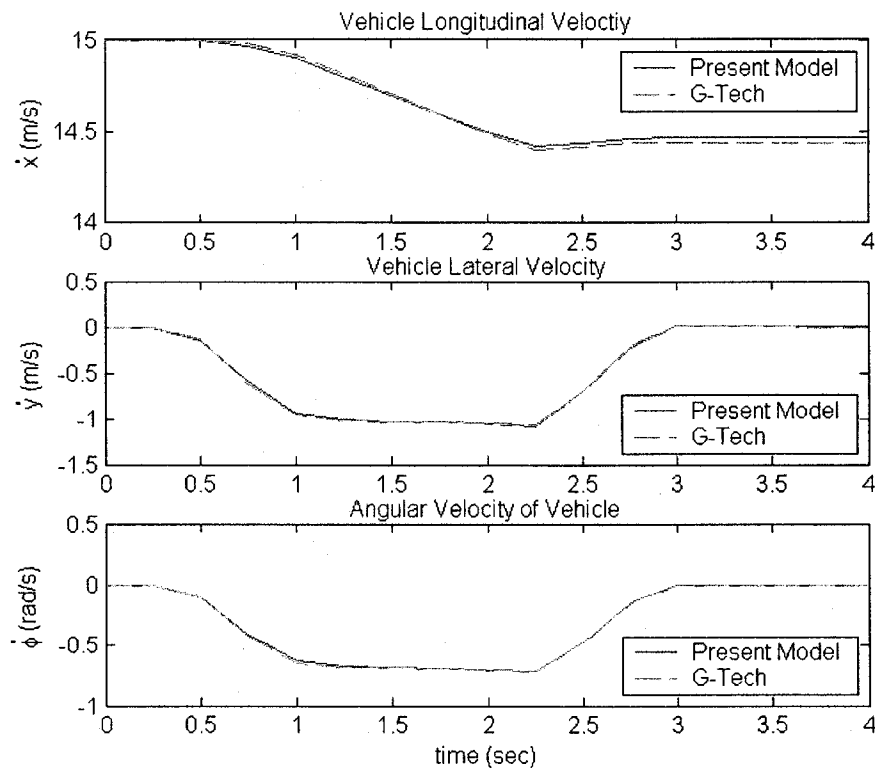


**Figure 5.25a Vehicle body speeds, no torque input**

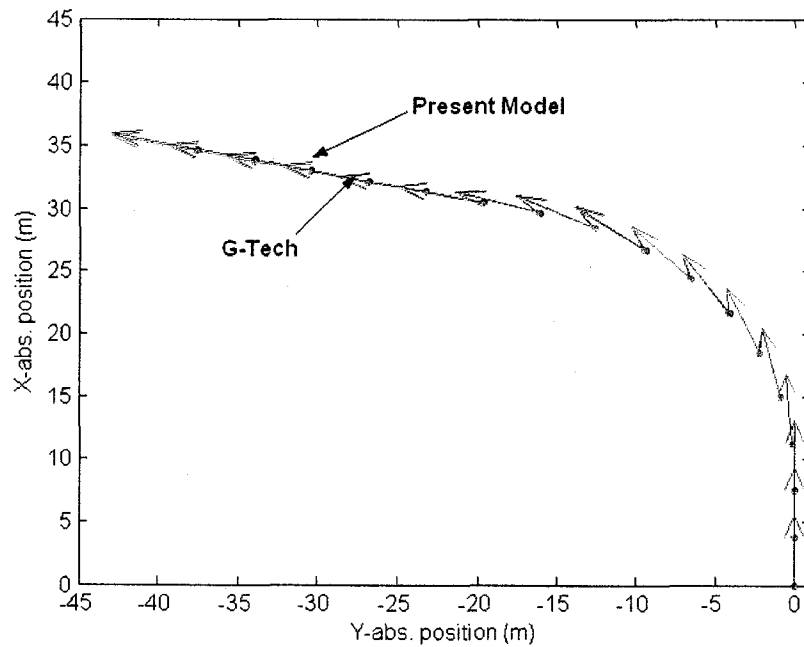


**Figure 5.25b** Vehicle position, no torque input

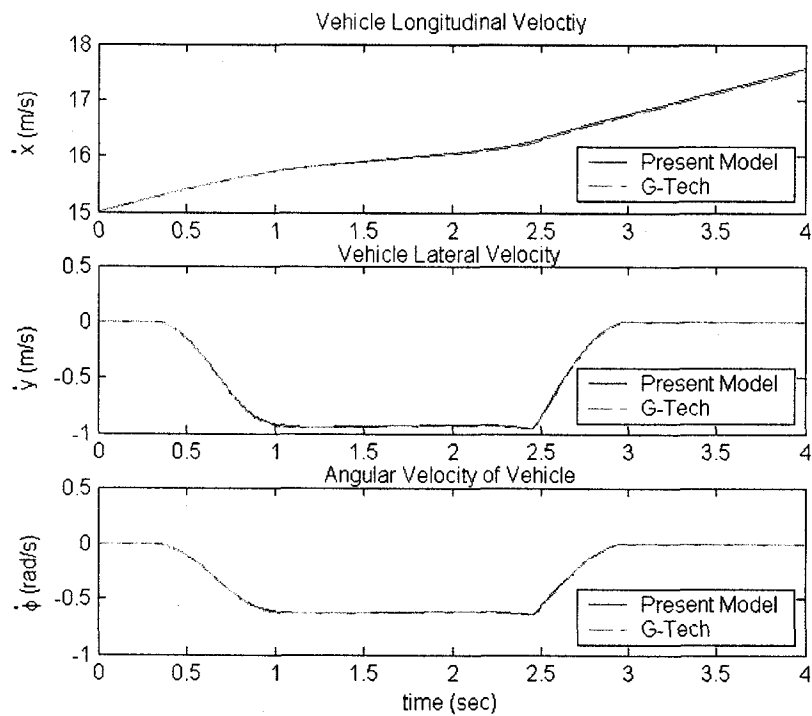


**Figure 5.26a** Vehicle body speeds, 50 N.m input torque

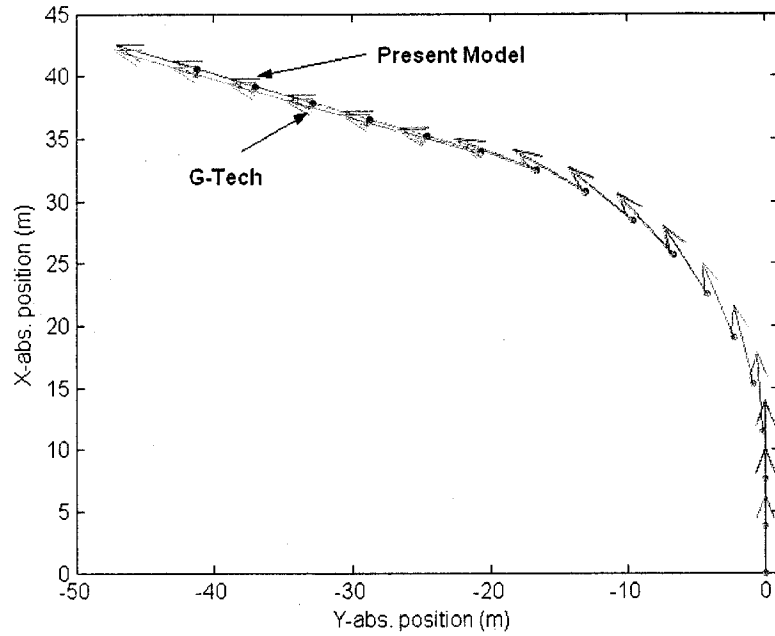


**Figure 5.26b Vehicle position, 50 N.m input torque**

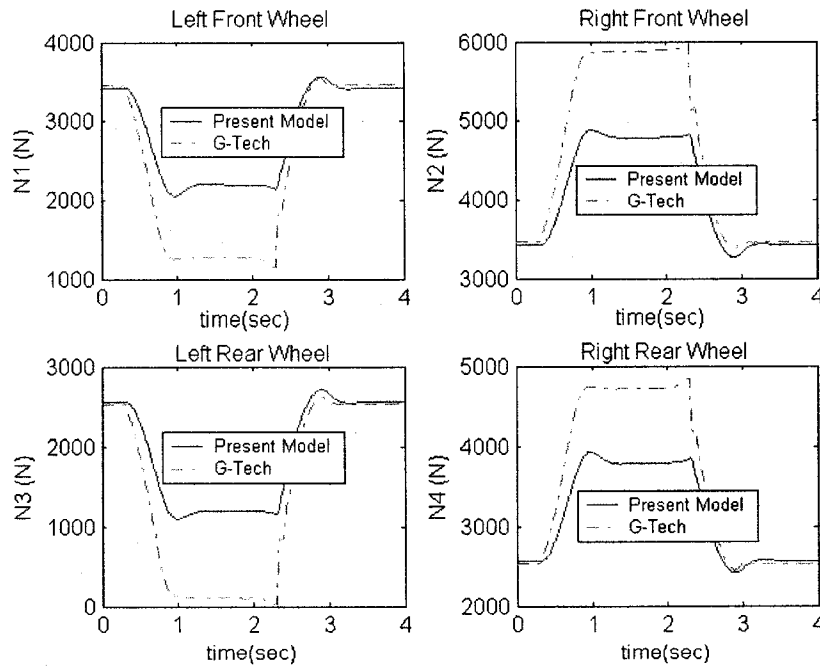


**Figure 5.27a Normal forces for turn maneuver with no torque input**

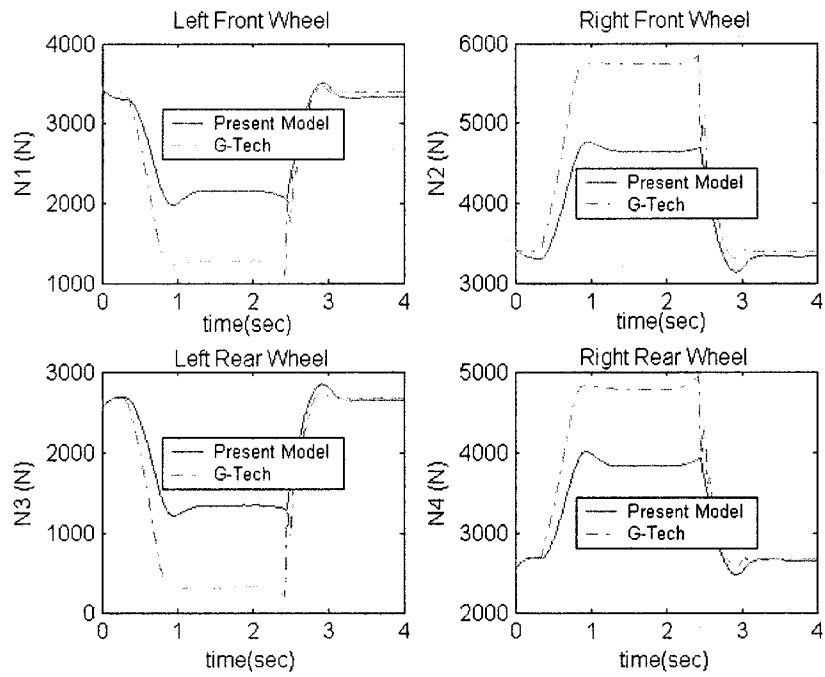


**Figure 5.27b Normal forces for turn maneuver with 50 N.m torque input**

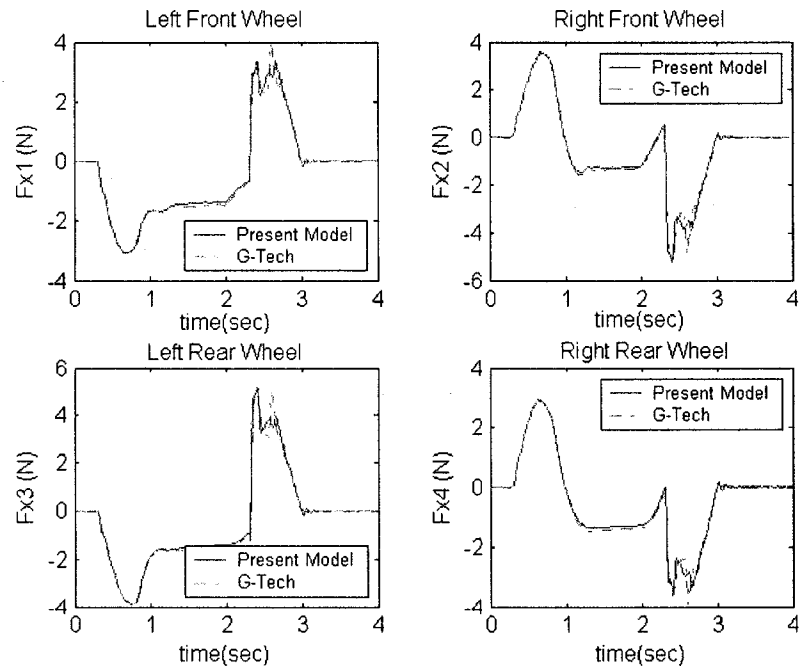


**Figure 5.28a Longitudinal friction forces, no torque input**

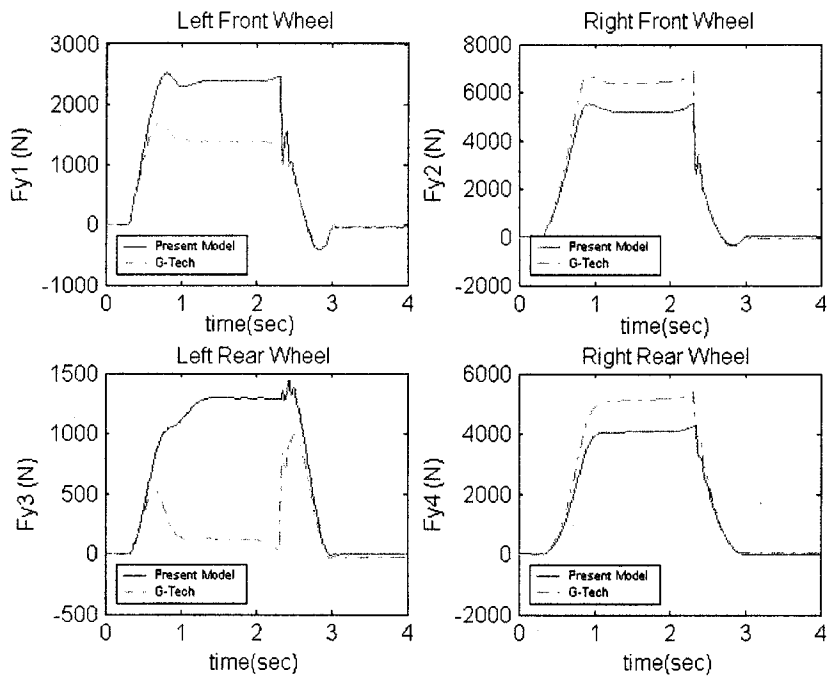


**Figure 5.28b Lateral friction forces, no torque input**

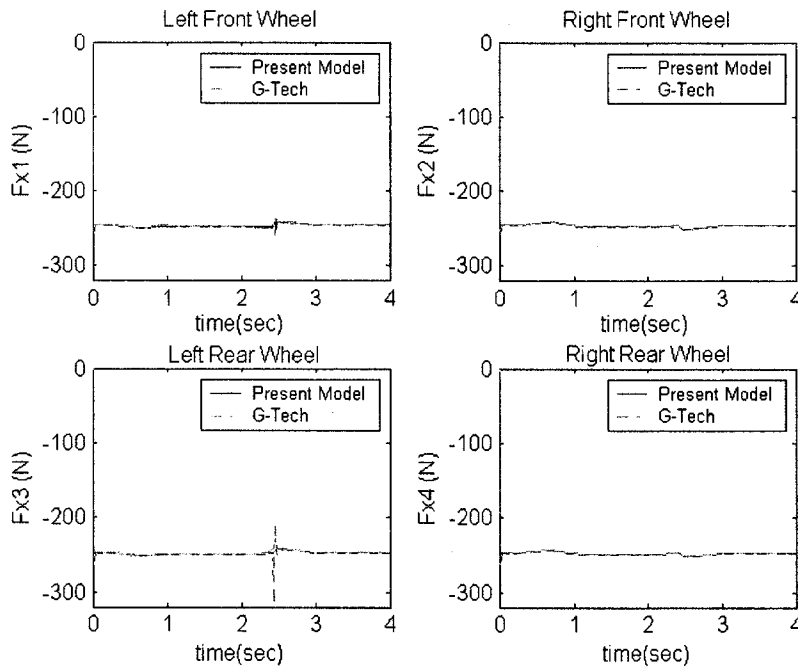


**Figure 5.29a Longitudinal friction forces, 50 N.m torque input**

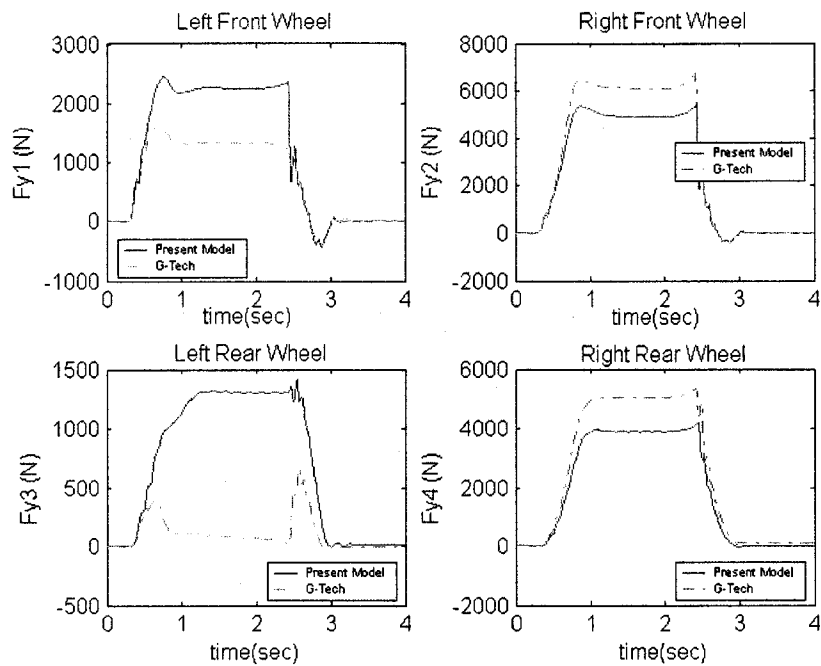


**Figure 5.29b Lateral friction forces, 50 N.m torque input**

Finally, the present model is applied to an icy road surface simulation. The same steering input and parameters are used. The frictional parameters are however taken as  $\mu_s = 0.2$  and  $\mu_k = 0.1$ . The resulting vehicle path on a slippery road surface with zero torque input is shown in Figure 5.30. The slippery road condition has significantly reduced the lateral and yaw motion of the vehicle body resulting in a much greater turning radius.

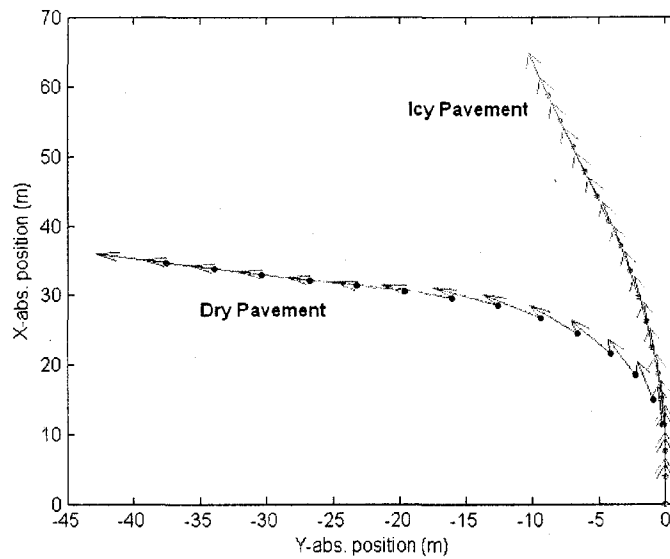


**Figure 5.30 Comparison of vehicle positions, no torque input**

If a front-wheel drive vehicle is considered on the same slippery road with a 100 N-m input torque applied to each of the front wheels so that the total input torque remains at 200 N-m, Figure 5.31 shows that an even greater turning radius results. As shown in Figure 5.32 when the same torques are inputted to the rear wheels, the vehicle spins out of control, as much higher lateral friction forces are exerted onto the front wheels (see Figure 5.33), producing a very high yaw moment and causing the vehicle to rotate and spin out of control.

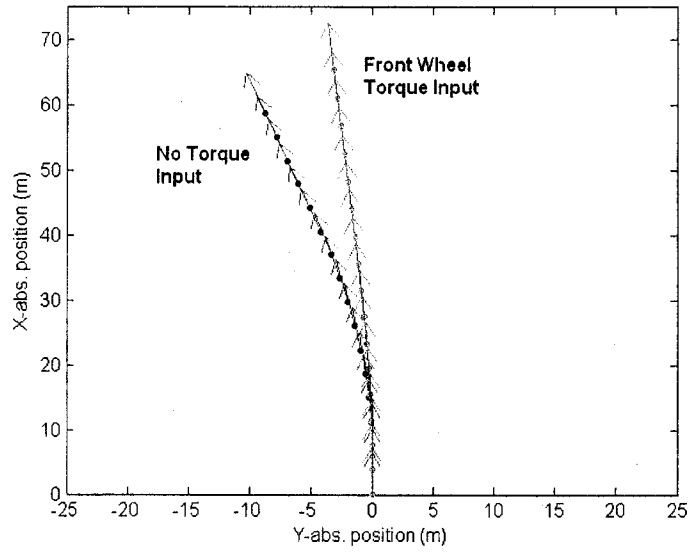


**Figure 5.31 Comparison of vehicle positions, slippery road**

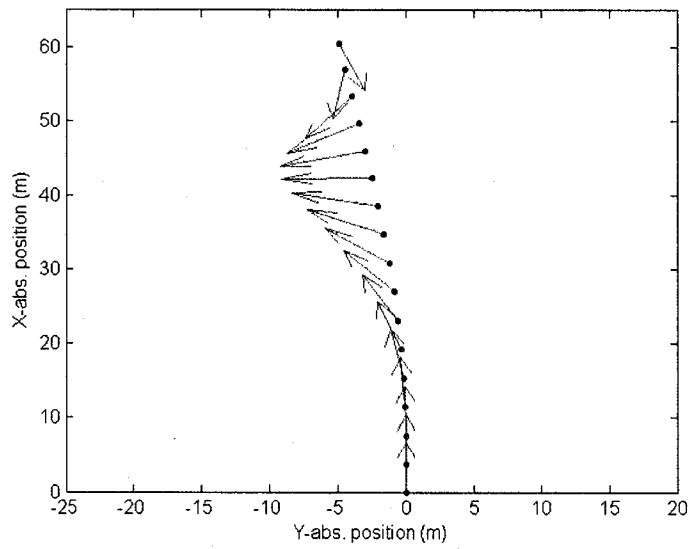


**Figure 5.32 Vehicle spins out of control, 100 N.m torque to rear wheels**

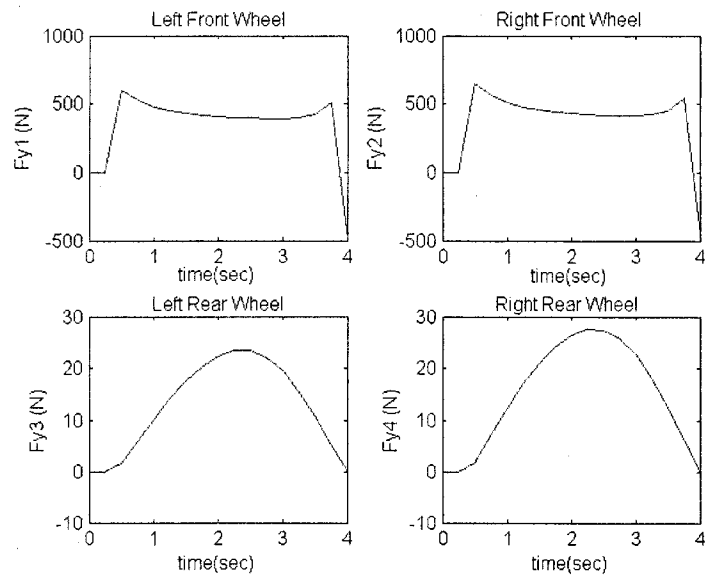


**Figure 5.33 Lateral frictional forces, 100 N.m torque to rear wheels**

#### 5.4 Conclusions.

In this chapter, the mathematical models developed and presented in Chapters 3 and 4 were applied and tested against three previous studies. Three cases were studied, 1) a seven degrees-of-freedom half-car model of a three-wheeled vehicle, with friction forces modeled by dry friction (with no-slip only) [5.1] or by the LuGre model as was the case of the model presented here, 2) a seven degrees-of-freedom full-car model [5.2], with passive suspension and dry friction (with no slip or with slip), and 3) another seven degrees-of-freedom full-car model in which the suspension were absent [5.3], but were presented in the model developed here.

- 1) The model proposed here was able to reproduce published work [5.1, 5.2]. See Figure 5.3 through 5.5 for the three-wheeled vehicle with friction [5.1], and Figures 5.10 and 5.11 for the full-car model of [5.2]. Note that for these two cases, the proposed model adopts either the LuGre friction model or the dry friction model.
- 2) The author's model was able to capture the essence of the vehicle's dynamic behavior, see Figures 5.25 through 5.29. Specifically, vehicle speeds, vehicle positions (when there is no input torque) and longitudinal frictional forces were found to be identical to or extremely close to those of [5.3]. However, differences were observed in vehicle positions (with input torques present) and in lateral friction forces. Note that the proposed model and the model of [5.3] both employed the LuGre friction model. They differed in the treatment of suspensions, to include them in the proposed model and to neglect them in [5.3].
- 3) Therefore, it is suggested that the proposed model is as accurate as the publications referenced and compared. Discussions in sub-sections 5.3.3.1 and 5.3.3.2 also suggest that the rigorous modeling and mathematical development

presented in Chapter 3 yields a model that captures the physical essence of the vehicle.

- 4) The model presented here is versatile in that it can be simplified to quarter- and half-car models, and that it can easily adopt other friction and damper models.

Now that the vehicle model has been developed and verified, a control algorithm needs to be implemented.

## CHAPTER 6

### SLIDING MODE CONTROL

In recent decades, automobiles have continuously been improved with the implementation of various control techniques. Such techniques serve to optimize the functionality and safety of the vehicles. Meeting the demand for better handling and ride comfort has been one of the most intensified research areas in vehicle control.

A great deal of attention has been given to the vehicle suspension system which in turn influences the ride, handling and maneuverability of a vehicle. The induced vibrations from the road surface pass through the suspension system before affecting the body. In the meantime, through the suspension system, the vibration of the vehicle body influences the tires' dynamic loading and consequently the handling of the vehicle. The main functions of the suspension system are therefore to provide effective isolation from road surface unevenness and to improve ride comfort while maintaining a desired level of road holding (the ability of a car to grip the pavement, as measured by lateral acceleration in terms of gravitational acceleration  $g$ ) so as to provide stability and directional control during handling maneuvers. The control design of active suspension system has undergone a major development. Many control laws have been employed for the linear

and nonlinear models of quarter-, half- and full-vehicle systems [6.1-6.9]. A detailed comparison of performances of various active and passive suspension systems on quarter-, half- and full-car models using full-state feedback control can be found in [6.10].

This chapter presents the active suspension control of a half-car (bounce-pitch) model using the non-switch sliding mode control technique of [6.9]. As a case study, an half-car model with 4 DOFs will be subjected to excitation from a ramp-step road profile. The performance of the active suspension will be evaluated, and compared with that of the passive suspension. The effectiveness of the controller for active suspension systems will be demonstrated. The vehicle body's bounce and pitch motions will also be examined in the frequency domains. The robustness of the controller will then be tested by varying the vehicle's physical parameters within their possible operating range.

This chapter is a logical extension of the vehicle model developed previously in Chapters 3 and 4, and verified in Chapter 5. After all, a mathematical model is more useful if it can be used as a tool towards improvement of the physical system that it represents.

## **6.1 Background.**

Suspension is required for ride comfort and road holding. Excitation of vehicle vibration is primarily due to road irregularities. With suspension, the vehicle body becomes less

sensitive to the disturbances generated by the road surface acting on the wheels. In the early days, suspension system of most vehicles was purely passive, schematically represented by dampers and springs (see, for examples, Figure 6.1a). The quality of a passive suspension depends on suspension parameters. For example, good ride comfort requires soft springs but this yields poor road holding. An optimal passive suspension system possesses properly tuned spring and damping coefficients, providing satisfactory ride comfort and road holding simultaneously. In addition, the resonance frequencies associated with the sprung ( $M_b$ ) and unsprung ( $m$ ) masses remain permanent when passive suspensions are employed [6.5, 6.9].

Active suspensions, on the other hand, regulate the interaction between the vehicle body and the wheel by an actuator (see Figure 6.1b). The actuator may be electronically or hydraulically controlled and applies a force between the vehicle body and the wheel. This force represents the control action. The advantage of the active suspension over the conventional suspension is the capability to control the attitude of the vehicle, to reduce the effects of braking and to reduce the vehicle roll during cornering maneuvers in addition to increase the ride comfort and vehicle road handling. Thus, it becomes a much focused research area in vehicle control.

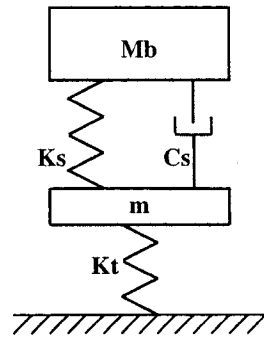


**Figure 6.1a Schematic of a passive suspension system**

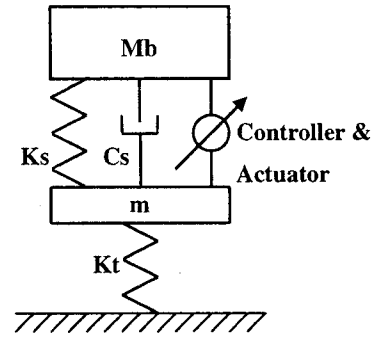


**Figure 6.1b Schematic of an active suspension system**

Control design of the active suspension system has also witnessed a major development. Many control laws have been applied to linear and nonlinear models of quarter-, half- and full-vehicle systems. The most common type of controller studied has been the linear quadratic regulators (LQR) with optimal state feedback control [6.1]. Other techniques have also been investigated, including PID controller [6.2], state and output feedback scheduled controller [6.3], stabilizing controllers [6.4] and fuzzy logic controllers [6.5]. In the area of robust control, techniques such as the  $H_\infty$  output feedback control [6.6], the mixed  $H_2/H_\infty$  controller [6.7], the modular adaptive robust control technique [6.8], and the sliding mode controller [6.9] have been investigated to increase the robustness of suspensions designed for automobiles.

In particular, a non-switch sliding mode control (SMC) method with chattering-free characteristic was discussed in [6.9]. “Chattering” refers to the high frequency switching of sliding mode controller, and the audible noise associated with it. Reference [6.11]

presented a survey of chattering problems in SMC systems, and provided several possible methods for chattering suppression. Reference [6.12] showed the application of higher order sliding mode control for eliminating chattering. The theory of SMC has been developed to provide a systematic approach to the problem of maintaining stability and consistent performance in the face of modeling uncertainties, in which the control strategies based on SMC schemes are robust against disturbances and parameter uncertainties [6.14]. Because of the insensitivity features, the SMC theory has been applied to a wide class of systems, such as applications of the robot manipulators, spacecraft, and power systems. Most of the early work in the area had been proposed by Utkin [6.13].

## 6.2 Vehicle Model (A Pitch-Bounce Half-Car).

The equations of motion of a pitch-bounce vehicle model with active suspension are given below in equations (6.1) through (6.3). The control forces generated by the front and rear actuators are represented by  $u_n$  (where  $n = 1, 2$ ). Note that such a vehicle model with passive suspension has been presented in Section 3.5.2.

$$m_n \ddot{z}_n = k_{sn}(z - x_n \gamma - z_n) + c_{sn}(\dot{z} - x_n \dot{\gamma} - \dot{z}_n) - k_{tn}(z_n - R_n) - u_n \quad (6.1)$$

$$M_b \ddot{z} = -\sum [k_{sn}(z - x_n \gamma - z_n) + c_{sn}(\dot{z} - x_n \dot{\gamma} - \dot{z}_n) - u_n] \quad (6.2)$$

$$I_{y, cg} \dot{\gamma} = \sum [k_{sn}(z - x_n \gamma - z_n)x_n + c_{sn}(\dot{z} - x_n \dot{\gamma} - \dot{z}_n)x_n - u_n x_n] \quad (6.3)$$

These equations can be expressed in the state-space form,

$$\dot{\underline{x}} = f(\underline{x}) + [B]\underline{u} \quad (6.4)$$

where,  $\underline{x} = [x_1, x_2, x_3, x_4, x_5, x_6, x_7, x_8]^T = [z_1, z_2, z, \gamma, \dot{z}_1, \dot{z}_2, \dot{z}, \dot{\gamma}]^T$ . And  $f(\underline{x})$  is a vector

of functions. Matrix  $[B]$  is the controller coefficient matrix having the dimension of  $8 \times 2$ ,

and  $\underline{u} = [u_1, u_2]^T$  is the control input vector. The system parameters are given in Table

6.1.

**Table 6.1 System Parameters**

Parameter	Value	Unit
$M_b$	1500	kg
$m_1$	100	kg
$m_2$	200	kg
$k_{s1}$	28000	N/m
$k_{s2}$	34000	N/m
$k_{t1}$	400000	N/m
$k_{t2}$	400000	N/m
$c_{s1}$	2000	N.s/m
$c_{s2}$	2000	N.s/m
$x_1$	1.0	m
$x_2$	-1.2	m
$I_{y, cg}$	1600	kg.m <sup>2</sup>

### 6.3 Sliding Mode Controller Design.

The theory of SMC can be found mostly in the nonlinear control literature, see, for example, reference [6.14]. The procedure of developing an SMC algorithm includes two stages [6.15, Section 4.3], the first is to define a pre-specified sliding surface  $\underline{s}$ , and the second to develop a control law that will guarantee the attractiveness of the system trajectory to the surface. Once the system trajectory is confined to the pre-specified surface, the so-called sliding mode occurs. While in sliding mode, the system is insensitive to parameter variations and disturbances.

In implementing sliding mode control onto the system given by equation (6.4), the sliding surface  $\underline{s}$  is chosen to be the error of the system and expressed in terms of the error state vector  $\underline{e} = (\underline{x}_{ref}(t) - \underline{x})$  such that,

$$\underline{s}(x, t) = [G]\underline{e} \quad (6.5)$$

Here  $\underline{x}_{ref}(t)$  represents the state vector of the reference, and the constant matrix  $[G]$  represents the slope of the sliding surface.

Under SMC, the system trajectories must stay on the sliding surface (that is  $\underline{s} = 0$ ) for solutions to be stable. To design a control laws  $\underline{u}$  for the close-loop system, Lyapunov's second theorem is employed to ensure the system is asymptotically stable. In

other words, the state trajectories of the controlled system satisfy  $\underline{s} = 0$  only if the existence condition of the sliding surface is met. The existence condition is typically identified as [6.15]

$$\lim_{\underline{s} \rightarrow 0} \underline{s} \dot{\underline{s}} \leq 0 \quad (6.6)$$

To satisfy the condition above, it is required that

$$\dot{\underline{s}} = -D\underline{s} \quad (6.7)$$

Note that the derivative of the sliding surface is chosen according to the constant reaching law [6.12]. With  $D > 0$ , the solution of equation (6.7) will ensure the sliding surface to converge to zero.

Typically, the control input vector  $\underline{u}$  consists of a *reaching phase*, in which the system moves from its initial position in the state space to the sliding surface, and a *sliding phase*, in which it moves along the sliding surface to the desired origin. That is,

$$\underline{u} = \underline{u}_{eqv} + \underline{u}_s \quad (6.8)$$

According to the conditions given in equations (6.6) and (6.7)

$$\begin{aligned} \underline{s} \dot{\underline{s}} &= -\underline{s} D \underline{s}^T \leq 0 \\ \dot{\underline{s}} &= -D \underline{s} \end{aligned} \quad (6.9)$$

Employing the derivative of equation (6.5)

$$\begin{aligned} [G] \left[ \frac{d\underline{x}_{ref}}{dt} - \frac{d\underline{x}}{dt} \right] &= -D \underline{s} \\ [G] [\dot{\underline{x}}_{ref} - (\underline{f} + [B] \underline{u})] &= -D \underline{s} \end{aligned} \quad (6.10)$$

The SMC input  $\underline{u}$  is found to be

$$\underline{u} = -([G][B])^{-1} \{ [G](\underline{f} - \dot{\underline{x}}_{ref}) \} + ([G][B])^{-1} D\underline{s} \quad (6.11)$$

where  $([G][B])^{-1}$  must exist. The first term is referred to as the equivalent control  $\underline{u}_{equiv}$ ,

which is formulated by setting  $\dot{\underline{s}} = 0$ , and dictates the motion of the state trajectory along

the sliding surface.

$$\underline{u}_{equiv} = -([G][B])^{-1} \{ [G](\underline{f} - \dot{\underline{x}}_{ref}) \} \quad (6.12)$$

Since when  $\underline{s} \neq 0$ , equation (6.11) is in effect, forcing the system states move from their

initial position in the state space to the sliding surface; and when  $\underline{s} = 0$ ,  $\underline{u} = \underline{u}_{equiv}$  is true, or

the system moves along the sliding surface to the desired position. Thus, the two stages

of SMC are realized.

The uncertainties in system parameters may result in a poor knowledge in  $\underline{f}$  and  $[B]$ ,

which in turn may cause the calculated equivalent control  $\underline{u}_{equiv}$  to be far off from the actual

equivalent control. Thus, an estimation  $\hat{\underline{u}}_{equiv}$  was suggested by [6.9] to replace  $\underline{u}_{equiv}$ . That is,

$$\hat{\underline{u}}_{equiv} = \frac{1}{\tau s + 1} \underline{u} \quad (6.13)$$

where  $\frac{1}{\tau}$  is the cutoff frequency. The purpose of using a low pass filter is to bypass the

high frequencies coming from undesirable system oscillations with finite frequency

caused by system imperfections, and to retain the characteristics of the signal. Finally, the

non-switch SMC is given by

$$\underline{u} = \hat{\underline{u}}_{eqv} + ([G][B])^{-1} D\underline{S} \quad (6.14)$$

with  $\hat{\underline{u}}_{eqv}$  given by equation (6.13).

#### 6.4 Simulations and Discussions.

Simulations have been carried out to demonstrate the effectiveness of SMC for active suspension systems in comparison to the passive suspension. Road disturbance has been taken as a single ramp-step bump having a height of 0.02 m between  $t = 1.0$  s and  $t = 1.20$  s (see Figure 6.2). Two such road inputs are applied to the system, with a time delay  $\delta t$  between them. The vehicle is assumed to travel at a constant speed of 10 m/s. The comparison between passive and active suspensions is made in both the time and frequency domains.

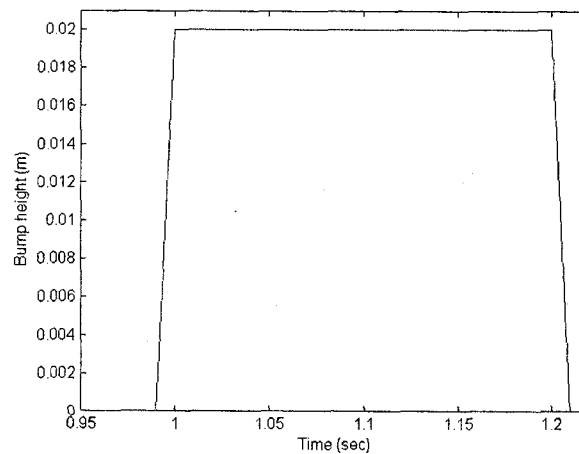


**Figure 6.2 A single ramp-step bump**

The control input  $\underline{u}$  is determined by allowing  $\underline{x}_{ref} = \{0\}$  for all reference states.

Parameter  $\tau$  is set to 0.05 ~ 0.1s since the two resonance frequencies pertaining to body motion and wheel hop (the violent up and down motion of a wheel) are found to be less than 10 Hz.

$[G]$  and  $D$  are non-unique. From the practical point of view, these values are determined from the design limitations of the suspension system and actuator, such as maximum working space and actuator saturation. Two sets of control parameters ( $[G]$  and  $D$ ) are used in the present study. These parameters are identified through trial-and-error. The first set is used to demonstrate the effectiveness of SMC regardless of the physical limitation on the actuator; whereas, the second set takes into account the physical limitation.

#### 6.4.1 First Set of Control Parameters.

$$[G] = \begin{bmatrix} 0 & 0 & 10 & 0 & 0 & 0 & 5 & -2 \\ 0 & 0 & 0 & 0 & 0 & 0.01 & 0 & 0.3 \end{bmatrix}, \quad D = 50$$

The controlled and uncontrolled (as in the case of passive suspension) vehicle body bounce and pitch displacements and their accelerations are presented in Figure 6.3. The vehicle body follows a smooth trajectory against the road irregularities being sensed by the front and rear wheels as seen in Figures 6.3a and 6.3b (the dotted lines). The vehicle body's controlled bounce and pitch reach the zero reference value much faster and with

much less oscillation. The decrease in vehicle body bounce and pitch accelerations give rise to a more comfortable ride, see Figures 6.3c and 6.3d. The maximum value of the control forces is around 900 N as seen in Figures 6.4a and 6.4b. This relatively high value, together with the fact that the control forces,  $u_1$  and  $u_2$ , are varying with a frequency of 7 – 8 Hz, makes it impossible to actually implement the actuator. Otherwise, the forces are found to be changed reasonably smooth and without any rapid changes known as chattering which can harm vehicle components.

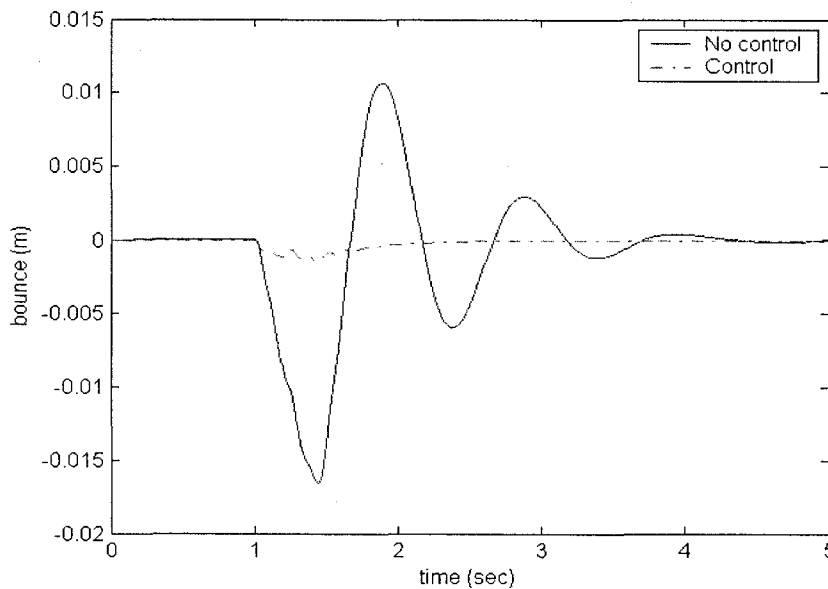


**Figure 6.3a Vehicle body bounce**

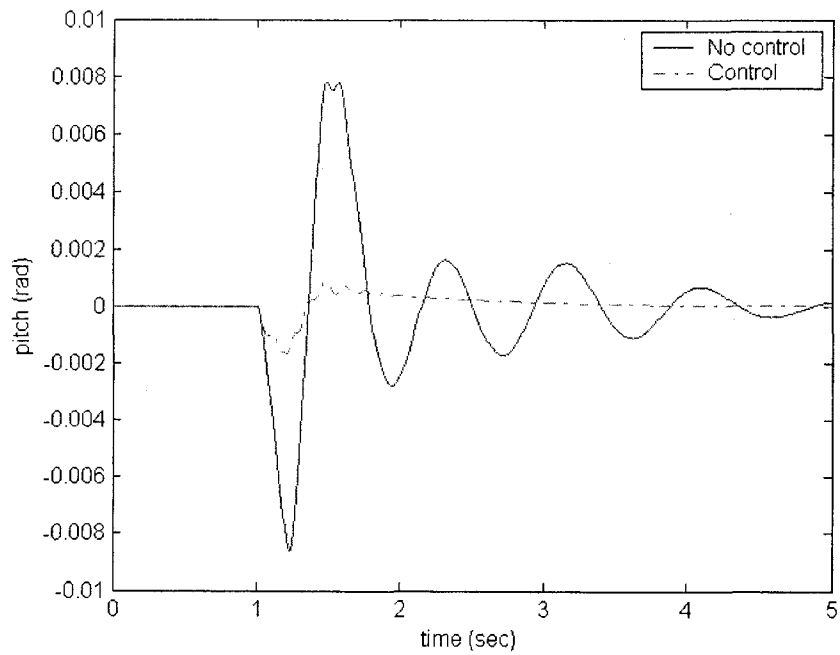


**Figure 6.3b Vehicle body pitch**

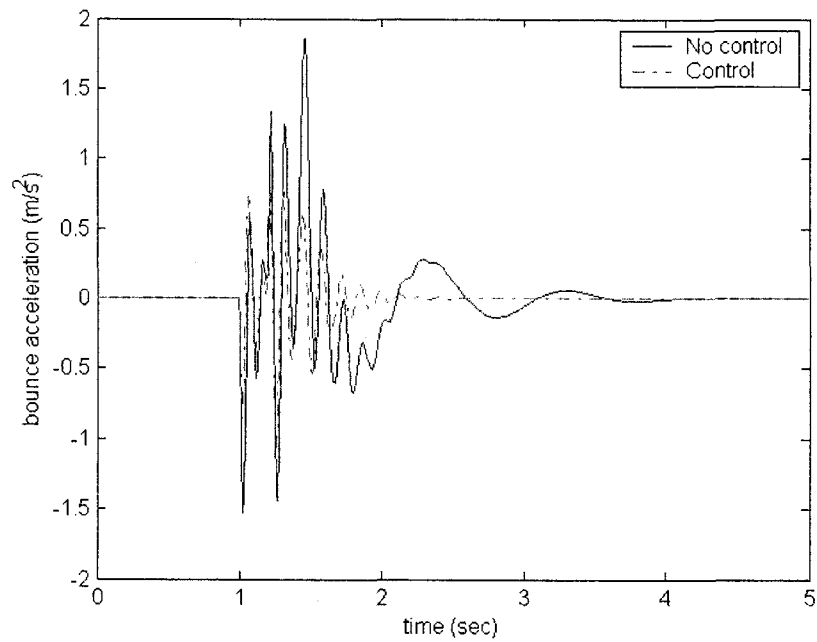


**Figure 6.3c Acceleration of vehicle body bounce**

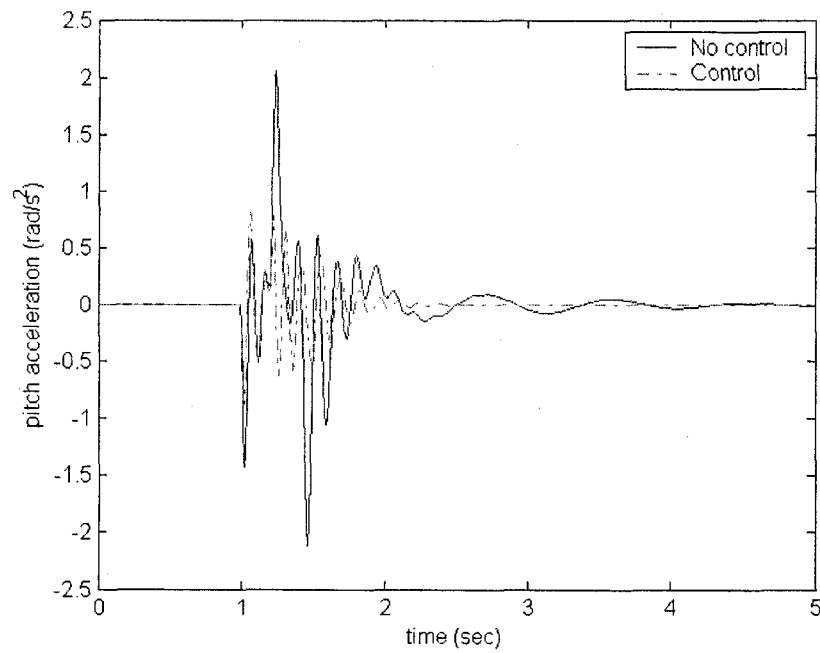


**Figure 6.3d Acceleration of vehicle body pitch**

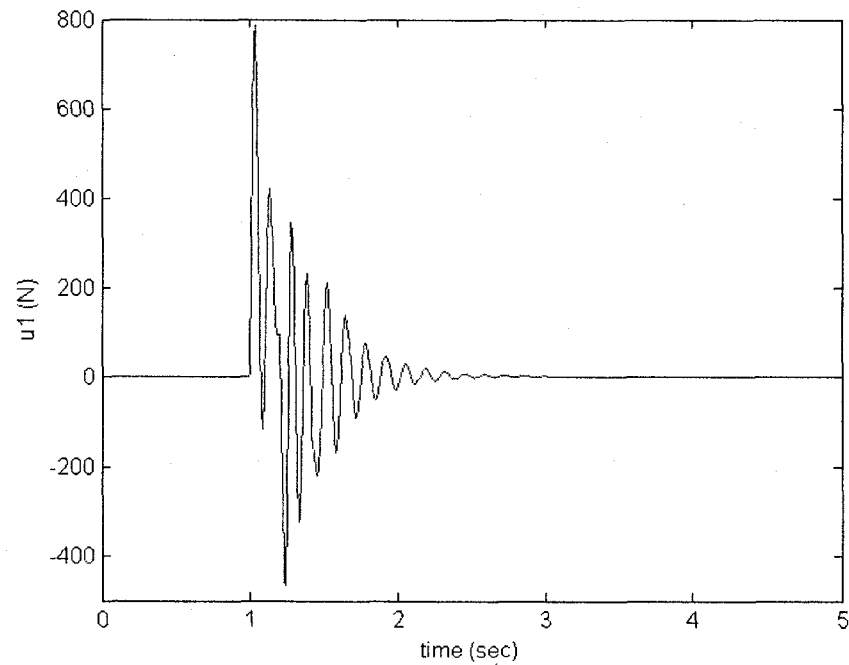


**Figure 6.4a Control input force at front suspension**

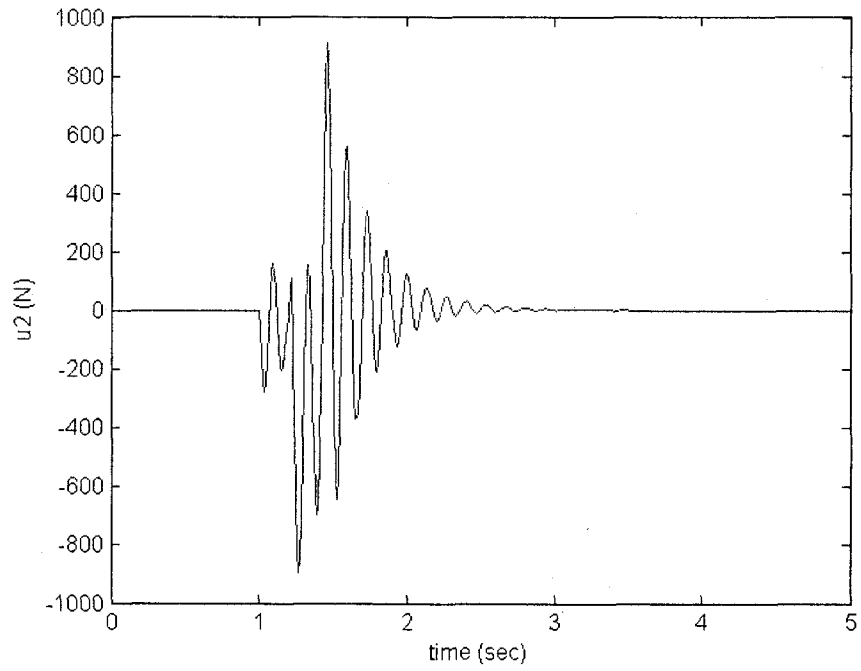


**Figure 6.4b Control input force at rear suspension**

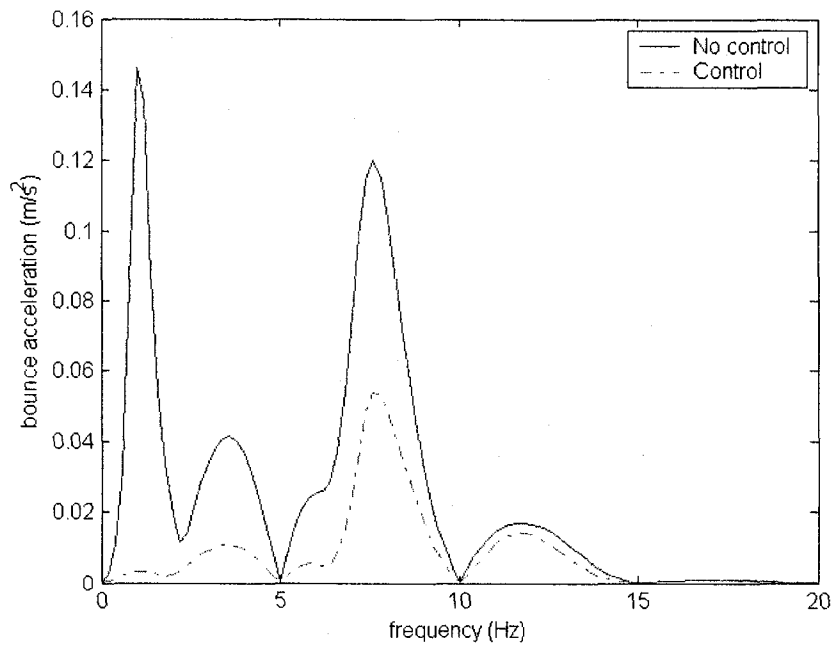


**Figure 6.5a Frequency spectrum of body bounce acceleration**

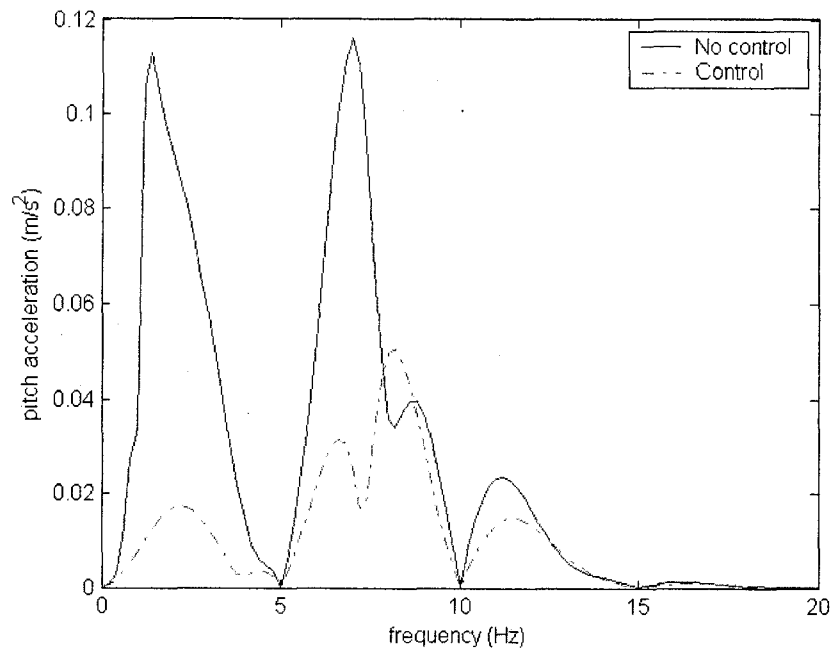


**Figure 6.5b** Frequency spectrum of body pitch acceleration

The frequency responses of the vehicle with passive suspension (i.e., no control) are also examined. There are practically two effective resonance frequencies belonging to body motion and wheel hop. Such frequencies are observed to be 1.1 and 7.5 Hz, respectively, in the frequency spectra of vehicle body bounce and pitch accelerations (Figures 6.5a and 6.5b). From both figures, it is seen that, when the controllers are active, the resonance of pertaining to vehicle body's bounce motion vanishes, albeit not entirely. The spectral intensity at wheel hop frequency is significantly reduced, much more so for the vehicle body's pitch motion. One can therefore conclude that, by employing the SMC strategy, only one mode is controlled. In the present study, this mode is the vehicle body bounce mode.

The robustness character of SMC is illustrated in Figure 6.6 where physical parameters of the model, such as the sprung mass  $M_b$ , and the spring and damping coefficients,  $k_{s1}$ ,  $k_{s2}$ ,  $c_{s1}$  and  $c_{s2}$ , are varied. A controller is said to be robust if it operates effectively over all possible operating conditions. The results in Figure 6.6 clearly demonstrate that the SMC is effective over a wide range of conditions, hence it is robust.

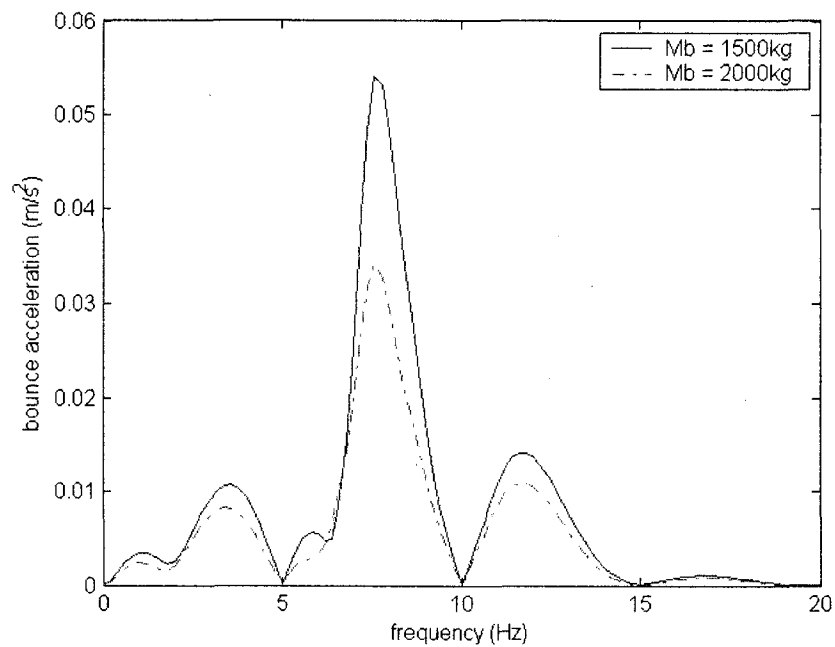


**Figure 6.6a** Vehicle bounce acceleration – Change in sprung mass

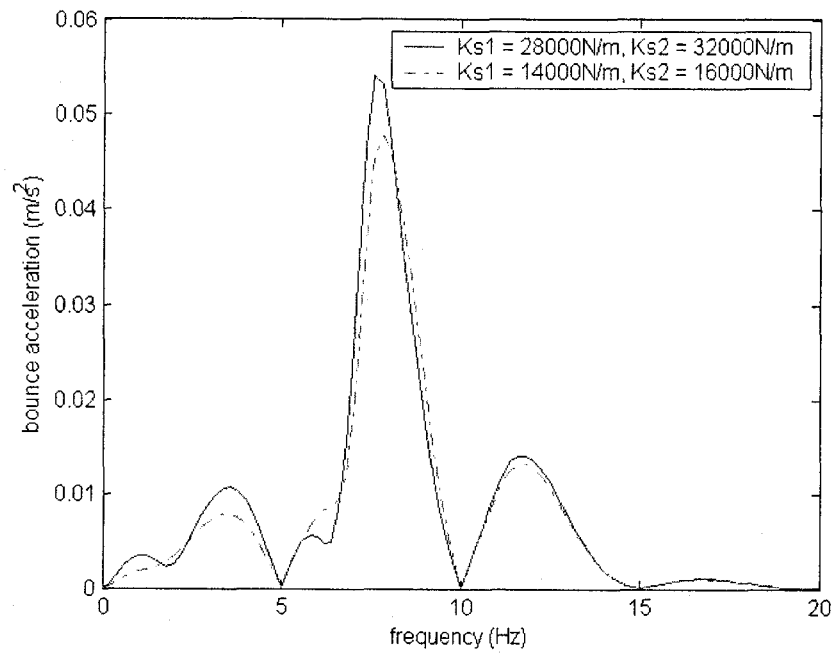


**Figure 6.6b Vehicle bounce acceleration – Change in spring coefficients**

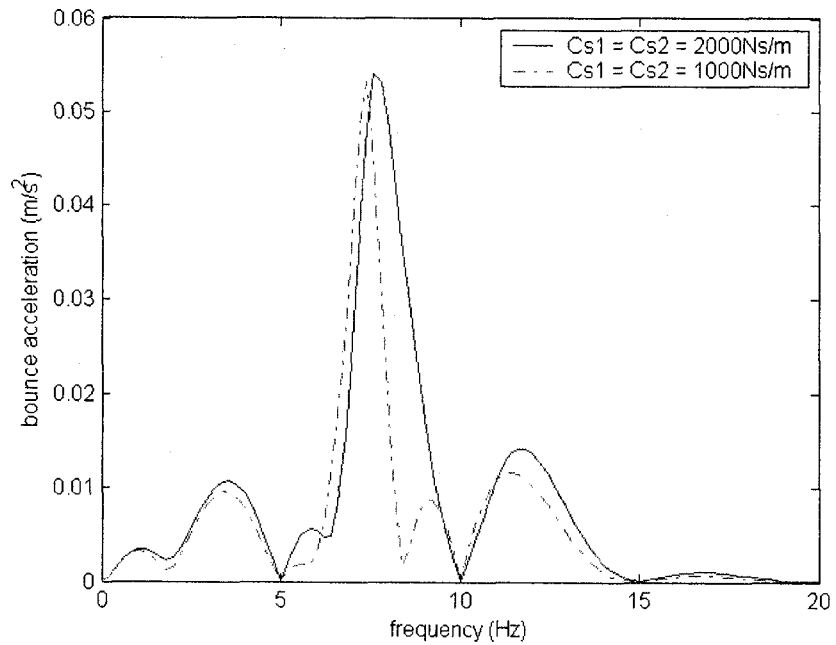


**Figure 6.6c Vehicle bounce acceleration – Change in damping coefficients**

#### 6.4.2 Second Set of Control Parameters.

$$[G] = \begin{bmatrix} 0 & 0 & 100 & 0 & 0 & 0 & 2 & 0 \\ 0 & 0 & 0 & 0 & 0 & 0 & -1 & 4 \end{bmatrix}, \quad D = 2$$

This set of parameters is chosen to lower the jerk effect of the control inputs to a feasible range; As a result, the controller is less effective in isolating vibrations induced from the road surface. As with first case, this set of parameters was also determined by trial-and-error.

As seen in Figures 6.7a and 6.7b, the control input forces now experience lower jerk effect; they are decreased in their peak values' magnitudes and are slower acting in the time domain. For such control inputs, the vehicle body takes longer time to reach the zero reference for its bounce and pitch motions (Figures 6.8a and 6.8b). The frequency spectra of the vehicle body's bounce and pitch accelerations show the reduction of spectral intensity only at the vehicle body's bounce frequency.

Therefore, one can conclude that SMC provides an effective means for reducing the displacement and acceleration of the vehicle body. On the other hand, the ability of using such control technique in practical vehicles would depend on the development of actuators that can withstand the large and fast momentum change required of the control inputs.

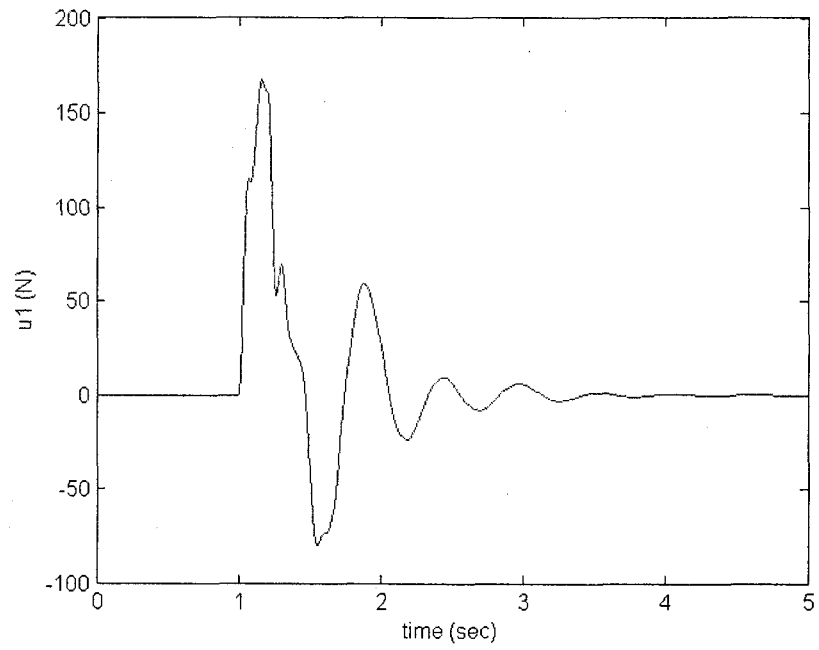


**Figure 6.7a Control input force at front suspension**

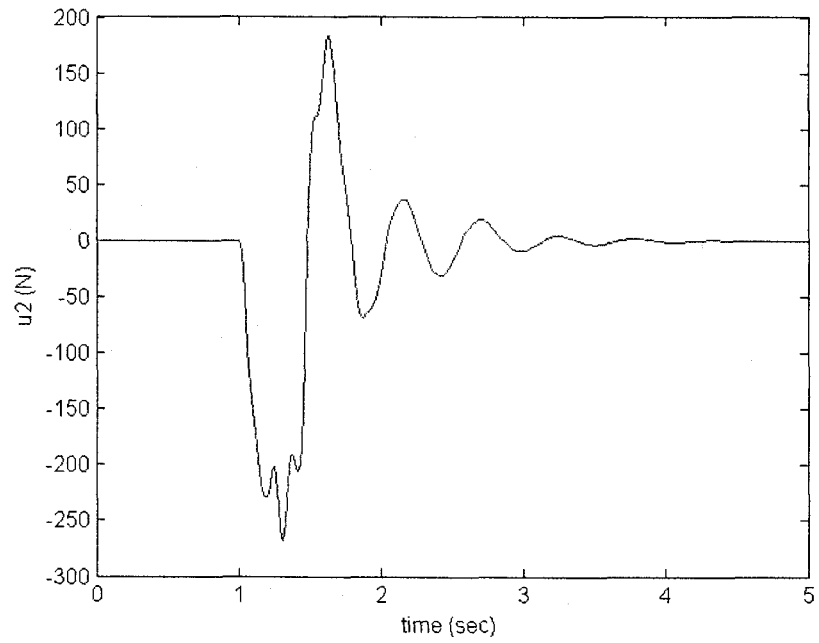


**Figure 6.7b Control input force at rear suspension**

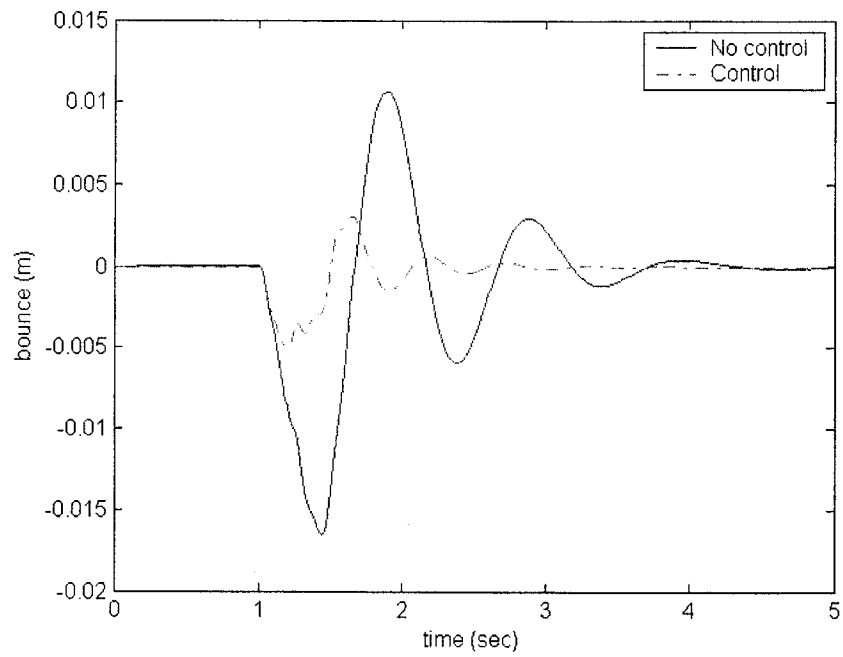


**Figure 6.8a Vehicle body bounce**

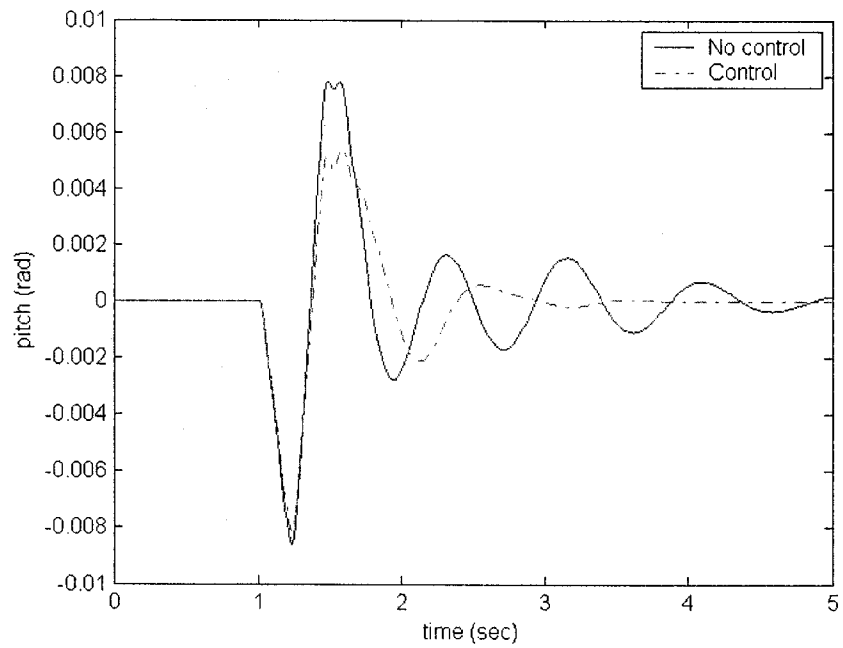


**Figure 6.8b Vehicle body pitch**

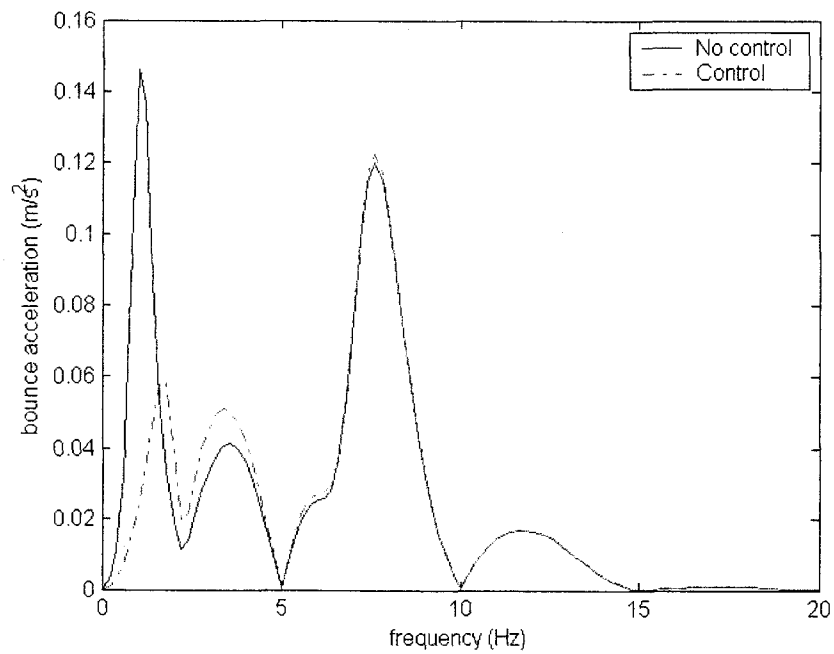


**Figure 6.9a** Frequency spectrum of body bounce acceleration

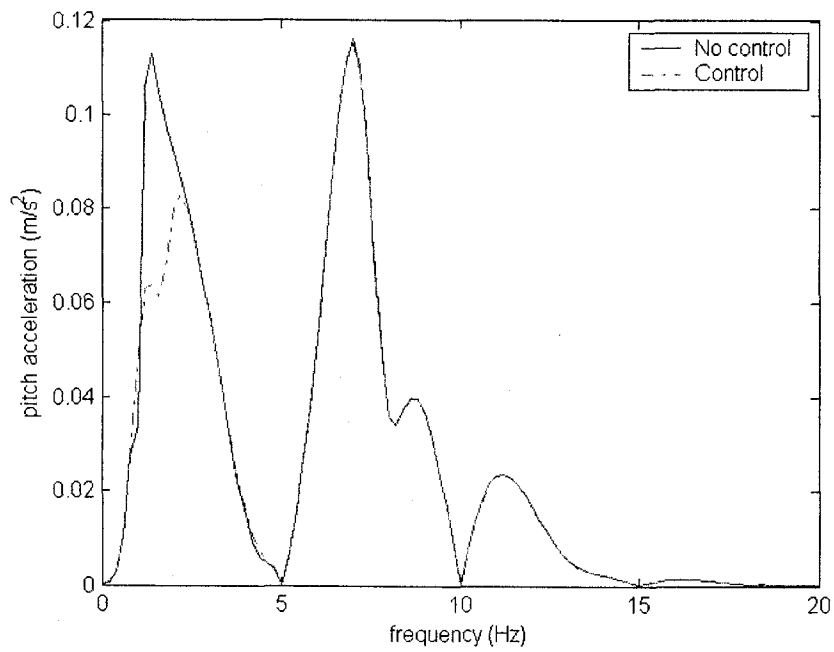


**Figure 6.9b** Frequency spectrum of body pitch acceleration

## 6.5 Conclusions.

In this chapter, a sliding mode controller for the bounce-pitch model of a vehicle has been designed and simulation results presented. The results clearly show improvements in ride comfort. The controller is effective in isolating vibration between the vehicle body and the irregularities in road surface. The controller is also capable of suppressing one mode (the resonance at a frequency associated with the vehicle body's bounce motion). Most importantly, it is proven robust. Moreover, one should realize that such control methodology is possible only when the developed technology can overcome the limitations on the physical components such as actuators.

## CHAPTER 7

### CONCLUSIONS AND RECOMMENDATIONS

The aim of this thesis was to develop a dynamic model of a ground vehicle and to apply control techniques to the model to optimize the functionality and safety of the vehicle.

The theoretical development of the model is detailed in Chapter 3. The model presented provides a means to simulate vehicle motions which can lead to appropriate control and design of vehicles. Main conclusions and some recommendations for future work are given below.

#### 7.1 Conclusions.

Main conclusions resulting from the study presented are listed below.

##### 7.1.1 Vehicle Dynamic Modeling.

A vehicle model with 14-DOF and with independent suspensions and wheels was developed. Features of this 14-DOF full-car model were,

1. The vehicle was treated as an assembly of rigid bodies, the sprung and un-sprung masses, with the following DOFs,
  - The sprung mass, or the vehicle body, was allowed three translational and three rotational motions.

- The un-sprung masses, or the wheels, were each allowed to have both bounce and spin motions.
2. The suspensions were modeled such that the wheel bounces were considered to be independent of the bounce of the vehicle body. Moreover, all bounces of the wheels were also considered independent of each other, as were the spins of the wheels.
  3. Each wheel center was connected to the vehicle body through a “spring-damper” combination.
  4. The tires were considered linear springs with spring constants.
  5. The steering of the wheels was not treated as a DOF. However, steering was incorporated into the model through tire-road interaction, hence becoming “a state”. The model provided wheel torque at each wheel as inputs and vehicle and wheel velocities as outputs.
  6. The fourteen equations of motion were contained in equations (3.35). Equations (3.38)-(3.42) founded a set of five simultaneous equations that were decoupled to allow the solution to proceed.
  7. The full-car model developed could be simplified into various car models with different DOFs.

### 7.1.2 Road-Tire Friction Modeling.

The LuGre friction model was selected to describe the road-tire contact forces due to its simplicity in model derivation, ease of model parameter identification, and high accuracy in predicting the frictional behaviors. The dynamic friction model interprets friction as the interaction of microscopic surface asperities. Existing two-dimensional, single-point-contact LuGre model was examined, and modification of the model was discussed. The modification took into account the coupling between the longitudinal and lateral traction forces, which required consideration of the combined translational and rotational motion of the wheel. This frictional model was then incorporated into the vehicle dynamic model to form a complete set of equations of motions for the vehicle system.

### 7.1.3 Numerical Simulation.

The vehicle model was numerically integrated by using the built-in integration solvers in Matlab. Three vehicle models were studied, (1) a 7-DOF half-car model of a three-wheeled vehicle, in which the tire frictional force was modeled either by dry friction (no-slip only) or by the LuGre model; (2) a 7-DOF full-car model, with passive suspension and dry damping friction; and (3) a 7-DOF full-car model in which the suspensions were either absent or present. Some of the findings were,

1. The model presented was able to reproduce published work for the first two cases and could adopt either the LuGre friction model or the dry friction model.
2. For the third case, the present model was able to capture the essence of the vehicle's dynamic and contact frictional behaviors under the variations of applied wheel torque for normal or slick road conditions. However, discrepancy between the models was found in vehicle positions and in lateral frictional forces when wheel torques were applied. This may be attributed to how the suspensions were modeled.
3. Simulation results suggested that the vehicle model presented was as accurate as the models available in the literature. In addition, it had the versatility in that it could be simplified to quarter- and half-car models, and could easily be adopted to other friction and damper models.
4. In general, the rigorous mathematical development of this vehicle dynamics model provided a model that captured the essence of the vehicle's behavior.

#### 7.1.4 Control Application to the Vehicle Model.

The non-switching sliding mode control technique was implemented in designing the active suspension control system of a half-car model (a bounce-pitch model). Sliding mode control was selected based on its character of maintaining stability and consistent performance in spite of the lack of modeling certainty in a close-loop system. In particular, a non-switching sliding mode control method with chattering-free characteristic was considered for this study. The implemented controller was effective in isolating vibration between the vehicle body and the irregularities in road surface, capable of suppressing one mode (the resonance at a frequency associated with the vehicle body's bounce motion) while reducing significantly the spectral intensity at the other mode, the wheel bounce motion. Most importantly, it was proven robust.

#### **7.2 Recommendations.**

The results in this thesis lay the groundwork for a better understanding of automobile dynamic behavior. There are some natural extensions to this work that can be attempted in the future. They are outlined in the following, in no particular order.

Additional higher-order dynamic effects may be incorporated by adding or modifying certain detail at the component level. For instance, the wheel chamber angle

and the effect of wheel inertia about the  $z$ -axis may be included. The center rolling axis suggested by [3.3] may be introduced to the current model so that the model would be able to handle a wider range of suspension systems.

The average lumped LuGre friction model as presented in [4.2 - 4.4, 4.6] may be incorporated into the current model. This version of LuGre model has been proven to predict friction behaviors that are closer to reality.

In terms of applying the dynamic vehicle model, more numerical simulation may be conducted to demonstrate the capability and accuracy of the current model. It is suggested to gain access to commercial software such as ADAMS/CAR, CARSim, etc., to further validate the model.

Other modeling approaches, for example, the Lagrange's formulation, may also be employed to verify the model itself.

The area of control allows for the greatest opportunities for expansion. Owing to the non-unique nature of the control parameters, they may be fine-tuned by taking into consideration the spatial limitation of the suspension and the actuator's dynamic limitations (available control action) for which active suspension output and control are constrained [3.12]. Extension of the sliding mode control from a half-car to a full-car model may be considered. Further, the horizontal, longitudinal, lateral, and yaw motions

may be controlled by the means of wheel torques. Reference [4.11] has discussed this using a simpler vehicle model and provided good insights to such control application. It serves as a good starting point of control by means of wheel torques.

In conclusion, this thesis has presented a number of unique developments that enable the study of vehicle dynamic behaviors in both modeling and control design. The continued development and refinement of the work are expected to lead to techniques that could potentially improve the vehicle design process.

## APPENDIX A

### DERIVATION OF VELOCITIES AND ACCELERATIONS

#### 1. Velocity and Acceleration at Center of Gravity of the Vehicle Body CG

$V_{cg}$  and  $A_{cg}$  are measured with respect to the fixed global coordinates  $X, Y, Z$ .

However, it is convenient to express the velocity and acceleration in terms of vehicle body coordinates  $x, y, z$  such that

$$V_{cg} = \dot{x}\vec{i} + \dot{y}\vec{j} + \dot{z}\vec{k}, \quad A_{cg} = \ddot{x}\vec{i} + \ddot{y}\vec{j} + \ddot{z}\vec{k} + \dot{x}\dot{\vec{i}} + \dot{y}\dot{\vec{j}} + \dot{z}\dot{\vec{k}} \quad (\text{A.1})$$

where, given  $\Omega = \dot{\varphi}\vec{k}$ , one has

$$\dot{\vec{i}} = \Omega \times \vec{i} = \dot{\varphi}\vec{j}, \quad \dot{\vec{j}} = \Omega \times \vec{j} = -\dot{\varphi}\vec{i}, \quad \dot{\vec{k}} = \Omega \times \vec{k} = \vec{0} \quad (\text{A.2})$$

so that  $A_{cg}$  becomes

$$A_{cg} = (\ddot{x} - \dot{y}\dot{\varphi})\vec{i} + (\ddot{y} + \dot{x}\dot{\varphi})\vec{j} + (\ddot{z})\vec{k} \quad (\text{A.3})$$

#### 2. Velocity and Acceleration at a Wheel Center $CW_n$ .

In determining the velocity and acceleration at a wheel center  $CW_n$ , the kinematics is that of a point in a moving frame of reference, with the vehicle body being the moving frame of reference. The wheel center is assumed to only have motion relative to the moving frame in the vertical direction. The velocity of the wheel center  $CW_n$ , measured

with respect to the fixed global frame of reference but expressed in terms of vehicle body coordinates  $x, y, z$  is

$$\mathbf{V}_{cw,n} = \mathbf{V}_{cg} + \boldsymbol{\Omega} \times \mathbf{r}_{cw,n} + \mathbf{V}_{rel,n} \quad (\text{A.4})$$

where  $\mathbf{V}_{rel,n}$  is the velocity of the wheel center relative to the moving frame, and  $\mathbf{r}_{cw,n}$  the position vector of the wheel center in the moving frame. Defining  $H = h - r$ , the absolute vertical distance from vehicle body center of gravity  $CG$  to centers of the wheels in the initial configuration (Figure 3.10), and  $z_{w,n} = z_n + H - z$ , then

$$\mathbf{r}_{cw,n} = x_n \vec{i} + y_n \vec{j} + z_{w,n} \vec{k} \quad (\text{A.5})$$

where  $x_n$  and  $y_n$  are the  $x$ - and  $y$ -coordinates of the wheel center with respect to the vehicle body frame. They can be determined by the wheelbase and track width of the vehicle. Since,

$$\begin{aligned} \mathbf{V}_{cg} &= \dot{x} \vec{i} + \dot{y} \vec{j} + \dot{z} \vec{k}, \quad \mathbf{V}_{rel,n} = (\dot{z}_n - \dot{z}) \vec{k} \\ \boldsymbol{\Omega} \times \mathbf{r}_{cw,n} &= [-\dot{\varphi} y_n] \vec{i} + [\dot{\varphi} x_n] \vec{j} \end{aligned} \quad (\text{A.6})$$

one obtains, for  $\mathbf{V}_{cw,n}$

$$\mathbf{V}_{cw,n} = [\dot{x} - \dot{\varphi} y_n] \vec{i} + [\dot{y} + \dot{\varphi} x_n] \vec{j} + [(\dot{z}_n - \dot{z}) + \dot{z}] \vec{k} \quad (\text{A.7})$$

and for  $\mathbf{A}_{cw,n}$

$$\begin{aligned} \mathbf{A}_{cw,n} &= [\ddot{x} - \ddot{\varphi} y_n] \vec{i} + [\ddot{x} - \dot{\varphi} \dot{y}_n] \vec{i} + [\ddot{y} + \ddot{\varphi} x_n] \vec{j} + [\ddot{y} + \dot{\varphi} \dot{x}_n] \vec{j} \\ &\quad + [(\ddot{z}_n - \ddot{z}) + \ddot{z}] \vec{k} + [(\dot{z}_n - \dot{z}) + \dot{z}] \dot{\vec{k}} \end{aligned} \quad (\text{A.8})$$

By virtue of (A.2) and  $\dot{z}_{w,n} = \dot{z}_n - \dot{z}$ ,  $\ddot{z}_{w,n} = \ddot{z}_n - \ddot{z}$ , one further writes,

$$\begin{aligned} \mathbf{A}_{cw,n} = & [\ddot{x} - \dot{\varphi}\dot{y} - \dot{\varphi}^2 x_n - \ddot{\varphi}y_n] \vec{i} + [\dot{y} + \dot{\varphi}\dot{x} + \ddot{\varphi}x_n - \dot{\varphi}^2 y_n] \vec{j} \\ & + [(\ddot{z}_n - \ddot{z}) + \dot{z}] \vec{k} \end{aligned} \quad (\text{A.9})$$

Note that equation (A.9) is identical to equation (3.11), hence proving that the approaches used in Chapter 3 and used above, albeit different points of view in treating the kinematics, are identical. It is also interesting to note that the small roll and small pitch assumption has not been invoked in the above derivation. For the derivation in Chapter 3, though the second half of equation (3.7) assumes small roll and small pitch, equations (3.8) – (3.11) are valid with and without the small roll small pitch assumption.

## REFERENCES

### Chapter 1

- [1.1] D.A. Crolla, "Vehicle Dynamics - Theory into Practice", *Journal of Automobile Engineering*, **210**, 83-94, 1996.
- [1.2] R.S. Sharp, "The Application of Multi-Body Computer Codes to Road Vehicle Dynamics Modeling Problems", *Journal of Automobile Engineering*, **208**, 55-61, 1994.
- [1.3] [http://www.mscsoftware.com/products/adams\\_applications.cfm?Q=396&Z=397](http://www.mscsoftware.com/products/adams_applications.cfm?Q=396&Z=397)
- [1.4] <http://www.carsim.com/products/carsim>
- [1.5] <http://www.mathtools.net/MATLAB/Automotive/index.html>
- [1.6] C. Canudas de Wit, H. Olsson, K.J. Astrom and P. Lischinsky, "A New Model for Control of Systems with Friction", *IEEE Transaction on Automatic Control*, **40**(3), 1995.
- [1.7] MATLAB Release 13, Vers. 6.5.0, The MathWorks Inc., 2002

### Chapter 2

- [2.1] F.H. Speckhart, "A Computer Simulation for Three-Dimensional Vehicle Dynamics", *SAE Paper 730526*, 1973.
- [2.2] D.A. Crolla, "Vehicle Dynamics - Theory into Practice", *Journal of Automobile Engineering*, **210**, 83-94, 1996.
- [2.3] A. Hac and A.V. Fratini Jr., "Elimination of Limit Cycles due to Signal Estimation in Semi-Active Suspensions", *SAE, ISSN 0148-7191*, 1999.
- [2.4] D.E. Simon, "Experimental Evaluation of Semiactive Magnetorheological Primary Suspensions for Heavy Truck Applications", M.Sc. Thesis, Virginia Polytechnic Institute and State University, 1998.
- [2.5] H. Chen, Z.Y. Liu and P.Y. Sun, "Application of Constrained  $H_{\infty}$  Control to Active Suspension Systems on Half-Car Models", *J. Dynamic Systems, Measurement and Control*, **127**, 345-354, 2005.
- [2.6] T.R. Gawade, S. Mukherjee and D. Mohan, "Wheel Lift-off and Ride Comfort of Three-Wheeled Vehicle over Bump", *IE(I) Journal*, **85**, 78-87, 2004.

- [2.7] T.R. Gawade, S. Mukherjee and D. Mohan, "Six Degree-of-Freedom Three-Wheeled Vehicle Model Validation", *Proceedings of the I MECH E Part D Journal of Automobile Engineering*, **12(D4)**, 487-498, 2005.
- [2.8] E. Bakker, H.B. Pacejka and L. Lidner. "A New Tire Model with an Application in Vehicle Dynamics Studies", SAE Paper #890087, 1989.
- [2.9] M.G. Villella, "Nonlinear Modeling and Control of Automobiles with Dynamic Wheel-Road Friction and Wheel Torque Inputs", Master's thesis, School of Electrical and Computer Engineering, Georgia Institute of Technology, 2004.

### Chapter 3

- [3.1] A. Bedford and W. Fowler, "*Engineering Mechanics, Dynamics*", Addison-Wesley, 286-289, 1994.
- [3.2] "*Vehicle Dynamics Terminology*", SAE Recommended Practice J-670e, Society of Automotive Engineers, 1976.
- [3.3] A.Y. Ungoren and H. Peng, "Evaluation of Vehicle Dynamics Control for Rollover Prevention", University of Michigan, 2003.
- [3.4] F.H. Speckhart, "A Computer Simulation for Three-dimensional Vehicle Dynamics", *SAE paper # 730526*, 1973.
- [3.5] F.J. Alonso, "Experimental Analysis of Vehicle Dynamics. Validation of A Novel Vehicle Mathematical Model Using Advanced Instrumentation", Insia-Polytecnic University of Madrid, 2004.
- [3.6] T.D. Day, S.G. Roberts and A.R. York, "SIMON: A New Vehicle Simulation Model for Vehicle Design and Safety Research", *SAE paper #2001-01-0503*, 2001.
- [3.7] T.R. Gawade, S. Mukherjee and D. Mohan, "Wheel Lift-off and Ride Comfort of Three-wheeled Vehicle over Bump", *IE(I) Journal*, **85**, 78-87, 2004.
- [3.8] A. Pytal and J. Kiusalaas, *Engineering Mechanics: Dynamics*, HarperCollins Canada, 1994.
- [3.9] Maple 9.01, Vers. 9, Maplesoft of Waterloo Maple Inc., 2003
- [3.10] R.J. Dorling, "Integrated Control of Road Vehicle Dynamics", Ph.D. Dissertation, University of Cambridge, 1996.
- [3.11] A. Hac and F.V. Fratini, Jr., "Elimination of Limit Cycle due to Signal Estimation in Semi-active Suspensions", *SAE paper # 1999-01-0728*, 1999.

- [3.13] D.E. Simon, "Experimental Evaluation of Semiactive Magnetorheological Primary Suspensions for Heavy Truck Applications", M.Sc. Thesis, Virginia Polytechnic Institute and State University, 1998.
- [3.14] H. Chen, Z.Y. Liu and P.Y. Sun, "Application of Constrained  $H_\infty$  to Active Suspension Systems on Half-Car Models", *J. Dynamic Systems, Measurement and Control*, **127**, 345-354, 2005.
- [3.15] A. Giua, C. Seatzu and G. Usai, "A Mixed Suspension System for a Half-car Vehicle Model", *Dynamics and Control*, **10**, 375-397, 2000.
- [3.16] N. Yagiz and I. Yuksek, Sliding Mode Control of Active Suspensions for a Full Vehicle Model, *International Journal of Vehicle Design*, **26**, 264-276, 2001.
- [3.17] R. Güçlü, "Active Control of Seat Vibrations of a Vehicle Model Using Various Suspension Alternatives", *Turkish Journal of Engineering & Environmental Sciences*, **27**, 361-373, 2003.
- [3.18] K. Hayakawa, K. Matsumoto, M. Yamashita, Y. Suzuki, K. Fujimori and H. Kimura, "Robust  $H_\infty$ -Output Feedback Control of Decoupled Automobile Active Suspension Systems", *IEEE Transactions on Automatic Control*, **44**, 392-396, 1999.
- [3.19] L. Zuo and S.A. Nayfeh, "Structured  $H_2$  Optimization of Vehicle Suspensions Based on Multi-Wheel Models", *Vehicle System Dynamics*, **40**, 351-371, 2003.

#### Chapter 4

- [4.1] H. Olsson, K.J. Astrom, C. Canudas-de-Wit, M. Gafvert and P. Lischinsky, "Friction Models and Friction Compensation", Report, Department of Automatic Control, Lund Institute of Technology, 1997.
- [4.2] E. Velenis, P. Tsiotras and C. Canudas-de-Wit, "Extension of the LuGre Dynamic Tire Friction Model to 2D Motion", Report, School of Aerospace Engineering, Georgia Institute of Technology, 2001.
- [4.3] J. Yi, S. Suryanarayanan, A. Howell, R. Horowitz, M. Tomizuka and K. Hedrick, "Development and Implementation of a Vehicle-Centered Fault Diagnostic and Management System for the Extended PATH-AHS Architecture: Part II", Report, Department of Mechanical Engineering, University of California at Berkeley, 2002.
- [4.4] C. Canudas-de-Wit, P. Tsiotras, E. Velenis, M. Basset and G. Gissinger, "Dynamic Friction Models for Road/Tire Longitudinal Interaction", *Vehicle System Dynamics*, **39**(3), 189-226, 2003.

- Friction Models for Road/Tire Longitudinal Interaction”, *Vehicle System Dynamics*, **39**(3), 189-226, 2003.
- [4.5] J. Svendenius and B. Wittenmark, “Review of Wheel Modeling and Friction Estimation”, Report, Department of Automatic Control, Lund Institute of Technology, 2003.
- [4.6] J. Deur, J. Asgari and D. Hrovat, “A 3D Brush-type Dynamic Tire Friction Model”, *Vehicle System Dynamics*, **42**(3), 133-173, 2004.
- [4.7] M.G. Vilella and D.G. Taylor, “Input-Output Linearization of an Automobile Model with 2D LuGre Friction”, *Proc. American Control Conference*, 429-434, 2005.
- [4.8] C. Canudas de Wit, H. Olsson, K.J. Astrom and P. Lischinsky, “A New Model for Control of Systems with Friction”, *IEEE Transaction on Automatic Control*, **40**(3), 1995.
- [4.9] R. Stribeck, “Die wesentlichen Eigenschaften der Gleit- und Rollenlager”, *Zeitschrift des Vereines Seutscher Ingenieure*, **46**(38), 1342-1348, 1902.
- [4.10] M.G. Vilella, “Nonlinear Modeling and Control of Automobiles with Dynamic Wheel-Road Friction and Wheel Torque Inputs”, Master’s thesis, School of Electrical and Computer Engineering, Georgia Institute of Technology, 2004.
- [4.11] E. Bakker, H.B. Pacejka and L. Lidner. “A New Tire Model with an Application in Vehicle Dynamics Studies”, SAE Paper #890087, 1989.
- [4.12] E. Bakker, L. Nyborg and H. Pacejka, “Tyre Modelling for Use in Vehicle Dynamics Studies”, SAE Paper #870421, 1987.

## Chapter 5

- [5.1] T. R. Gawade, S. Mukherjee, D. Mohan, “Wheel Lift-off and Ride Comfort of Three-Wheeled Vehicle over Bump”, *IE(I) Journal-MC*, **85**, 2004.
- [5.2] G. Rahmi, “Active Control of Seat Vibrations of a Vehicle Model Using Various Suspension Alternatives”, *Turkish J. Eng. Environmental Science*, 361-373, 2003.
- [5.3] M.G. Vilella, “Nonlinear Modeling and Control of Automobiles with Dynamic Wheel-Road Friction and Wheel Torque Inputs”, Master’s thesis, School of Electrical and Computer Engineering, Georgia Institute of Technology, 2004.
- [5.4] J.G. Heydinger, R.A. Bixel, W. R. Garrott, M. Pyne, J.G. Howe and D.A. Guenther, “Measured vehicle inertial parameters-NHTSA’s data through November 1998”.  
[ <http://www-nrd.nhtsa.dot.gov/vrtc/ca/capubs/sae1999-01-1336.pdf> ]

## Chapter 6

- [6.1] K. Birgit, R. Georg, S. Oskar von, Z. Douglas E., "Active Suspension Design For A Tractor By Optimal Control Methods", Sonderforschungsbereich 438, Munchen, Augsburg, Technische Universitat Munchen, 1998.
- [6.2] G. Rahmi, "Active Control of Seat Vibrations of a Vehicle Model Using Various Suspension Alternatives", *Turkish J. Eng. Environmental Science*, 361-373, 2003.
- [6.3] I. E. Kose, F. Jabbari, "Scheduled controllers for linear systems with bounded actuators," *Automatica* **39**, 1377-1387, 2003.
- [6.4] M. C. Smith, F-C Wang, "Controller Parameterization for Disturbance Response Decoupling: Application to Vehicle Active Suspension Control." *IEEE Transactions on Control Systems Technology*, **10**(3), 393-407, 2002.
- [6.5] L. Sakman, R. Guclu, N. Yagiz, "Fuzzy logic control of vehicle suspensions with dry friction nonlinearity." *Sadhana*, **30**, Part 5, 649-659, 2005.
- [6.6] K. Hayakawa, K. Matsumoto, M. Yamashita, Y. Suzuki, K. Fujimori, and H. Kimura, "Robust  $H_{\infty}$  Output Feedback Control of Decoupled Automobile Active Suspension Systems", *IEEE Transactions on Automatic Control*, **44**(2), 392-396, 1999.
- [6.7] P. Gaspar, I. Szaszi and J. Bokor, "Mixed  $H_2/H_{\infty}$  Control Design for Active Suspension Structures", *Periodica Polytechnica Ser. Transp. Eng.* **28**(1/2), 3-16, 2000.
- [6.8] S. Chantranuwathana, and H. Peng, "Adaptive robust force control for vehicle active suspensions," *Proceedings of the American Control Conference*, 1702-1706, 1999.
- [6.9] N. Yagiz and I. Yuksek, "Sliding Mode Control of Active Suspensions for a Full Vehicle Model", *International Journal of Vehicle Design*, **26**(2/3), 264-276, 2001.
- [6.10] J. D. Richard, "Integrated Control of Road Vehicle Dynamics", PhD. Dissertation, *Cambridge University Engineering Department*, 1996.
- [6.11] J. Guldner and V. I. Utkin, "The chattering problem in sliding mode systems", [http://www.univ-perp.fr/mtns2000/articles/SI14\\_4.pdf](http://www.univ-perp.fr/mtns2000/articles/SI14_4.pdf)
- [6.12] M. Vig, "Higher Order Sliding Mode Control of Differentially Flat Systems", M.Sc. Thesis, *Indian Institute of Tech*, 2004.
- [6.13] V. I. Utkin, "Variable Structure Systems with Sliding Mode", *IEEE Transactions on Automatic Control*, **AC-22**, 212-222, 1977.

- [6.14] J.J.E. Slotine and W. Li, "Applied Nonlinear Control", Prentice-Hall, Inc. 1991.
- [6.15] M. Ahmed, "Sliding Mode Control for Switched Mode Power Supplies", Ph.D. Dissertation, Lappeenranta University of Technology, 2004.